

การพัฒนาเทคนิคการเลี้ยวเบนของรังสีเอกซ์บนผลึกชนิดผงและเทคนิคการเรืองแสงของรังสีเอกซ์โดยใช้
รังสีซินโครตรอน

นางสาววราลักษณ์ แสงสุวรรณ

ศูนย์วิทยทรัพยากร
จุฬาลงกรณ์มหาวิทยาลัย

วิทยานิพนธ์นี้เป็นส่วนหนึ่งของการศึกษาตามหลักสูตรปริญญาวิทยาศาสตรดุษฎีบัณฑิต

สาขาวิชาฟิสิกส์ ภาควิชาฟิสิกส์

คณะวิทยาศาสตร์ จุฬาลงกรณ์มหาวิทยาลัย

ปีการศึกษา 2552

ลิขสิทธิ์ของจุฬาลงกรณ์มหาวิทยาลัย

DEVELOPMENT OF X-RAY POWDER DIFFRACTION AND
X-RAY FLUORESCENT TECHNIQUES USING
SYNCHROTRON RADIATION



Miss Varalak Saengsuwan

ศูนย์วิทยทรัพยากร
จุฬาลงกรณ์มหาวิทยาลัย

A Thesis Submitted in Partial Fulfillment of the Requirements
for the Degree of Doctor of Philosophy Program in Physics

Department of Physics

Faculty of Science


Chulalongkorn University

Academic Year 2009

Copyright of Chulalongkorn University

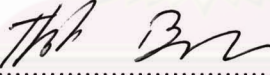
Thesis Title Development of X-ray Powder Diffraction and X-ray Fluorescent
Techniques using Synchrotron Radiation
By Miss Varalak Saengsuwan
Field of Study Physics
Thesis Advisor Assistant Professor Thiti Bovornratanaraks, Ph. D.
Thesis Co-advisor Wantana Klysubun, Ph. D.

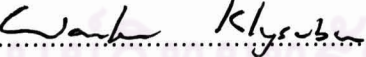
Accepted by the Faculty of Science, Chulalongkorn University in Partial Fulfillment of the
Requirements for the Doctoral Degree


..... Dean of the Faculty of Science
(Professor Supot Hannongbua, Dr.rer.nat.)


THESIS COMMITTEE


..... Chairman
(Assistant Professor Sojiphong Chatrathorn, Ph. D.)


..... Thesis Advisor
(Assistant Professor Thiti Bovornratanaraks, Ph. D.)


..... Thesis Co-advisor
(Wantana Klysubun, Ph. D.)


..... Examiner
(Assistant Professor Nuttakorn Thubthong, Ph. D.)


..... Examiner
(Somrit Wongmanerod, Ph. D.)


..... External Examiner
(Saroj Rujirawat, Ph. D.)

วราลักษณ์ แสงสุวรรณ: การพัฒนาเทคนิคการเลี้ยวเบนของรังสีเอกซ์บนผลึกชนิดผงและเทคนิคการเรืองแสงของรังสีเอกซ์โดยใช้รังสีซินโครตรอน. (DEVELOPMENT OF X-RAY POWDER DIFFRACTION AND X-RAY FLUORESCENT TECHNIQUES USING SYNCHROTRON RADIATION) อ. ที่ปรึกษาวิทยานิพนธ์หลัก: ผศ.ดร.ธิดา บวรรัตนารักษ์, อ.ที่ปรึกษาวิทยานิพนธ์ร่วม : ดร.วันทนา คล้ายสุบรรณ, 129 หน้า.

วิทยานิพนธ์นี้มีวัตถุประสงค์เพื่อพัฒนาการประยุกต์ใช้รังสีซินโครตรอน ณ ห้องปฏิบัติการแสงสยาม สถาบันวิจัยแสงซินโครตรอน (องค์การมหาชน) สำหรับการวิเคราะห์ชิ้นงานต่างๆ เพื่อเพิ่มประสิทธิภาพในการวัด โดยงานนี้ได้ทำการพัฒนาระบบลำเลียงรังสีซินโครตรอนตั้งแต่เริ่มออกแบบระบบลำเลียงรังสีตลอดจนพัฒนาเทคนิคที่สำคัญในการวิเคราะห์ชิ้นงานต่างๆ อาทิเช่น การวิเคราะห์การเลี้ยวเบนของรังสีเอกซ์บนผลึกชนิดผง ด้วยเครื่องตรวจวัดแบบพื้นที่ เพื่อวิเคราะห์การเปลี่ยนแปลงโครงสร้างผลึกของสารภายใต้สภาวะความดันสูง และเทคนิคการวิเคราะห์การเรืองแสงของรังสีเอกซ์ด้วยเครื่องตรวจวัดซิลิกอน พีไอเอ็น เพื่อวิเคราะห์สารประกอบทั้งในเชิงปริมาณ คุณภาพ และระบุตำแหน่งของธาตุต่างๆ ในสารตัวอย่าง โดยเทคนิคนี้ได้ใช้แสงขาวในการกระตุ้นสารตัวอย่างให้เกิดการเรืองแสงของรังสีเอกซ์ แล้วทำการวัดปริมาณรังสีเอกซ์ที่เกิดขึ้น สำหรับการระบุตำแหน่งของธาตุต่างๆ ในสารตัวอย่าง ได้ใช้เลนส์โพลิแคปพิลลารีเพื่อโฟกัสแสงขาวให้มีขนาดเล็กในระดับไมครอน นอกจากนี้ ยังได้พัฒนาโปรแกรมสำหรับเทคนิคการวิเคราะห์การเรืองแสงของรังสีเอกซ์ทั้งในเชิงปริมาณและคุณภาพอีกด้วย

ศูนย์วิทยทรัพยากร
จุฬาลงกรณ์มหาวิทยาลัย

ภาควิชา ฟิสิกส์
สาขาวิชา ฟิสิกส์
ปีการศึกษา 2552

ลายมือชื่อ นิสิต..... วราลักษณ์ แสงสุวรรณ.....
ลายมือชื่อ อ. ที่ปรึกษาวิทยานิพนธ์หลัก.....
ลายมือชื่อ อ. ที่ปรึกษาวิทยานิพนธ์ร่วม.....

4873849423 : MAJOR PHYSICS

KEYWORDS: XRF IMAGING / XRF ANALYSIS / X-RAY POWDER DIFFRACTION / HIGH PRESSURE CONDITION

VARALAK SAENGSUWAN: DEVELOPMENT OF X-RAY POWDER DIFFRACTION AND X-RAY FLUORESCENT TECHNIQUES USING SYNCHROTRON RADIATION. THESIS ADVISOR: ASST. PROF. THITI BOVORNATANARAKS, Ph. D., THESIS COADVISOR: WANTANA KLYSUBUN, Ph. D., 129 pp.

This thesis proposes the analytical techniques that use the synchrotron radiation at the Siam Photon Laboratory, Synchrotron Light Research Institute (Public Organization) as an x-ray source in order to improve the resolution and enhance the process of measurement. The design and development of synchrotron beamline for x-ray powder diffraction under high pressure condition, x-ray absorption spectroscopy and x-ray fluorescent techniques will be presented. This research emphasizes to study the methods of x-ray powder diffraction and x-ray fluorescent techniques that used to characterize the samples. The characteristic x-rays that glow from the sample are stimulated by a white light synchrotron x-ray beam and then collected by a Si-PIN detector. Furthermore, polycapillary x-ray half lens is a powerful tool that used for focusing polychromatic x-rays in x-ray fluorescent imaging technique and also for focusing and increasing photon flux of monochromatic x-rays in x-ray powder diffraction technique under high pressure condition. In addition, necessary x-ray fluorescent data analysis software for the quantity identification of the composites in the material will be expressed.

Department:Physics.....

Field of study:Physics.....

Academic year:2009.....

Student's signature.....*Varalak Saengsuwan*.....

Advisor's signature.....*Thiti Bovornatanarak*.....

Co-advisor's signature.....*Wantana Klysubun*.....

Acknowledgments

The author gratefully acknowledge the support of all who have, directly or indirectly, contributed to this thesis.

First, my great appreciation is expressed to Asst. Prof. Dr. Thiti Bovornratanaraks , my thesis advisor, and Dr. Wantana Klysubun, my thesis co-advisor, for his/her attention, encouragement, considerate guidance and useful comments to make this thesis accomplished.

I wish to express my sincere appreciation to Asst. Prof. Dr. Kajornyod Yoodee for his considerate guidance and great helpful comments. My appreciation is also extended to the committees for inspecting and checking on my work very carefully.

I wish to express my sincere appreciation to the Synchrotron Light Research Institute (SLRI) Graduate Scholarship under Contract No.GS-48-D05, Chulalongkorn University Graduate School Thesis Grant, Graduate School, Department of Physics, Chulalongkorn University and also Office of the National Research Council of Thailand (NRCT) for their financial supports.

Moreover, I would like to express my appreciation to my teachers and my friends at Sainampeung School, Mahidol University, Chulalongkorn University and also SLRI staffs for their help and sincere friendship.

Finally, I wish to express my sincere gratitude to my parents and my sister for their love, support and encouragement to make me succeed.

Contents

Abstract (Thai)	iv
Abstract (English)	v
Acknowledgments	vi
Contents	vii
List of Tables	ix
List of Figures	xi
Chapter I Introduction	1
Chapter II Ray Tracing Simulation	9
2.1 Beamline Optics	9
2.1.1 Double Crystal Monochromator	9
2.1.2 Double Multilayer Monochromator	12
2.1.3 Collimating Mirror	13
2.1.4 Focusing Mirror	14
2.2 Total External Reflection and Mirror Reflectivity	15
Chapter III X-Ray Fluorescent Technique	19
3.1 Theory of X-Ray Fluorescence	19
3.1.1 Fluorescent Yield	22
3.1.2 White X-Ray Beam Filter	23
3.2 Si-PIN Detector	24
3.2.1 Energy Calibration using Polychromatic X-Rays	27
3.3 X-Ray Fluorescent Quantitative Analysis	31
3.4 XRF Analysis Software	32

3.5	X-Ray Fluorescent Imaging	33
3.5.1	Polycapillary X-Ray Optics	34
3.6	The Lower Limit of Detection	37
Chapter IV X-Ray Powder Diffraction Technique		39
4.1	Image Plate Area Detector	39
4.2	Crystal Structure Refinement	41
Chapter V Experimental Methods		47
5.1	X-Ray Fluorescent Analysis	47
5.2	X-Ray Fluorescent Imaging	50
5.3	X-Ray Powder Diffraction	57
Chapter VI Results and Discussions		64
6.1	Ray Tracing Simulation	64
6.2	X-Ray Fluorescent Analysis	79
6.3	X-Ray Fluorescent Imaging	82
6.4	X-Ray Powder Diffraction	98
Chapter VII Conclusions		103
7.1	Ray Tracing Simulation	103
7.2	X-Ray Fluorescent Technique	103
7.3	X-Ray Powder Diffraction Technique	104
References		105
Biography		114

List of Tables

Table	Page
2.1 DCM crystal and energy range at the XAS beamline BL8, Siam Photon Laboratory (http://www.slri.or.th)	10
2.2 Darwin width of perfect crystal [28]	11
3.1 Characteristic x-rays of the standard material.	28
3.2 Observed peak positions expressed in channel and photon energy that was calibrated using the quadratic equation for Ca, Ti, V, Cr, Mn, Fe, Ni, Cu and Zn. Peak area and the difference between the observed energy and the reference energy are also given.	29
3.3 Specifications of the Polycapillary half lens No.UNS1G-1F-171208 .	35
3.4 Detection limit for selected elements in different matrix.	38
4.1 Parameters refinable simultaneously	43
5.1 Widths (A, B) and spacing (C) of the nickel grid structure denoted in Figure 5.4(b).	52
5.2 Specifications of the Polycapillary half lens No.UNS1G-2T-170209 .	58
6.1 Parameters of synchrotron radiation source for designing x-ray beamline.	72
6.2 Parameters of optical elements	73
6.3 Peak fitting for a NIST SRM 610 multi-element glass calibration standard using the XRF analysis software.	82
6.4 Apparent widths (FWHM) for the fluorescent signal from Cu K_{α} for the Cu wire with ϕ 100 μm in horizontal (see Figure 6.19(a)) and vertical (see Figure 6.19(b)) directions for monochromatic beam.	85
6.5 Apparent widths (FWHM) for the fluorescent signal of Cu K_{α} (the Cu wire with ϕ 100 μm) in horizontal (see Figure 6.20(a)) and vertical (see Figure 6.20(b)) directions for white beam.	85

- 6.6 Apparent widths (FWHM) for the fluorescent signal of Cu K_{α} (the Cu wire with ϕ 25 μm) in horizontal (see Figure 6.21(a)) and vertical (see Figure 6.21(b)) directions for white beam. 88
- 6.7 Apparent widths (FWHM) for the fluorescent signal of Cu K_{α} (the Cu wire with ϕ 25 μm) in horizontal (see Figure 6.22(a)) and vertical (see Figure 6.22(b)) directions for white beam. 88
- 6.8 Setup No.1: widths (A, B) and spacing (C) of the nickel grid structure denoted in Figure 5.4(b). Widths (D) and spacing (E) of the fluorescent patterns in Figure 6.27. 95
- 6.9 Setup No.2: widths (A, B) and spacing (C) of the nickel grid structure. Widths (D) and spacing (E) of the fluorescent patterns. 96



ศูนย์วิทยทรัพยากร
จุฬาลงกรณ์มหาวิทยาลัย

List of Figures

Figure	Page
1.1 General electric synchrotron accelerator was built by Frank Elder, Anatole Gurewitsch, Robert Langmuir and Herb Pollock in 1946. [2]	2
1.2 Schematic diagram of accelerated electron up to several GeV by a synchrotron accelerator.	3
1.3 Characteristics of synchrotron radiation source. [5]	4
1.4 Siam Photon Laboratory. [6]	5
1.5 (a) Photograph of polycapillary x-ray optics (http://www.unisantis.com/kumakhov-optics.html) [24] and schematic drawing of (b) the Kirkpatrick-Baez mirror comprising of two grazing spherical or non-spherical mirrors for focusing in the light horizontally and vertically, respectively [25, 26] and (c) the Wolter mirror based on the total reflection of single metal layer mirrors [26, 27].	8
2.1 Preliminary design of beamline optics including a CM, a DCM and a FM in both top and side views.	10
2.2 Rocking curves or reflectivity curves of various perfect crystal reflections at a wavelength of 1.55 Å. FWHM of these curves are called rocking width or Darwin width, ω_D . [4, 28]	11
2.3 Schematic diagram of a double crystal monochromator	12
2.4 Schematic of a multilayer reflector of bilayer pairs of high- and low-Z materials (A and B).	13
2.5 Schematic diagram of a bent mirror for collimating the x-ray beam in the vertical plane.	14
2.6 Schematic diagram of a toroidal mirror for focusing the x-ray beam in both the horizontal and vertical directions.	15
2.7 Schematic diagram of the optical magnifications.	15

2.8	Glancing incident radiation and total external reflection for x-rays and EUV radiation.	16
2.9	Critical angle of Pt and Rh as a function of photon energy. For 20 keV, the critical angle are equal to 4.15 and 3.2 mrad for Pt and Rh, respectively.	17
2.10	Reflectivity for Rh 5 nm/Pt 25 nm/Si with binder layer Cr 5 nm. . .	18
3.1	Schematic diagram of interactions between x-rays and the matter . .	19
3.2	Schematic diagram of x-ray fluorescent emission of the sample. . . .	20
3.3	Fluorescent yields for x-ray emissions K, L and M shells as a function of atomic number. [32]	22
3.4	Photon counts as a function of atomic number.	23
3.5	(a) XRF spectra from sticky rice powder, (b) x-ray transmission for the aluminium filter with a thickness of 0.1 mm.	25
3.6	Connection diagram for XR-100CR as Si-PIN detector, PX2CR as pre-amplifier and power supply and MCA8000A as multi-channel analyser.	26
3.7	Setup for the energy calibration using characteristic x-rays of a metal foil as a calibration foil.	27
3.8	GaAs spectra with difference in volt pulse height and amplifier gain. .	28
3.9	Detected pulse height and photon energy is fitted using quadratic equation. Calibration elements are Ca, Ti, V, Cr, Mn, Fe, Ni, Cu and Zn.	30
3.10	Calibrated XRF spectra for standard material with recorded time of 180 s.	30
3.11	Algorithm for XRF analysis software	33
3.12	Schematic representation of the principles of capillary optics. [26] . .	35
3.13	Polycapillary x-ray optics; (a) focusing lens, (b) half focusing lens and (c) parallel beam lens. [26]	36
4.1	Bragg's Law	40

4.2	Schematic diagram of image plate method in high-pressure re- search. [59].	41
4.3	Gaussian function (solid line), the Lorentzian function (long dash line) and the pseudo - Voigt function (short dash line) for $y_0 = 1$, $x_c = 2$, $A = 5$ and $w = 1.5$	45
5.1	Schematic diagram of the experimental setup for XRF analysis. . .	47
5.2	Experimental XRF spectrum from a NIST SRM 610 standard with a white beam and measurement time 2000 s.	49
5.3	Schematic diagram of the experimental setup for XRF imaging at the Siam Photon Laboratory;(a) the setup No.1 and (b) the setup No.2.	51
5.4	Patterns 1-4 and magnified structures of nickel grids on supporting glass.	53
5.5	Photograph of the test object made of copper (seen in orange) and cobalt (gray) foils.	54
5.6	Defining scanned area (left). Sample was placed in the scanned area (right).	55
5.7	Sample holder with Ni mesh over a fluorescent screen.	55
5.8	Capture photo for Ni mesh by CCD camera. A green spot represents the position of x-ray beam on the screen.	56
5.9	Fluorescent signal from Ni K_α for both x (left) and y (right) scans.	56
5.10	Picture frame versus motor frame.	56
5.11	Setup for x-ray powder diffraction technique under extreme condi- tions on the beamline BL-8 at the Siam Photon Laboratory.	57
5.12	Setup for x-ray powder diffraction technique under extreme condi- tions using the polycapillary lens on the beamline BL-2 at the Siam Photon Laboratory.	59

5.13 R-line fluorescences of a ruby crystal in the DAC at room temperature are shown; ruby crystal: at ambient pressure (A); at about 22.3 kbar (B); at about 40 kbar (C). The pressure shift is to lower energy with increasing pressure. [70]	60
5.14 Old micro-EDM used at the Extreme Condition Physics Research Laboratory, Chulalongkorn University.	61
5.15 Schematic layout for drilling machine.	62
5.16 Schematic diagram of the drilling circuit.	62
5.17 New micro-EDM.	63
6.1 Complete diffraction pattern of the hexagonal phase of ZnO under ambient condition at beamline BL8.	64
6.2 Schematic layout of the proposed XRPD beamline for the Siam Photon Laboratory.	65
6.3 Comparison of simulated photon flux between DCM: Ge(220) and DMM: W/B_4C ML for a photon energy range of 5-12 keV and opening angle of $1.75(\text{h}) \times 0.125(\text{v})$ mrad ² is shown in (a). Reflectivity of W/B_4C ML with $d = 10 \text{ \AA}$, $N = 600$ and $\Gamma = 0.5$ is shown in (b).	66
6.4 Simulated rocking curve for the DMM with W/B_4C ML at 9 keV.	67
6.5 Calculated reflectivity of Rh 5 nm/ Pt 25 nm coated on silicon mirror with $\theta_c = 3, 5$ and 7 mrad.	67
6.6 Image size at focal plane for the mirror magnifications M0.3, M0.4, M0.5, M0.6 and M0.7.	69
6.7 Beam convergence at focal plane for the mirror magnifications M0.3, M0.4, M0.5, M0.6 and M0.7.	70
6.8 Layout for beamline design of the unfocused and focused monochromatic beam for x-ray absorption spectroscopy and x-ray fluorescent techniques.	71

6.9	Reflectivity for Si with glancing angle of 3 mrad, Rh with glancing angle of 5 mrad and Rh 5/Pt 25 nm with glancing angle of 6 mrad for a photon energy range of 1-15 keV.	74
6.10	Reflectivity for Si with a glancing angle of 3 mrad for a photon energy range of 1000-3000 eV.	74
6.11	Reflectivity for Rh 5/Pt 25 nm with a glancing angle of 6 mrad for a photon energy range of 1400-3000 eV.	75
6.12	Reflectivity for Rh with a glancing angle of 5 mrad and Rh 5/Pt 25 nm with a glancing angle of 6 mrad for a photon energy range of 2300-6700 eV.	75
6.13	Image size at focal plane.	76
6.14	Beam convergence at focal plane.	77
6.15	(a) Flux at sample and (b) energy resolution for all cases of beamline designs.	78
6.16	(a) XRF spectrum of Cd in sticky rice powder and (b) Calibration curve derived from the sticky rice standards with varying Cd concentrations.	80
6.17	Calibration curve derived from the sticky rice standards with varying Cd concentrations. The experiment was repeated using white beam at the beamline BL6.	81
6.18	Experimental setup for testing the polycapillary half lens No.208 using monochromatic x-rays with a photon energy of 9.5 keV at beamline BL2	83
6.19	Fluorescent signal from Cu K_{α} for the Cu wire with ϕ 100 μm normalized by the electron beam current scanned in (a) the horizontal direction (x) and (b) the vertical direction (z) for monochromatic x-ray beam. The step size is 50 μm and the counting time is 30 s/step.	84

6.20	Fluorescent signal from Cu K_{α} for the Cu wire with ϕ 100 μm normalized by the electron beam current scanned in (a) the horizontal direction (x) and (b) the vertical direction (z) for white beam. The step size is 50 μm and the counting time is 30 s/step.	86
6.21	Fluorescent signal from Cu K_{α} for the Cu wire with ϕ 25 μm normalized by the electron beam current scanned in (a) the horizontal direction (x) and (b) the vertical direction (z) for white beam. The step size is 20 μm and the counting time is 30 s/step.	87
6.22	Fluorescent signal from Ti K_{α} normalized by the electron beam current scanned in (a) the horizontal direction (x) and (b) the vertical direction (z) for white beam. The step size is 20 μm and the counting time is 30 s/step.	89
6.23	XRF images of copper for 1 st and 2 nd scans. The step size is 150 μm , the counting time is 10 s/step and the scanned area is 6000 \times 6000 μm^2	90
6.24	Imaging scans of a sharks fang fossil being preserved in rock. (a) Captured photo by the CCD camera (b) the information of Fe K_{α} in the sample. The step size is 150 μm , the counting time is 10 s/step and the scanned area (red boundary) is 5000 \times 5000 μm^2	91
6.25	(a) Photo of the rice grain, (b) the information of Cd L_{α} for the sample. The step size is 150 μm , the counting time is 10 s/step and the scanned area (red boundary) is 300 \times 11000 μm^2	92
6.26	XRF images of the nickel mesh for 1 st and 2 nd scans. The step size is 100 μm , the counting time is 5 s/step and the scanned area is 5.04(x) \times 4.6(y) mm ² . The image (b) was rotated by 0.573 degree (clockwise).	93
6.27	Spatial profiles of Ni K_{α} recorded from the grid patterns.	94
6.28	New apparatus (No.2) for one dimensional testing (left). Focused white beam (red circle) on the Ni grid pattern 1 (right).	96

- 6.29 (a) Photograph of the test object made of copper (seen in orange) and cobalt (gray) foils. XRF Images (b) and (c) of copper and cobalt, respectively. The step size is $150 \mu\text{m}$, the counting time is 10 s/step and the scanned area is $6000 \mu\text{m} \times 6000 \mu\text{m}$ 97
- 6.30 X-ray transmission for (a) the diamond culets with thickness of $4000 \mu\text{m}$ and (b) air with path length 100 cm. 99
- 6.31 X-ray powder diffraction pattern for CeO_2 under high pressure. Recorded time are (a) 3 (b and c) 4 hrs. 100
- 6.32 X-ray powder diffraction pattern for Al_2O_3 at ambient condition. Recorded time are (a) 4 and (b) 2.5 hrs. 101
- 6.33 X-ray powder diffraction pattern for CeO_2 at ambient condition. Recorded time is (a) 2.5, (b) 3 and (c) 4 hrs. 102

CHAPTER I

INTRODUCTION

Synchrotron radiation (SR), an emitted electromagnetic radiation from high energy accelerated electrons in a storage ring, plays an important role in several research areas including pure science and emerging technologies — nanotechnology, biotechnology, cognitive science, robotics and artificial intelligence. The radiation was discovered in a general electric synchrotron accelerator as shown in Figure 1.1 by Frank Elder, Anatole Gurewitsch, Robert Langmuir and Herb Pollock in 1946. Pollock described that on 24 April 1946 they discovered some intermittent sparking, called synchrotron radiation, during running the machine. Moreover, SR can also be generated by astronomical objects — relativistic electrons spiral through magnetic fields — which was first detected by Geoffrey R. Burbidge in 1956 in a jet emitted by Messier 87 [1], the largest and brightest galaxy within the northern Virgo Cluster located about 55 million light years away.

SR is widely used than electromagnetic radiation from conventional sources because it has better properties such as 1) narrow angular collimation and small source size, 2) large energy range with very broad continuous spectrum with the photon energy ranging from infrared to hard x-rays, 3) high intensity and high flux, 4) regularly pulsed time structure, 5) high degree of linear/circular polarization and 6) computability of properties as described in Figure 1.2. SR source can be divided into three types according to period and strength of magnets:

1. Bending magnet or dipole magnet source comprises of two magnets with north and south poles facing each other. The radiation from the bending magnet source has a Gaussian distribution. Photon energy is continuous as expressed in Figure 1.3. The opening angle of the radiation, $\frac{1}{\gamma}$, depends on energy of electrons in the storage ring by the following equation

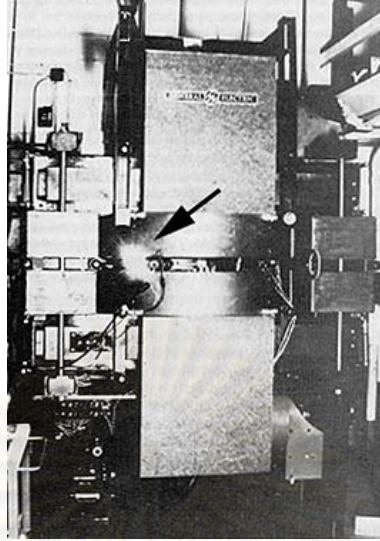


Figure 1.1: General electric synchrotron accelerator was built by Frank Elder, Anatole Gurewitsch, Robert Langmuir and Herb Pollock in 1946. [2]

$$\frac{1}{\gamma} = \frac{mc^2}{E_e} = \frac{1}{1.957E_e[\text{GeV}]} \quad (1.1)$$

where E_e is the energy of electrons in the storage ring. For the Siam Photon Source, $E_e = 1.2 \text{ GeV}$, then $\frac{1}{\gamma} = 0.426 \text{ mrad}$.

2. Wiggler is an insertion device installed in a straight section of a storage ring. The source is composed of many periods of strong dipole magnets with alternating magnetic field directions which are arrayed in a straight line. The radiation from the wiggler source is also continuous as shown in Figure 1.3. Horizontal beam divergence is much larger than that of the bending magnet source. If the wiggler source is composed of N periods of dipole magnets, photon flux will be $2N$ times higher than that of the dipole magnet source.
3. Undulator source is closely similar to the wiggler source, but the dipole magnetic fields are weaker and the number of periods is a lot higher. The radiation from the undulator source is quasi-monochromatic as presented in Figure 1.3. Photon flux is discrete because the radiation from each period of dipole magnets interfere. Because of radiation interference, photon flux is

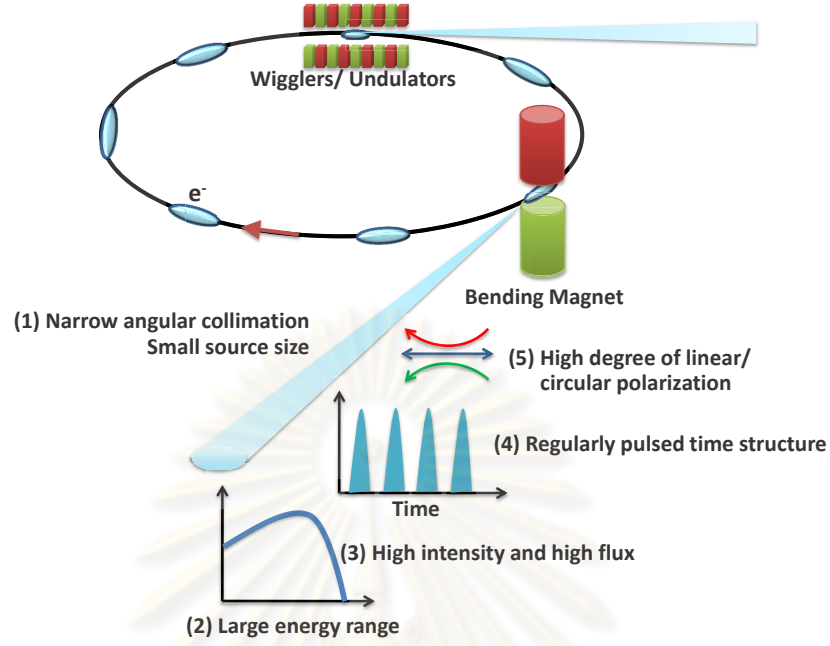


Figure 1.2: Schematic diagram of accelerated electron up to several GeV by a synchrotron accelerator.

N^2 times higher than that of the dipole magnet source.

Characteristics of the synchrotron radiation can be described with the brilliance, photon density and photon flux. Each quantity can be defined by the following equations [3, 4]

$$Brilliance = \frac{\text{number of photons}}{s \cdot \sigma_x \cdot \sigma_z \cdot \varphi_x \cdot \varphi_z \cdot 0.1\% \text{ bandwidth}} \quad (1.2)$$

$$Intensity = \frac{\text{number of photons}}{s \cdot \varphi_x \cdot \varphi_z \cdot 0.1\% \text{ bandwidth}} \quad (1.3)$$

$$Flux = \frac{\text{number of photons}}{s \cdot 0.1\% \text{ bandwidth}} \quad (1.4)$$

where $\sigma_{x,z}$ is the source size and $\varphi_{x,z}$ is the beam divergence. Subscripts x and z denote horizontal and vertical directions, respectively.

Currently, the Siam Photon Source consists of eight bending magnets as presented in Figure 1.4 with the stored electron beam energy of 1.2 GeV and the stored

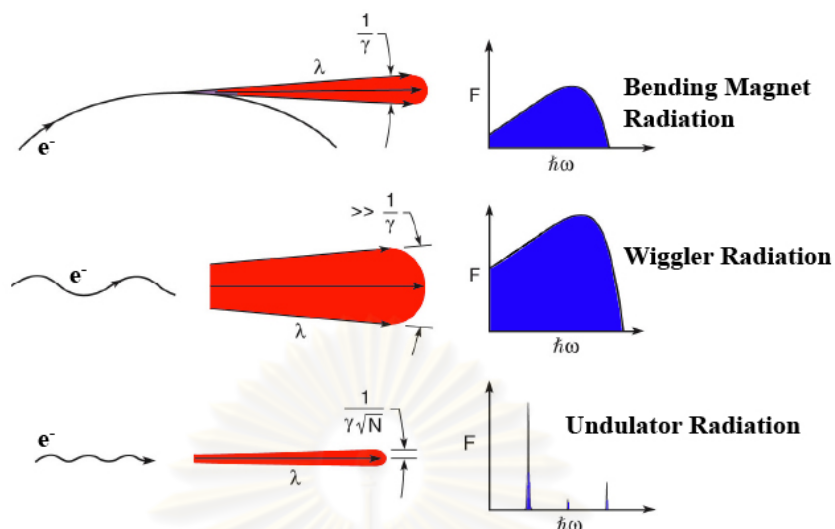


Figure 1.3: Characteristics of synchrotron radiation source. [5]

beam current of 150 - 100 mA. There are two operated bending magnet beamlines including x-ray lithography for micro-machining at the beamline BL6 and x-ray absorption spectroscopy (XAS) for chemical and structural analyses at the beamline BL8. In addition, the planar undulator beamline BL3 are under constructed for VUV & soft x-ray photoemission spectroscopy, nano x-ray photoelectron spectroscopy (nano-XPS), nano x-ray absorption spectroscopy (nano-XAS) and also photoemission electron microscopy (PEEM) in order to support the applications in solid state spectroscopy, surface analysis, absorption spectroscopy and microscopy. The 6.4-tesla superconducting wavelength shifter (WLS) beamline BL7.2 is also under constructed for protein crystallography (PX), XAS, small and wide angle x-ray scattering (SAXS & WAXS).

In this thesis, the design of x-ray optical systems by ray tracing simulation for x-ray powder diffraction under high pressure condition, XAS and x-ray fluorescent techniques developed for the Siam Photon Laboratory will be presented. The results from the simulation which are described in terms of reflectivity, collimating and focusing properties of the mirror, required focal size, photon flux at sample and energy resolution for further optimization of the beamline will be described in chapter 2. The related theories for ray tracing simulation are also explained.

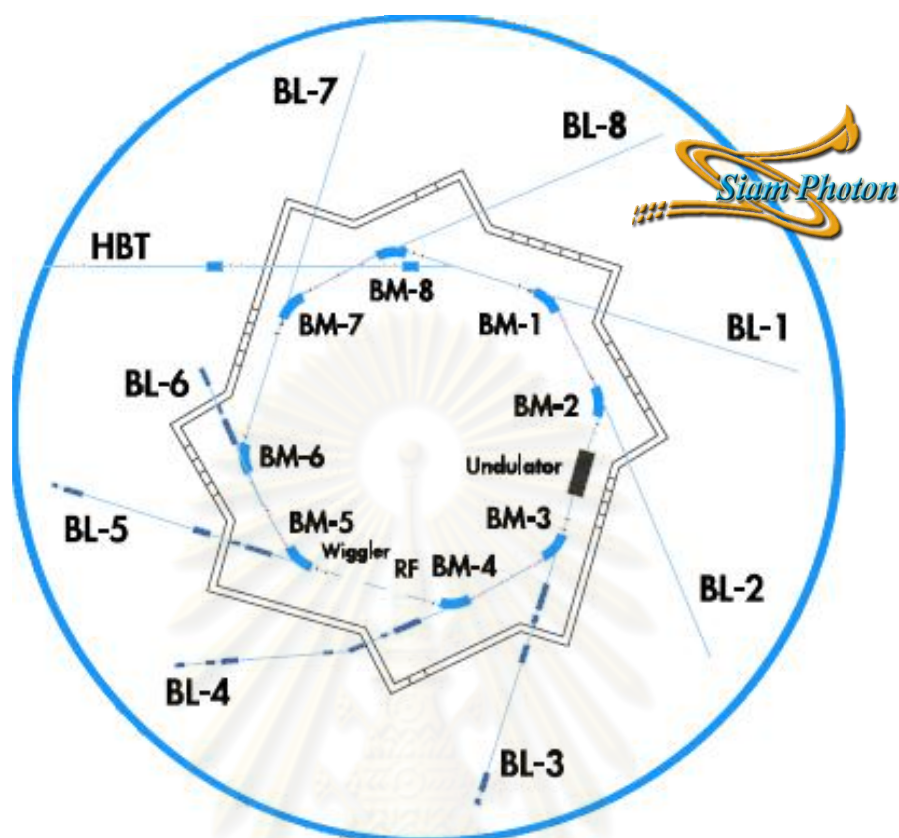


Figure 1.4: Siam Photon Laboratory. [6]

This thesis also developed two techniques used for synchrotron radiation: x-ray fluorescence (XRF) and x-ray powder diffraction (XRPD) under high pressure condition. XRF techniques including XRF analysis and XRF imaging are widely used in several research disciplines. XRF analysis is well-known for elemental identification and quantification while XRF imaging or mapping provides information on the spatial distribution of elements. XRF imaging is often used in several applications, for example, pharmaceuticals, geology, archaeology, electronics and life sciences. Both monochromatic x-rays and polychromatic x-rays (white x-ray beam) can be used for elemental excitation. Many types of x-ray optics are employed as presented in Figure 1.5, e.g., polycapillary x-ray optics described in chapter 3, Kirkpatrick-Baez mirror and Wolter mirror, for focusing the x-ray beam that is necessary for XRF imaging. Moreover, ultra-narrow spot sizes are

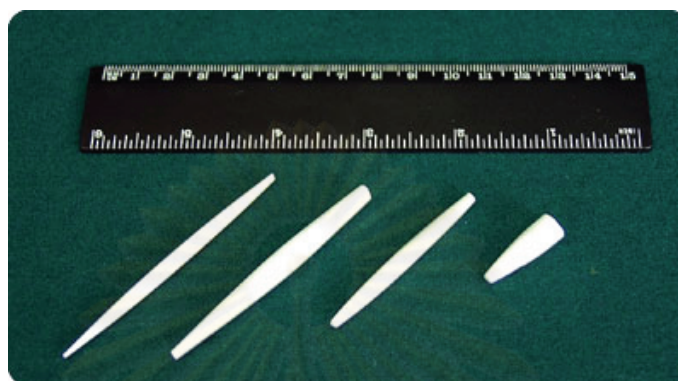
achievable nowadays at synchrotron facilities allowing qualitative and quantitative characterization of particles with micrometer and even down to nanometer size [7, 8]. In order to support various applications in x-ray micro analysis such as x-ray micro-tomography [9], x-ray microprobe [10] and inorganic elemental analysis [11, 12], the XRF technique at the Siam Photon Laboratory has been developed. A white x-ray beam delivered from a bending magnet beamline and with a critical photon energy of 1.4 keV was used for excitation. The experimental setup and test results on the XRF analyses of a standard containing a number of trace elements, a sticky rice sample with metal contamination and also various dimension of nickel grids on supporting glass and bi-metal structures were reported in chapter 3. A necessary XRF data analysis software for the quantity identification of the composites in the material will also be expressed.

X-ray powder diffraction under high-pressure conditions using synchrotron radiation based on station 9.1 at the Daresbury Synchrotron Radiation Source [13] was developed at the Siam Photon Laboratory [6] for expanding the understanding of physical and chemical properties of materials. In our recent work, we have recorded the complete two dimensional diffraction pattern of the hexagonal phase of ZnO at the beamline BL8 using an image plate area detector. However, the diffraction intensity could have been improved significantly if there were focusing optics to converge the whole x-ray beam onto the sample in the diamond anvil cell (DAC). In addition, some intensity loss by x-ray absorption in the DAC at 9 keV is expected. This can be compensated by higher flux. Expected performance of the proposed XRPD beamline was determined by ray tracing simulation with the aid of SHADOW [14]. The x-ray beam simulated for the bending magnet source was traced through each optic and characterized in terms of photon flux, beam size, beam convergence and energy resolution. As compared to a Ge(220) double crystal monochromator (DCM) used at the beamline BL8 of the Siam Photon Laboratory [15], higher photon flux can be obtained from a double multilayer monochromator (DMM), which plays a vital role in the high flux applications, for

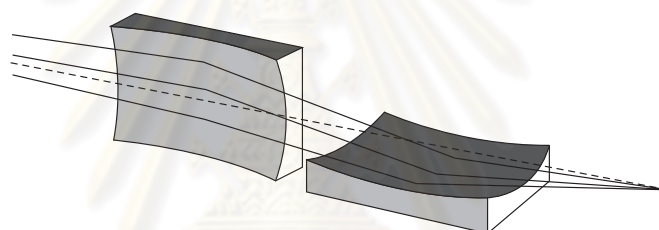
example, XRPD technique, microscopic x-ray fluorescence analysis, small-angle x-ray scattering technique and x-ray topography [16]. We consider a W/B₄C DMM [17–20] that is employed in a superconducting bending magnet beamline for high-pressure studies at the Advanced Light Source [21] and a microscopic XRD at HASYLAB [22]. Moreover, we can also focus the x-ray beams using the x-ray optics. One of the most easiest apparatus for focussing the x-ray beams to the high pressure cell is a polycapillary x-ray optics [23]. The examinations for XRPD using a polycapillary x-ray optics are implied in chapter 4.

Results and discussions are presented in chapter 5 and finally conclusions and future work are implied in the last chapter.

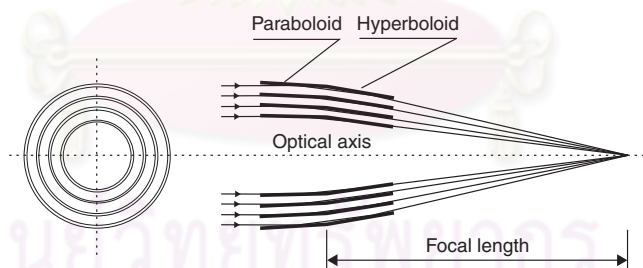




(a)



(b)



(c)

Figure 1.5: (a) Photograph of polycapillary x-ray optics (<http://www.unisantis.com/kumakhov-optics.html>) [24] and schematic drawing of (b) the Kirkpatrick-Baez mirror comprising of two grazing spherical or non-spherical mirrors for focusing in the light horizontally and vertically, respectively [25, 26] and (c) the Wolter mirror based on the total reflection of single metal layer mirrors [26, 27].

CHAPTER II

RAY TRACING SIMULATION

Ray tracing is a powerful simulation tool for studying and designing x-ray optical systems especially for synchrotron radiation beamline. A powerful simulation method, ray tracing, is used for studying and designing x-ray optical systems especially for synchrotron radiation beamline. In this research, the computer simulation program called SHADOW is used for configuring the x-ray beamline.

2.1 Beamline Optics

A preliminary design of the optical beamline is presented in Figure 2.1. The x-ray beam is collimated in the vertical plane by a collimating mirror (CM) and monochromatized by a double crystal monochromator (DCM). Beryllium windows are used for filtering out the low-energy x-rays and for isolating vacuum between the beamline and the storage ring where the source is located. Rectangular slits are utilized for defining the beam size and the beam divergence. The x-ray beam is focused on the sample position by the second mirror called a focusing mirror (FM). Optical properties of CM and FM are based on total external reflection. The mirrors made of silicon coated with higher atomic-number metals, e.g., platinum, rhodium and gold, for providing the reflection at greater incident angles and higher photon energies. Total external reflection and mirror reflectivity will be discussed later in the next section.

2.1.1 Double Crystal Monochromator

Double crystal monochromator is commonly employed in x-ray beamlines for selecting photon energy of the x-ray beam. The important major factors for choosing a suitable pair of crystals for each experiment are the photon energy range of interest and the intrinsic resolution of the crystal. For example, hard x-ray beamline for protein crystallography at the Siam Photon Laboratory desires energy resolution below 2×10^{-4} and photon energy range of 5 - 20 keV. Therefore,

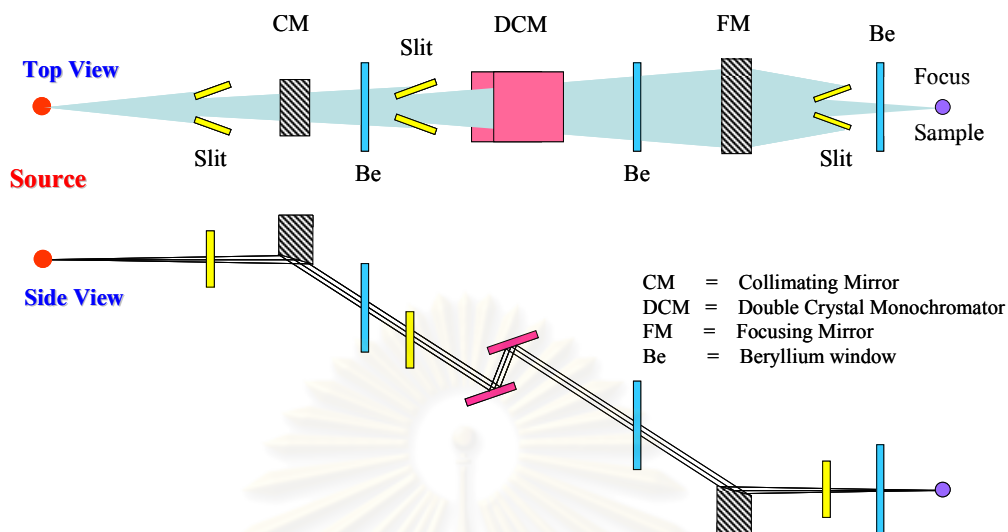


Figure 2.1: Preliminary design of beamline optics including a CM, a DCM and a FM in both top and side views.

Si(111) crystal is suitable for this technique. X-ray absorption spectroscopy technique for chemical and structural analyses at Siam Photon Laboratory delivers monochromatic x-rays with energy resolution between 1×10^{-4} to 3×10^{-4} and photon energy range of 1.25 eV - 10 keV. Hence, the suitable crystals are shown in Table 2.1.

Table 2.1: DCM crystal and energy range at the XAS beamline BL8, Siam Photon Laboratory (<http://www.slri.or.th>)

Crystal type	2d spacing (Å)	Photon energy range (eV)
KTP(011)	10.955	1250 - 4780
InSb(111)	7.481	1830 - 7000
Si(111)	6.271	2180 - 8350
Ge(220)	4.001	3440 - 10000

The energy resolution of the beam diffracted by the crystal depends on both natural divergence of the incident beam and the FWHM of the rocking curve of the crystal called rocking width or Darwin width. The Darwin width of the crystal,

$\frac{\delta\lambda}{\lambda}$, can be written as

$$\frac{\delta\lambda}{\lambda} = \omega_D \cot \theta_B = \frac{d^2}{\epsilon_0 \pi^2} \frac{e^2}{mc^2} \frac{|F(h)|}{V_0} \quad (2.1)$$

where ω_D is the Darwin width of a perfect crystal derived from diffraction theory and $|F(h)|$ is the structure factor amplitude. Figure 2.2 and Table 2.2 presents the Darwin width for some popular perfect crystal including Si(111), Si(220), Ge(111), Ge(220) and pyrolytic graphite.

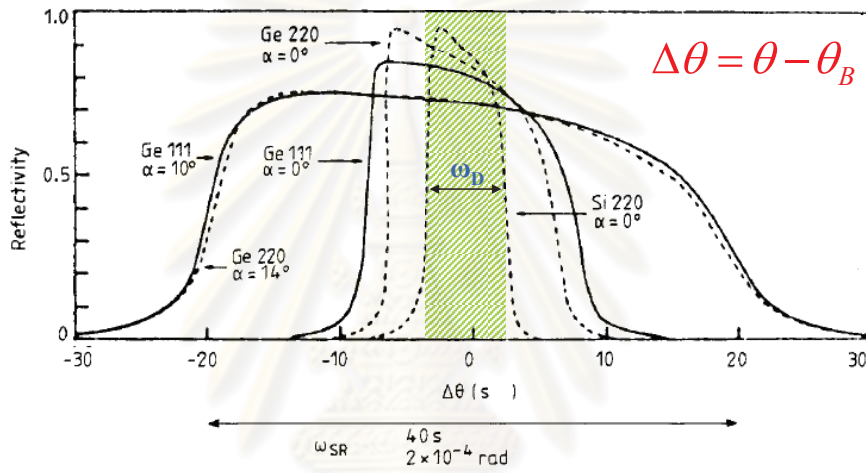


Figure 2.2: Rocking curves or reflectivity curves of various perfect crystal reflections at a wavelength of 1.55 \AA . FWHM of these curves are called rocking width or Darwin width, ω_D . [4, 28]

Table 2.2: Darwin width of perfect crystal [28]

Type	Reflection	$\frac{\delta\lambda}{\lambda}$
Silicon	(111)	1.33×10^{-4}
Silicon	(220)	5.6×10^{-5}
Germanium	(111)	3.2×10^{-4}
Germanium	(220)	1.5×10^{-4}
Pyrolytic graphite	0.5° mosaic spread	3.8×10^{-2}

Figure 2.3 illustrates an incident white x-ray beam (polychromatic x-rays) on double crystals. A white beam is monochromatized by Bragg's law:

$$2d_{hkl} \sin \theta_B = \lambda \quad (2.2)$$

where θ_B is the incident angle measured relative to the crystal surface, i.e., the

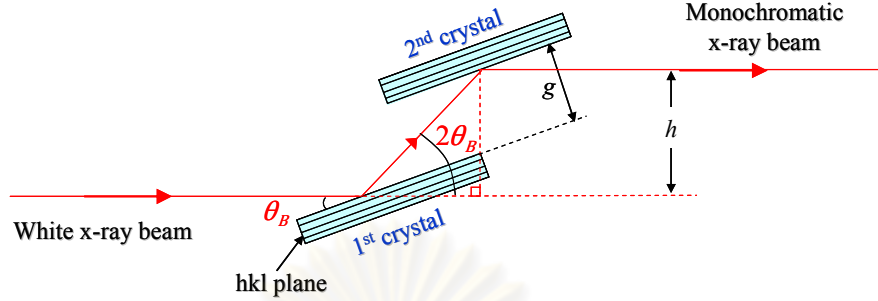


Figure 2.3: Schematic diagram of a double crystal monochromator

Bragg angle, d_{hkl} is the hkl plane spacing of the crystal and λ is the wavelength of the monochromatic x-ray beam. The values g and h are the gap between two crystals and the beam offset, respectively. The conversion between the wavelength, $\lambda(\text{\AA})$, and photon energy, $E(\text{keV})$, is given by

$$\lambda(\text{\AA}) = \frac{12.39841}{E(\text{keV})}. \quad (2.3)$$

In the case of soft x-ray beamline, we can increase the photon flux using double multilayer monochromator (DMM) as discussed in the next section.

2.1.2 Double Multilayer Monochromator

Double multilayer monochromator is ordinary utilized for tuning the incident photon energy. Because of its wide band pass, the multilayers can enhance the performance of the measurement by increasing the photon flux for x-rays, soft x-rays, and extreme ultraviolet (EUV) beamline as indicated in Ref. [29]. The multilayers consist of alternating layers of high- and low- Z materials, for example, Mo/Be , Mo/Si and W/B_4C with a constant thickness ratio (Γ) of the order of nanometres. Figure 2.4 describes that the multilayers with a constant d-spacing (total thickness of a pair of bilayer) adjust the incident photon energy by varying the incident angle (θ) as given by Bragg's law.

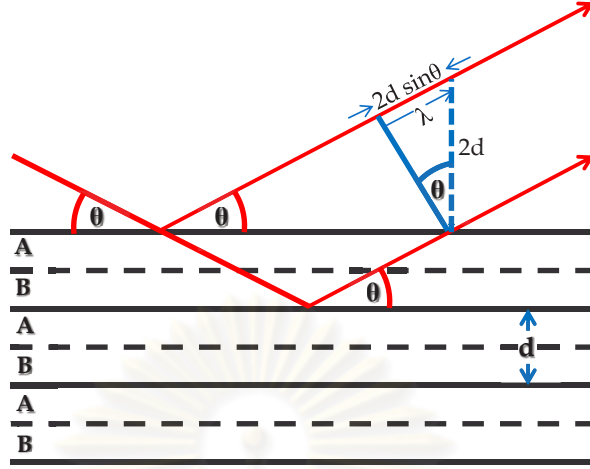


Figure 2.4: Schematic of a multilayer reflector of bilayer pairs of high- and low-Z materials (A and B).

2.1.3 Collimating Mirror

Collimating Mirror, a flat mirror bent or ground to a radius R , is customarily used for collimating the x-ray beam in the vertical plane before entering a DCM as presented in Figure 2.1. The meridional radius (R) of the mirror can be calculated by

$$\frac{1}{R} = \left(\frac{1}{r_1} + \frac{1}{r_2} \right) \frac{\sin \theta}{2} \quad (2.4)$$

where r_1 and r_2 are the source and the image plane distances, respectively. Here θ is a glancing angle between the x-ray beam and the mirror surface. In order to make total external reflection occur, a ray of light is designed to strike a medium boundary at an angle larger than a particular critical angle with respect to the perpendicular direction of the mirror surface. To collimate the beam in the vertical plane as described in Figure 2.5, the radius of the mirror can be calculated by assuming the image plane distance at infinity:

$$r_{2,CM} \rightarrow \infty \Rightarrow R_{CM} = \frac{2r_{1,CM}}{\sin \theta}. \quad (2.5)$$

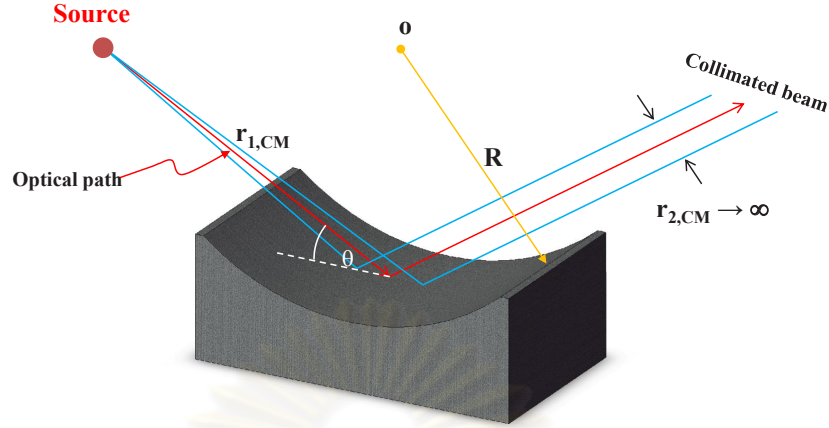


Figure 2.5: Schematic diagram of a bent mirror for collimating the x-ray beam in the vertical plane.

2.1.4 Focusing Mirror

Focusing mirror is a toroidal mirror or a bent cylindrical mirror as shown in Figure 2.6. A meridional curvature of radius R and a sagittal curvature of radius ρ of the mirror focus the beam in the vertical and the horizontal planes, respectively. The radii R and ρ are given by

$$\begin{aligned} \frac{1}{R} &= \left(\frac{1}{r_1} + \frac{1}{r_2} \right) \frac{\sin \theta}{2} \\ \frac{1}{\rho} &= \left(\frac{1}{r_1} + \frac{1}{r_2} \right) \frac{1}{2 \sin \theta}. \end{aligned} \quad (2.6)$$

In order to focus the collimated x-ray beam in the vertical plane after monochromatizing by the DCM, the meridional radius of the focusing mirror is obtained by assuming the source plane distance at infinity:

$$r_{1,FM} \rightarrow \infty \Rightarrow R_{FM} = \frac{2r_{2,FM}}{\sin \theta}. \quad (2.7)$$

For beamline design, the optical magnifications are selected such that the image or focused beam size and beam divergence are suitable for a particular experimental technique. Moreover, aberration of the focused beam size and beam divergence for each beamline design will be considered. The optical magnifications of the beamline optics are illustrated in Figure 2.7. The horizontal and the vertical

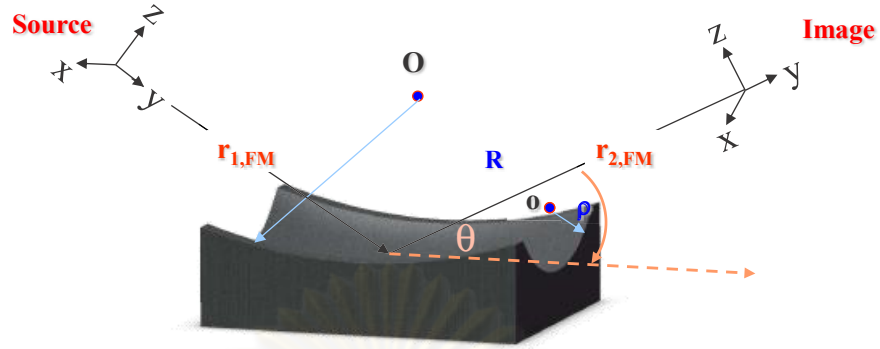


Figure 2.6: Schematic diagram of a toroidal mirror for focusing the x-ray beam in both the horizontal and vertical directions.

magnifications (M_x and M_z) depend on the source and the image plane distances as well as the beam divergences. They are given by

$$\begin{aligned} M_x &= \frac{r_{2,FM}}{r_{1,FM}} = \frac{x'_1}{x_2} \\ M_z &= \frac{r_{2,FM}}{r_{1,CM}} = \frac{z'_1}{z_2} \end{aligned} \quad (2.8)$$

where x'_1 and x'_2 are the horizontal beam divergences of the source and the image, respectively. z'_1 and z'_2 are the vertical beam divergences of the source and the image, respectively.

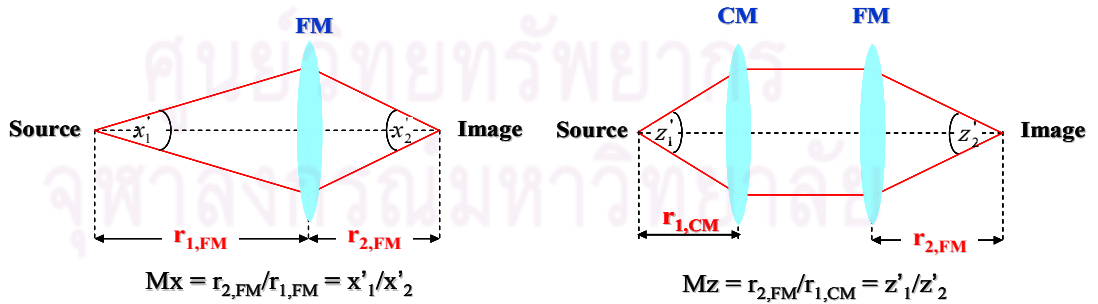


Figure 2.7: Schematic diagram of the optical magnifications.

2.2 Total External Reflection and Mirror Reflectivity

Total external reflection is generally used in several purposes, for example, radiation transport, deflection and focusing of x-ray beams. Physics of the light

reflection is based on Snell's law which demonstrates that visible light entering a medium of greater refractive index will be bent to the surface normal. Nevertheless, Snell's law demonstrates that x-rays and extreme ultraviolet (EUV) radiation is refracted further to the surface normal because the real part of the refractive index slightly less than unity. This total external reflection can occur in the case of an incident angle (θ) is less than a critical angle (θ_c) as presented in Figure 2.8.

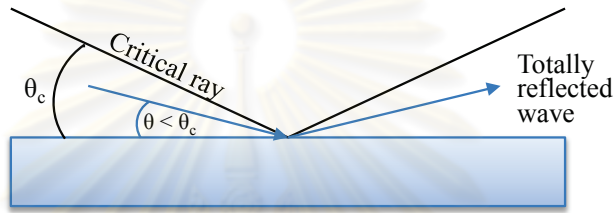


Figure 2.8: Glancing incident radiation and total external reflection for x-rays and EUV radiation.

The reflectivity of the perfectly smooth homogeneous mirror surface can be calculated by

$$R \approx \frac{h - \frac{\theta}{\theta_c} \sqrt{2(h-1)}}{h + \frac{\theta}{\theta_c} \sqrt{2(h-1)}} \quad (2.9)$$

where h is $(\frac{\theta}{\theta_c})^2 + \sqrt{[(\frac{\theta}{\theta_c})^2 - 1]^2 + (\frac{\beta}{\delta})^2}$, θ is incident angle and θ_c is critical angle, δ and β are the refractive-index real and imaginary components of material. The real part of the refractive index, δ , can be written as

$$\delta = \frac{N(\frac{Z}{A}) \cdot \rho e^2 \lambda^2}{2\pi m c^2} \beta = \frac{\mu \lambda}{4\pi} n = N(\frac{Z}{A}) \cdot \rho \quad (2.10)$$

where N is avocadro number, Z is atomic number, A is atomic mass, ρ is density of material, λ is wavelength of the incident beam and μ is linear absorption coefficient. The critical angle can be obtained from Snell's law and the refractive index,

$$n = 1 - \delta + i\beta \approx \cos \theta_c. \quad (2.11)$$

For simplify problem, β approaches zero . For x-rays, we can make an approximation for very small θ_c , $1 - \frac{\theta_c^2}{2} + \dots = 1 - \delta$, since $\delta \ll 1$,

$$\theta_c = \sqrt{2\delta} = 2.99 \times 10^{-23} \sqrt{n} \lambda (\text{\AA}). \quad (2.12)$$

Equation 2.12 indicates that the critical angle of each material depends on photon energy of the incident beam and others. In order to choose higher atomic number material for coating on silicon mirror, i.e., CM and FM, we have to concern about the reflectivity of each glancing-incidence angle and the photon energy range of interest for coated material. When a glancing-incidence angle is too small (less than 3 mrad), we have to use very long mirror (more than one meter) for matching with the size of incident rays. Figure 2.9 shows the relation between photon energy of the incident beam and critical angle for platinum (Pt) and rhodium (Rh). For a photon energy of 20 keV, we have to choose the glancing-incidence angle below 4.15 and 3.2 mrad for Pt and Rh, respectively.

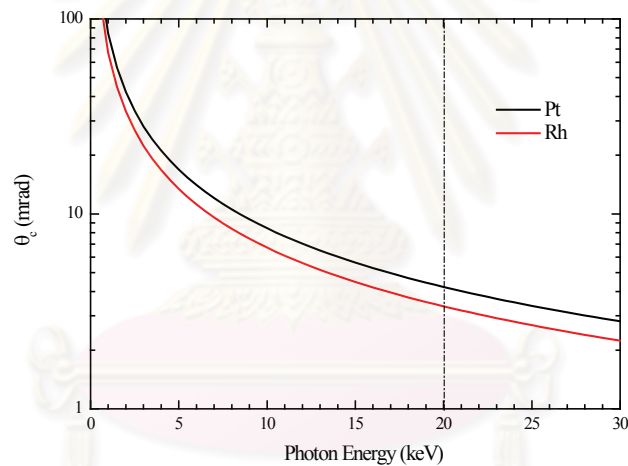


Figure 2.9: Critical angle of Pt and Rh as a function of photon energy. For 20 keV, the critical angle are equal to 4.15 and 3.2 mrad for Pt and Rh, respectively.

Figure 2.10 presents reflectivity for various coated materials — rhodium (Rh), platinum (Pt), chromium (Cr) — and thickness dependence on silicon mirror with a glancing-incidence angle of 3.5 mrad for both single and binary coatings. According to the graph, Rh 5 nm/ Pt 25 nm coated on Si is most suitable for working with photon energy of the incident beam between 5 - 20 keV.

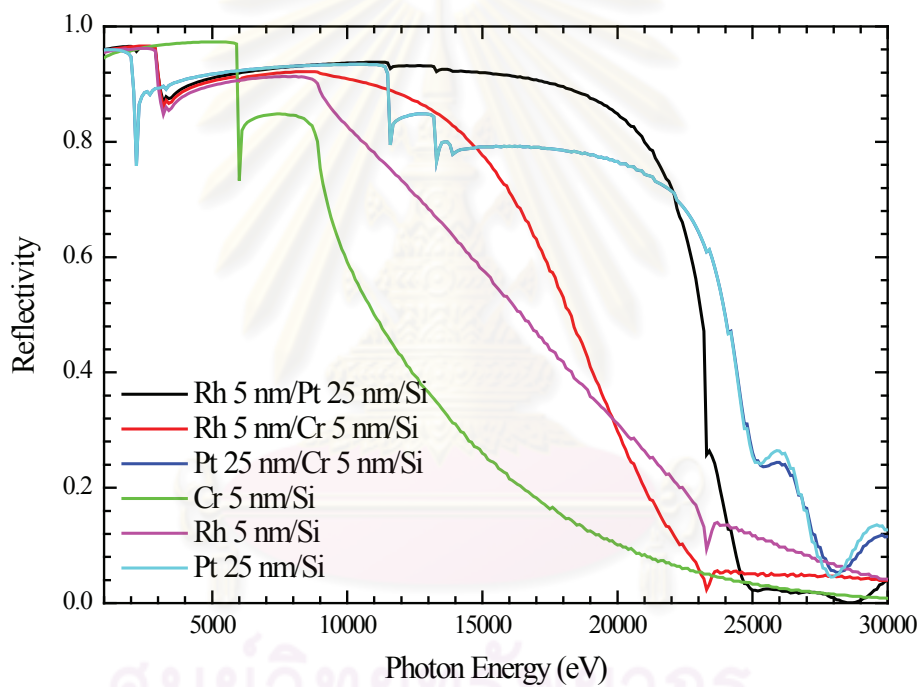


Figure 2.10: Reflectivity for Rh 5 nm/Pt 25 nm/Si with binder layer Cr 5 nm.

CHAPTER III

X-RAY FLUORESCENT TECHNIQUE

X-ray Fluorescence (XRF) analysis is the x-ray emission technique which is widely used in several research areas for elemental identification and quantification without destruction of the sample. This technique is based on a measurement of the energies and the intensities of the emitted characteristic x-rays from the excited sample. The measurement of x-ray intensity is proportional to the concentration of the element and the strength of the excitation source.

3.1 Theory of X-Ray Fluorescence

When x-ray beam is incident on the matter, the photoelectron emission, Compton scattering, Rayleigh scattering, x-ray transmission and x-ray fluorescence are occurred as shown in Figure 3.1.

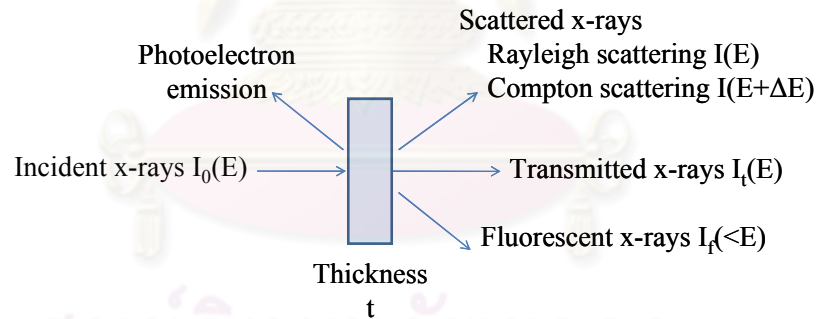


Figure 3.1: Schematic diagram of interactions between x-rays and the matter

The intensity $I(E)$ of the transmitted x-rays with photon energy E , when passing through the sample with the element i , thickness t and density ρ_i is given by

$$I(E) = I_0 e^{-\mu_i(E)\rho_i t} \quad (3.1)$$

where $\mu_i(E)$ is the mass attenuation coefficient of the element i . When the sample composes of many elements, the effective mass attenuation coefficient is given by

$$\mu(E) = \mu_1(E)W_1 + \mu_2(E)W_2 + \dots + \mu_n(E)W_n \quad (3.2)$$

where W_1, W_2, \dots, W_n are the weight fractions of each element in the sample.

When the x-ray beam is incident on the sample at the depth of z as shown in Figure 3.2, the intensity of the transmitted x-rays, $I(E, z)$, can be given by

$$I(E, z) = I_0(E)e^{-\mu(E)\rho\frac{z}{\sin\phi}}. \quad (3.3)$$

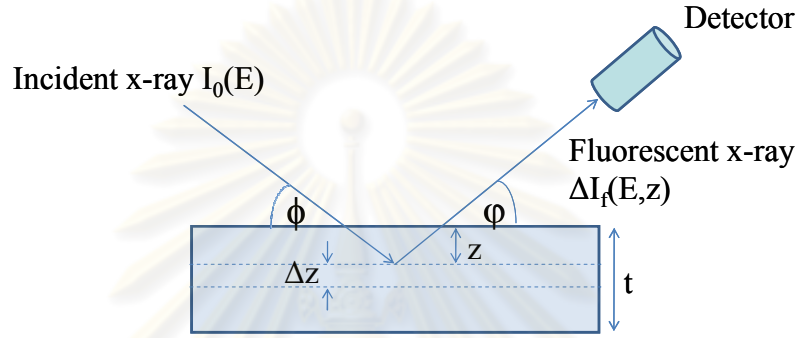


Figure 3.2: Schematic diagram of x-ray fluorescent emission of the sample.

The intensity of primary fluorescent x-rays between the depth of z and $z + \Delta z$ of the sample is given by [30, 31]

$$\Delta I_f(E, z) = P_i \mu_i(E) W_i \rho I(E, z) - I(E, z + \Delta z) = P_i I(E, z) \mu_i(E) W_i \rho^2 \frac{\Delta z}{\sin\phi} \quad (3.4)$$

where P_i is the probability of emitting characteristic x-rays of the element i from the sample. This probability can be calculated from the ionization cross-section and the fluorescent yield [32]. The intensity of primary fluorescent x-rays at the surface of the sample is given by

$$\Delta I_f(E) = \Delta I_f(E, z) e^{-\mu(E_{i,K_\alpha})\rho\frac{z}{\sin\phi}} = P_i I_0(E) \mu_i(E) W_i \rho^2 \frac{\Delta z}{\sin\phi} e^{-\bar{\mu}\rho z} \quad (3.5)$$

where

$$\bar{\mu} = \frac{\mu(E)}{\sin\phi} + \frac{\mu(E_{i,K_\alpha})}{\sin\phi}$$

and E_{i,K_α} is the emitted characteristic x-rays K_α of the element i .

From the definitions of the intensity of emitted primary fluorescent x-rays from everywhere in the sample, the intensity of total primary x-ray fluorescence from

the sample with thickness t can be calculated by

$$I_f(E) = \int_{z=0}^t \Delta I_f(E) dz = P_i I_0(E) \mu_i(E) W_i \rho \frac{1}{\bar{\mu} \sin \phi} [1 - e^{-\bar{\mu} \rho t}]. \quad (3.6)$$

For the intensity of primary fluorescent x-rays, which reaching the solid state detector, the absorption coefficient of the medium between the sample and detector, the geometrical parameters and the efficiency of the detector must be taken into account [31]. The P_i and $\mu_i(E)$ parameters can be determined from the XRF database [33].

When the sample is excited by a white beam, the intensity of primary fluorescent x-rays in K_α -line energy for the element i can be determined by integrating over the energy of equation (3.6)

$$I_{i,K_\alpha} = \int_{E=E_{i,abs}}^{E_{max}} I_0(E) \cdot G_1 G_2 \cdot \tau_{i,K_\alpha} P_{i,K_\alpha} \omega_{i,K_\alpha} B(E, E_{i,K_\alpha}) \cdot \mu_i(E, E_{i,K_\alpha}) W_i \rho \cdot \frac{\varepsilon(E_{i,K_\alpha})}{\bar{\mu}(E, E_{i,K_\alpha}) \sin \phi} [1 - e^{-\bar{\mu}(E, E_{i,K_\alpha}) \rho t}] dE \quad (3.7)$$

where $E_{i,abs}$ = the absorption edge energy

$I_0(E)dE$ = the spectral distribution of the exciting radiation

E_{max} = the maximum energy of a white beam

G_1, G_2 = the geometrical parameters caused by the sample's shape, surface texture, thickness and density

$\bar{\mu}(E, E_{i,K_\alpha}) = \frac{\mu(E_0)}{\sin \phi} + \frac{\mu(E_{i,K_\alpha})}{\sin \phi}$

$\mu_i(E, E_{i,K_\alpha}) =$ the absorption coefficient of the element i

P_{i,K_α} = the probability of the emitted characteristic x-ray K_α of the element i

$\varepsilon(E_{i,K_\alpha}) =$ an efficiency of the detector

ω_{i,K_α} = fluorescent yield of the emitted characteristic x-ray K_α of the element i

τ_{i,K_α} = natural lifetime of the emitted characteristic x-ray K_α of the element i

$B(E, E_{i,K\alpha}) =$ the absorption coefficient of the medium between the sample and detector.

3.1.1 Fluorescent Yield

The fluorescent yield, ω , is defined as a number n of x-ray photons emitted within a given series, divided by the total number N of vacancies in each associated level with the same time increment. Figure 3.3 presents fluorescent yield for x-ray emissions K, L and M shells as a function of atomic number. For the K series, the fluorescent yield, ω_K , can be written as

$$\omega_K = \frac{\sum n_K}{N_K} = \frac{n(K\alpha_1) + n(K\alpha_2) + n(K\beta_1) + n(K\beta_2) \dots}{N_K} \quad (3.8)$$

where n is the number of emitted photon in each subshell of the related shell and N is the number of all emitted photon in the related shell. In addition, the

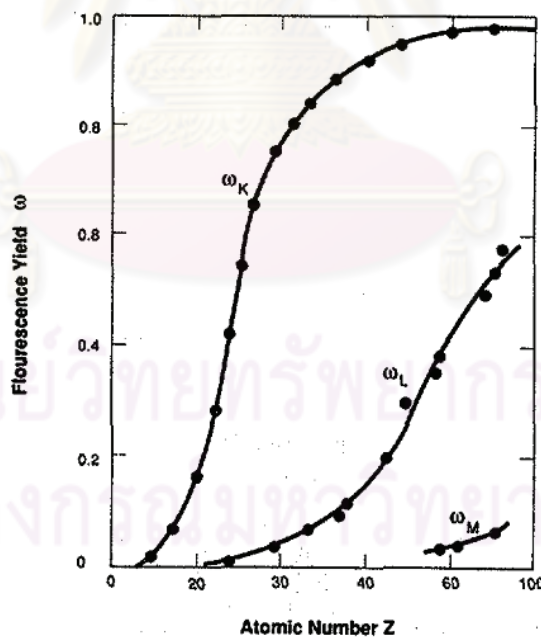


Figure 3.3: Fluorescent yields for x-ray emissions K, L and M shells as a function of atomic number. [32]

production of Auger electrons is other competing reaction, so the ratio of Auger electrons to vacancies is equal to $1 - \omega$.

There are various methods for the determination of fluorescent yields, e.g., using photoionization [34–36], using the measurement of the intensity ratio of K X-rays to incoherently scattered γ -rays [37–39]. In order to test the fluorescent yields for our system, we mix selected oxide compounds including CaCO_3 , TiO_2 , CrO_3 , Fe_2O_3 , NiO , ZnO and CuO by weighting with a ratio of interested elements Ca: Ti: Cr: Fe: Ni: Zn: Cu = 1: 1: 1: 1: 1: 1: 1 gram. Emitted photon counts for the elements are plotted as a function of atomic number as expressed in Figure 3.4. The graph demonstrates that the trends of the relation between photon counts and atomic number are similar to the relation between the fluorescent yields and atomic numbers as shown in Figure 3.3.

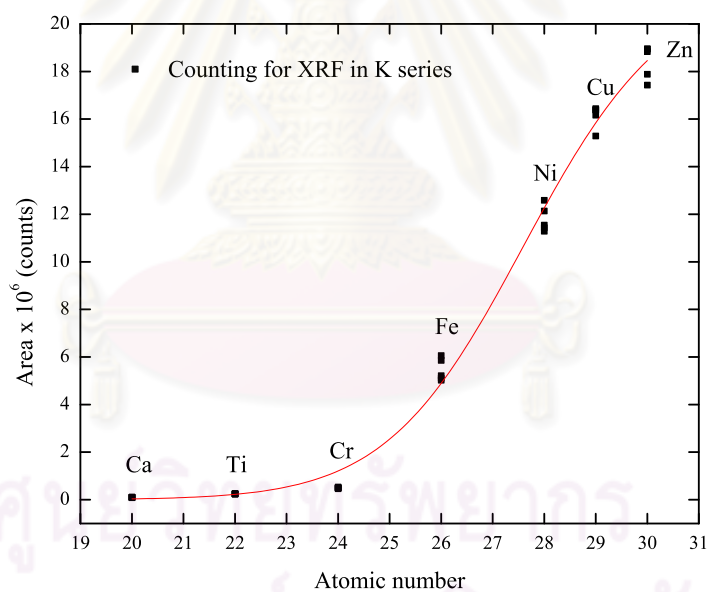


Figure 3.4: Photon counts as a function of atomic number.

3.1.2 White X-Ray Beam Filter

Optical effect of the filter is based on the principle of x-ray absorption. The x-ray absorption curve for the filter is controlled by the material type and its thickness. For primary x-rays, a primary x-ray beam filter is placed between the x-ray tube and the specimen for filtering out the emitted characteristic x-rays K_{α}

and K_{β} lines from the x-ray tube. In addition, in the case of white x-ray beam we utilize this advantage for improving the signal-to-background ratio. Figure 3.5(a) demonstrates the XRF spectra from sticky rice powder for both with and without aluminium filter (aluminium sheet with thickness of 0.1 mm). The setup with the filter can detect more nutrient elements in the rice, i.e., Cr, Ni, Fe, Cu and Zn [40–42]. X-ray transmission for the aluminium filter is expressed in Figure 3.5(b). As results, the comparison between XRF spectra in Figure 3.5(a) indicates that the aluminium filter can improve the detection limit for other nutrient elements in the sample.

In this thesis, we propose to set up an experimental station for XRF techniques at the SPL. A bending magnet source at the SPL can provide a white beam with photon energy up to 12 keV for exciting the sample. We use a Si-PIN detector for detecting fluorescent emissions of characteristic x-rays from the sample.

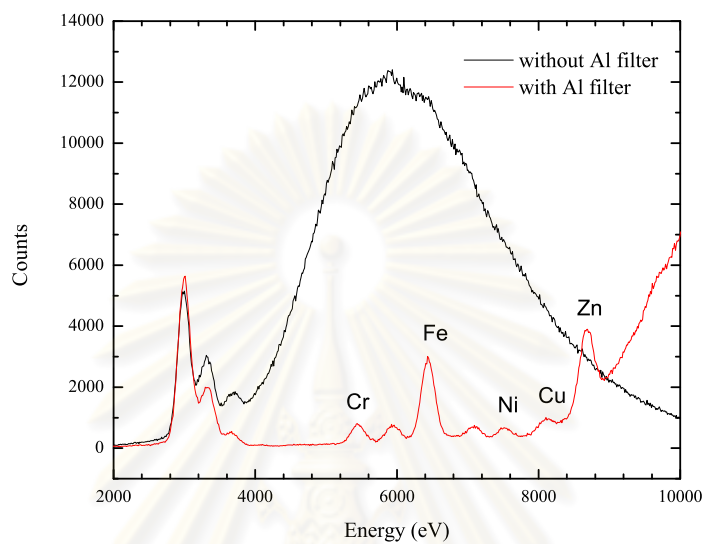
3.2 Si-PIN Detector

Si-PIN detector, a semiconductor detector, is widely used in many application fields; for example, x-ray fluorescence [43], PIXE analysis [44], Nuclear spectroscopy [45] and also works of art investigation [46].

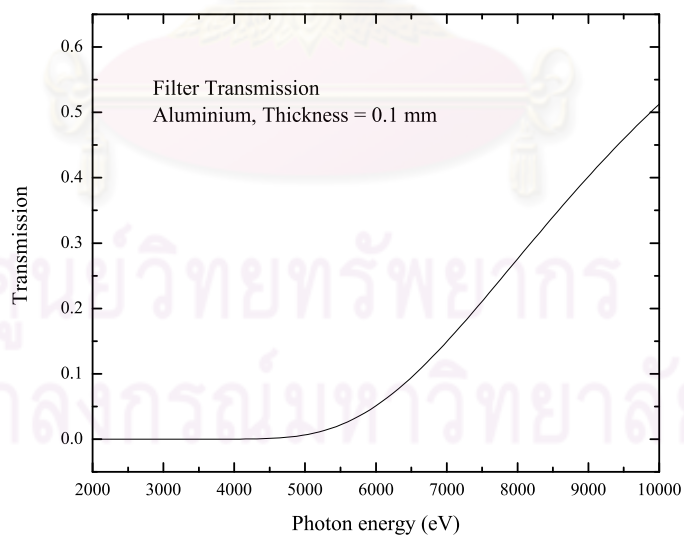
Function of the detector is based on a photodiode. Electron-hole pairs are activated by the detected x-ray photon from the detector. The amount of electron-hole pair (n) correspond with the energy of incident photon (E),

$$n = \frac{E}{\varepsilon}$$

where ε is the average energy for activating a pair of electron-hole. The values of ε are 3.62 and 3.72 eV for silicon at room temperature and 80 K, respectively. After that, the signals from electron-hole pairs are carried by reverse bias electric field to a current pulse for each x-ray entering the detector. The signals are then transformed to voltage pulse using a current-to-voltage pre-amplifier. The amplitude of the voltage pulse is proportional to the original x-ray photon energy. In order to minimize the electronic noise added to the signal during the process,



(a)



(b)

Figure 3.5: (a) XRF spectra from sticky rice powder, (b) x-ray transmission for the aluminium filter with a thickness of 0.1 mm.

the detector is mounted in a light-tight vacuum cryostat and kept at approximately -55°C , and is also monitored by an internal temperature sensor. The detector has a light tight, vacuum tight thin beryllium window for enable soft x-ray detection. The signal from the pre-amplifier is small and has a low signal-to-noise ratio; therefore, the linear amplifier is utilized for amplifying and converting their shape to complete signal-to-noise ratio. Finally, the signal will be arranged to energy spectrum using multi-channel analyser (MCA). The connection for the detection system is shown in Figure 3.6.

In this research, we use a high performance x-ray detector from AmpTek, inc., XR-100CR for recording characteristic x-rays glowed from the samples. The active area of the detector is 6 mm^2 and the energy resolution is about 174 eV at Mn K_{α} . The maximum excitation energy for the white x-ray beam is around 12 keV as detected from the scattered beam. The lightest element detectable by the detector operated in air is sulfur (S) K_{α} (2307.8 eV)

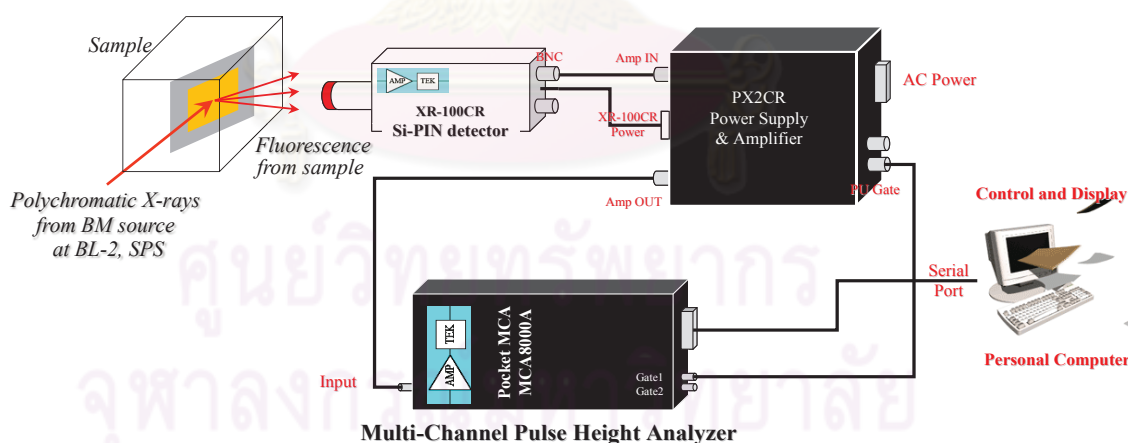


Figure 3.6: Connection diagram for XR-100CR as Si-PIN detector, PX2CR as pre-amplifier and power supply and MCA8000A as multi-channel analyser.

3.2.1 Energy Calibration using Polychromatic X-Rays

The detector was calibrated using metal foil including Ti, V, Cr, Mn, Fe, Co, Ni, Cu and Zn foil and also standard compounds — CaCO_3 and GaAs. The experimental setup for detector calibration is presented in Figure 3.7.

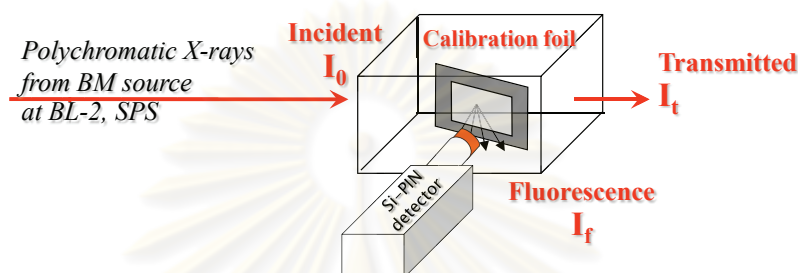


Figure 3.7: Setup for the energy calibration using characteristic x-rays of a metal foil as a calibration foil.

The fluorescent emissions of characteristic x-rays (1 keV and above) from the standard was detected by the Si-PIN detector. Figure 3.8 shows the fluorescent spectra for GaAs in difference magnitude of the MCA and amplifier gain. Suitable magnitude of the MCA is chosen at 5 volts (volt pulse height), ADC gain at 1024 and amplifier gain at 4.0 because this setting position emission K-lines of As, which is the highest elements excitable in K shell. MCA channels are fully employed to detect XRF signal upto highest volt pulse. White beam from bending magnet source can activate characteristic x-rays up to 12 keV.

The reference values of characteristic x-ray energies from calibrated foil are presented in Table 3.1. Table 3.2 presents the comparisons between the observed peak positions from this work and the reference energies.

As results, the calibration equation for the detector with 4.0 amplifier gain and 5 V/1024 channel MCA resolution is

$$Energy(eV) = -65.083 + 12.27 \cdot channel + 0.000171 \cdot channel^2$$

as illustrated in Figure 3.9. Figure 3.10 shows the XRF spectra from the standards in energy scale.

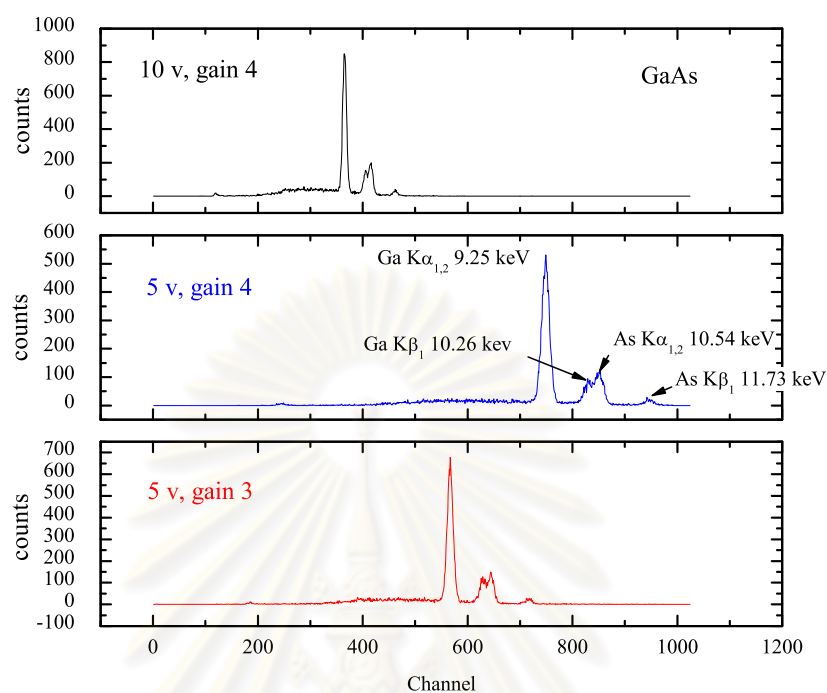


Figure 3.8: GaAs spectra with difference in volt pulse height and amplifier gain.

Table 3.1: Characteristic x-rays of the standard material.

Standard material	Thickness (μm)	$K\alpha_1$ (eV)	$K\alpha_2$ (eV)	$K\beta_1$ (eV)
CaCO ₃ (Ca)	-	3691.68	3688.09	4931.81
Ti foil	6	4510.84	4504.86	4931.81
V foil	5	4952.2	4944.64	5427.29
Cr foil	2 (on Al)	5414.72	5405.51	5946.71
Mn mesh	44*	5898.75	5887.65	6490.45
Fe foil	7.5	6403.84	6390.84	7057.98
Co foil	4	6930.32	6915.3	7649.43
Ni foil	5	7478.15	7460.89	8264.66
Cu foil	7.5	8047.78	8027.83	8905.29
Zn foil	10	8638.86	8615.78	9572.0

*particle size 325 mesh

Table 3.2: Observed peak positions expressed in channel and photon energy that was calibrated using the quadratic equation for Ca, Ti, V, Cr, Mn, Fe, Ni, Cu and Zn. Peak area and the difference between the observed energy and the reference energy are also given.

Standard material	Observed peak position (180 s/ gain 4.0 / resolution 5V, 1024 channel)						Reference Energy (eV)
	Channel	FWHM (channel)	Area (counts)	Energy (eV)	ΔE (eV)	FWHM (eV)	
Ca $K\alpha_{1,2}$	305.125 \pm 0.012	12.931 \pm 0.026	292186.18 \pm 487.13	3693.39	-1.199	159.255 \pm 0.161	3690.48
Ca $K\beta_1$	330.855 \pm 0.047	13.535 \pm 0.100	80763 \pm 497.51	4011.79	3.721	164.765 \pm 0.630	4012.7
Ti $K\alpha_{1,2}$	371.083 \pm 0.008	13.073 \pm 0.016	140527.49 \pm 152.12	4510.05	-1.729	161.402 \pm 0.121	4508.85
Ti $K\beta_1$	404.80 \pm 0.050	13.842 \pm 0.101	24852.79 \pm 156.52	4928.09	4.247	167.789 \pm 0.746	4931.81
V $K\alpha_{1,2}$	406.68 \pm 0.009	13.328 \pm 0.017	217688.10 \pm 243.36	4951.41	0.242	164.57 \pm 0.126	4949.68
V $K\beta_1$	444.68 \pm 0.056	14.147 \pm 0.111	36909.64 \pm 250.72	5423.04	5.256	170.409 \pm 0.813	5427.29
Cr $K\alpha_{1,2}$	443.743 \pm 0.011	13.583 \pm 0.021	235556.15 \pm 319.06	5411.41	-3.167	167.797 \pm 0.145	5411.65
Cr $K\beta_1$	486.403 \pm 0.072	14.633 \pm 0.143	39002.50 \pm 331.16	5941.45	4.471	175.498 \pm 0.98	5946.71
Mn $K\alpha_{1,2}$	482.93 \pm 0.012	13.927 \pm 0.024	413545.06 \pm 622.97	5898.21	-5.021	172.443 \pm 0.202	5895.05
Mn $K\beta_1$	530.176 \pm 0.078	14.982 \pm 0.152	71411.23 \pm 646.14	6485.98	0.051	181.728 \pm 1.306	6490.45
Fe $K\alpha_{1,2}$	523.632 \pm 0.014	14.232 \pm 0.028	475332.28 \pm 804.93	6404.53	-3.222	176.173 \pm 0.295	6399.51
Fe $K\beta_1$	576.097 \pm 0.096	15.214 \pm 0.192	76286.19 \pm 823.24	7057.93	1.745	182.694 \pm 2.03	7057.98
Co $K\alpha_{1,2}$	565.713 \pm 0.016	14.378 \pm 0.031	362892.21 \pm 688.24	6928.53	-3.704	177.864 \pm 0.267	6925.31
Co $K\beta_1$	623.387 \pm 0.113	15.589 \pm 0.226	57126.73 \pm 716.65	7647.68	0.236	184.879 \pm 1.918	7649.43
Ni $K\alpha_{1,2}$	609.635 \pm 0.016	14.615 \pm 0.033	340211.70 \pm 663.36	7476.10	-1.73	181.309 \pm 0.265	7472.40
Ni $K\beta_1$	672.775 \pm 0.118	15.672 \pm 0.236	52783.55 \pm 686.91	8264.42	0.767	188.141 \pm 1.894	8264.66
Cu $K\alpha_{1,2}$	655.040 \pm 0.015	14.902 \pm 0.030	340932.51 \pm 591.01	8042.86	-0.512	184.866 \pm 0.29	8041.13
Cu $K\beta_1$	723.963 \pm 0.106	15.787 \pm 0.212	52385.39 \pm 608.39	8904.52	1.556	188.241 \pm 2.056	8905.29
Zn $K\alpha_{1,2}$	702.153 \pm 0.015	15.104 \pm 0.031	263910.25 \pm 463.46	8631.68	-2.916	187.496 \pm 0.273	8631.17
Zn $K\beta_1$	777.14 \pm 0.110	16.022 \pm 0.219	40285.21 \pm 477.34	9570.44	0.908	190.405 \pm 1.957	9572.00

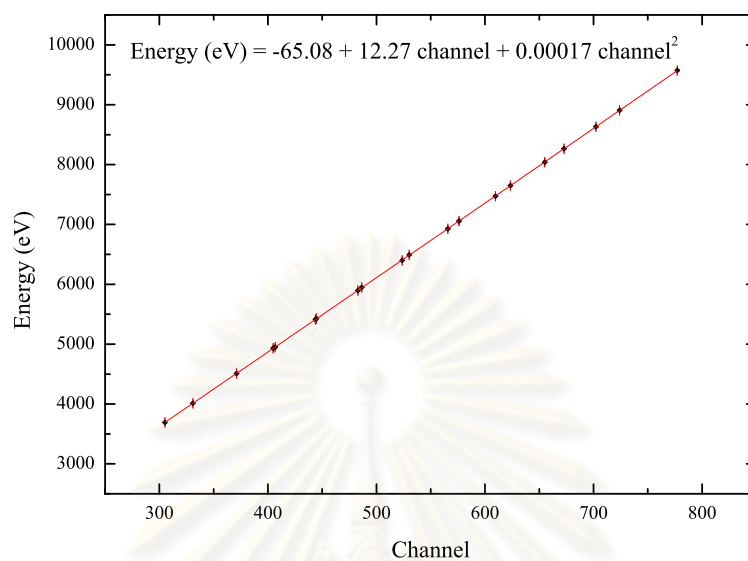


Figure 3.9: Detected pulse height and photon energy is fitted using quadratic equation. Calibration elements are Ca, Ti, V, Cr, Mn, Fe, Ni, Cu and Zn.

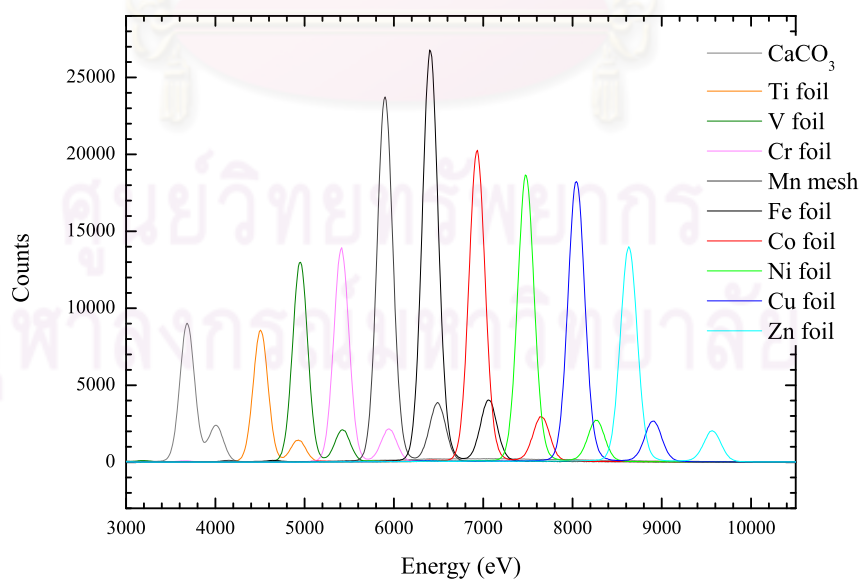


Figure 3.10: Calibrated XRF spectra for standard material with recorded time of 180 s.

3.3 X-Ray Fluorescent Quantitative Analysis

XRF analysis is a well-known technique for elemental identification and quantification as described in chapter 1. For quantitative analysis, suitable calibration methods are utilized for converting recorded XRF data intensities into an elemental concentration. Moreover, either internal or external standards are necessary for calibration process in quantitative analysis. We obtain a standard curve — the XRF intensities versus elemental concentration of standards — by preparing a reasonable number of standards and comparing the intensities of an unknown sample to those of known standards for determining concentrations of detectable elements present in the unknown samples.

For concentration calibration, standards should be prepared in a matrix as having similar composition as possible to the matrix of the sample. Dilute nitric acid (HNO_3) is usually used as a solvent for dissolving appropriate amount of chemical standards [47–51]. Furthermore, we can directly blend chemical standards to the matrix similar to sample matrix in a reasonable ratio; for example, in the case of powder form. The correlation between the fluorescent intensity and the elemental concentration is expressed by [52–54],

$$I_i = S_i \cdot C_i \quad (3.9)$$

where I_i is the fluorescent intensity of element i (cps), S_i is the sensitivity for element i (cps/ppm) and C_i is the concentration of element i (ppm). The sensitivity depends on instrumental factors and on fundamental physical parameters related to the energies of the incident and characteristic x-rays; for instance, the geometry of the XRF spectrometer, the detector efficiency for radiation of photon energy E_i and also the fluorescent yield of element i . For this method, we can add many internal standards for obtaining the calibration curve, e.g., K, Ca, Ti, Mn, Fe and Ga. In order to obtain the calibration curve — relation between the sensitivity and atomic number, $S'_i = f(z_i)$ — for each experiment, the intensity for internal

standard (SD), I_{SD} , can be written as

$$I_{SD} = S_{SD} \cdot C_{SD} \quad (3.10)$$

where S_{SD} is the sensitivity for internal standard (cps/ppm) and C_{SD} is the concentration of internal standard (ppm). We divide equation (3.9) by equation (3.10),

$$\begin{aligned} \frac{I_i}{I_{SD}} &= S' \cdot \frac{C_i}{C_{SD}} \\ R_i &= S'_i \cdot C_i \end{aligned} \quad (3.11)$$

where the relative sensitivity $S' = \frac{S_i}{S_{SD}}$ and product of the ratio of intensity for element i to intensity for internal standard (SD). In theory, the relative sensitivity for internal standard (S'_{SD}) is equal to one. The concentration of internal standard is

$$R_i = \frac{I_i}{I_{SD}} \cdot C_{SD}.$$

We could select internal standard from the absent element in the sample. To get S'_i , we mixed a set of external i with C_i and internal standard with C_{SD} and then measured the intensity I_i and I_{SD} ,

$$S'(z_i) = \frac{I_i}{I_{SD}} \cdot \frac{C_{SD}}{C_i} = f(z_i).$$

According to the graph between $S'(z)$ vs. z , we can obtain the calibration curve in order to determine the sensitivity for element i in the sample for each experimental set.

3.4 XRF Analysis Software

XRF analysis software was coded in C language based on Mathematica. The GUI interface was developed using MATLAB. At first the XRF data was fitted using Gaussian fit. After obtaining center for each peak with energy E, these values were compared with the database of XRF emission lines [33]. The algorithm, based on finding minimum value for the difference between E and $E_{theory:K,L,M}$ (ΔE_{min}), for peak indexing is described in Figure 3.11.

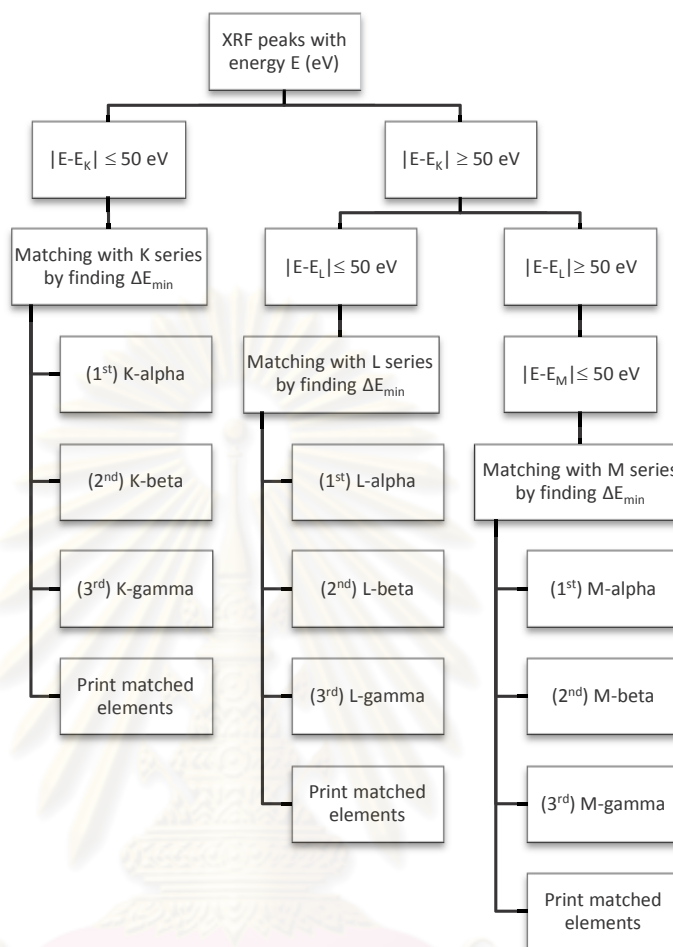


Figure 3.11: Algorithm for XRF analysis software

3.5 X-Ray Fluorescent Imaging

XRF imaging or mapping is very useful XRF technique for analysing the two-dimensional distribution of elements across an irradiated area, within x-ray penetration depth of the sample. The XRF mapping is typically presented by color levels corresponding to elemental's concentration. The referred literatures for this techniques, among many others, are the determination of elements in a fossil snail on the coast of the Baltic Sea on the island Ruegen [55], the investigation of the distribution of elements in snail shell with the use of synchrotron-based, micro-beam X-ray fluorescence spectrometry [56] and elemental distribution mapping on breast tissue samples [57]. This technique requires a small focal spot of an x-ray

beam for probing on a sample. In addition, a reasonable time for determining the 2D XRF information from a sample will be considered; therefore, a white x-ray beam from synchrotron x-ray source is desired as a microprobe of high spatial resolution (about 10-100 μm) because of its high flux and small divergence. In this research, we use a polycapillary x-ray half lens for focusing a white x-ray beam.

3.5.1 Polycapillary X-Ray Optics

A polycapillary x-ray optics is extensively used for focusing synchrotron radiation in micro x-ray analysis; for example, x-ray fluorescent imaging, micro x-ray absorption fine structure analysis and others. A polycapillary x-ray lens comprises an array of large numbers of small hollow glass tubes bent to a certain shape. This optic collects emerging x-rays from an x-ray source within a large solid angle and redirects them, by multiple external total reflections, to form either a focused beam (full lens) or a parallel beams (half lens) as illustrated in Figure 3.12. The critical angle for total reflection on glass surfaces is

$$\theta_c[mrad] = \frac{30}{E[keV]}$$

for photon energy ranging of 5-30 keV. The capillary lens can work as focusing and collimating as illustrated in Figure 3.13 [26]. For an x-ray source having very small source size and being quasi-parallel, i.e., synchrotron radiation, the capillary lens can work quite well for focusing the beam. On the other hand, the lens can be used as a collimator for a small diverging x-ray beam.

In this research, we used the polycapillary half lens (No.UNS1G-1F-171208) manufactured by UNISANTIS EUROPE GmbH to obtain a white micro beam for XRF imaging technique. The specifications of the capillary are listed in Table 3.3. The test results for the capillary lens will be presented in chapter 6.

Table 3.3: Specifications of the Polycapillary half lens No.UNS1G-1F-171208

Polycapillary half lens No.UNS1G-1F-171208	Specifications
Unit length (mm)	38.0
Unit diameter (mm)	14.5
Outlet focal distance (mm)	22.5
Optical inlet diameter (mm)	9.5
Transmission for Cu line (8.04 keV) (%)	12
Focal spot size for Cu line (μm)	95

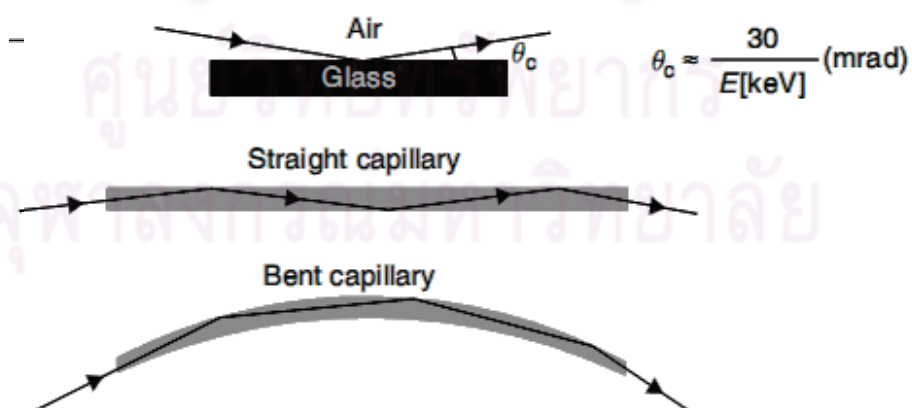


Figure 3.12: Schematic representation of the principles of capillary optics. [26]

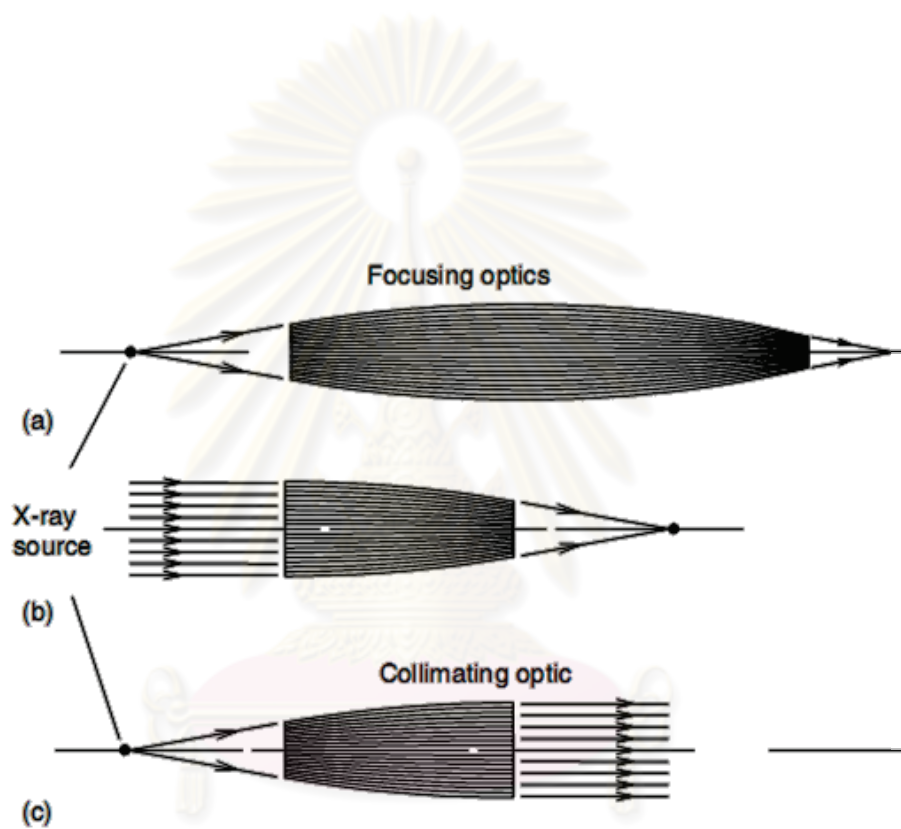


Figure 3.13: Polycapillary x-ray optics; (a) focusing lens, (b) half focusing lens and (c) parallel beam lens. [26]

จุฬาลงกรณ์มหาวิทยาลัย

3.6 The Lower Limit of Detection

In XRF analytical system, an important assessment, which depends on statistics of the x-ray emission, is the capability of the system to detect XRF signal from an element in a sample. If concentration of an interested element is greater than the limit of detection (LLD), we can observe its XRF signal.

To understand the LLD concept, we consider a sample having an element that emits XRF signal. If the concentration of this element in the sample is C , the system will detect I_{net} , which is the XRF intensity or countly rate subtracted by I_b of the background intensity. Had the detection system no statistical at all, the lowest concentration to be detected as one photon counts would be $\frac{C}{I_{net}}$. However, it is known that the probability of photon emission follows Gaussian statistics, thus the minimum photon counts that will be considered as the XRF signal, not the background, must higher than two times of the standard deviation of the background, $2\sigma_{I_b}$. It is the justified to define LLD, or the lowest detectable concentration, as

$$LLD = 2\sigma_{I_b} \frac{C}{I_{net}} = 2 \frac{C}{I_{net}} \sqrt{\frac{I_b}{T_b}} \quad (3.12)$$

where $\sigma_{I_b} = \frac{\sqrt{N_b}}{T_b} = \sqrt{\frac{I_b}{T_b}}$ for Gaussian statistical error. Here T_b is the accumulation time for background counting, which can be deducted from the total intensity, I_p , and the total time of the measurement, T_p as

$$\frac{T_p}{I_b} = \sqrt{\frac{I_p}{I_b}} \quad (3.13)$$

It should be noted that LLD for the same element at the same concentration usually differs from one sample to another. This is mainly due to the radiation of absorption coefficients (see equation (3.3 - 3.7)) in different matrix.

In the case of low concentration sample, errors is increasing by the factor of $\sqrt{2}$, so the LLD can be expressed as,

$$LLD = \frac{2\sqrt{2} \cdot C}{I_{net}} \cdot \sqrt{\frac{I_b}{T_b}} \quad (3.14)$$

Table 3.4 presents the detection limit of selected elements in different matrix evaluated for our XRF system used in this work.

Table 3.4: Detection limit for selected elements in different matrix.

Atomic Number	Element	Matrix	LLD (ppm)	I_{net} (cps)	C_i (%)
16	S	Gasoline	425	20	1.44
20	Ca	Anlene gold (low fat milk powder)	8	2270	1.16
22	Ti	Blush on	200	215	8.2
25	Mn	Blackmores Bio Zinc	118	55	0.4
26	Fe	Ginseng root	60	965	6.76
		Blush on	125	1134	11.0
28	Ni	Zeolite beta	38	2757	1.0
		Lipstick	8	693	0.3
29	Cu	0.1%CuO-doped glass	4	450	0.08
30	Zn	Blackmores Bio ACE	13	2610	1.0
		Corn leaf	4	160	0.13
		Wood	163	734	1.44

ศูนย์วิทยทรัพยากร
จุฬาลงกรณ์มหาวิทยาลัย

CHAPTER IV

X-RAY POWDER DIFFRACTION TECHNIQUE

X-ray powder diffraction is one of the most basic techniques for structural analysis of materials in the form of loose powders. A powder is composed of many crystallites with random orientation. In Figure 4.1, the scattered x-rays are completely in phase and their path differences are equal to n times the wavelength, therefore the diffraction occurs satisfying the Bragg's condition:

$$n\lambda = 2d_{hkl} \sin \theta \quad (4.1)$$

where n is a positive integer corresponding to the order of diffraction. For a first-order diffraction ($n = 1$) in Figure 4.1, the scattered rays 1' and 2' are in phase and their path length differ by a wavelength. The angle between the diffracted beam and the transmitted beam is always 2θ , called the diffraction angle or the Bragg angle. The intensity of the diffracted beam depends on the arrangement of atoms on the planes. The diffracted beam is rather strong when all rays scatter in the same direction.

Powder diffraction pattern can be recorded using a detector-photographic film, charge-coupled device (CCD), image plate, position-sensitive photodiode (PSD), etc. Whether the analogue or digital data collection technique is used, the final data can be displayed as intensity profiles versus d -spacing or Bragg angle.

4.1 Image Plate Area Detector

Originally the x-ray diffraction pattern was recorded on a photographic film by an x-ray camera. The camera was designed to hold a powder specimen and a photographic film for recording the diffracted beams. However, most of photographic films are sensitive to visible light. Hence, a solid state area detector, called image plate, has been developed.

Image plate area detector is a reusable two-dimensional detector used for

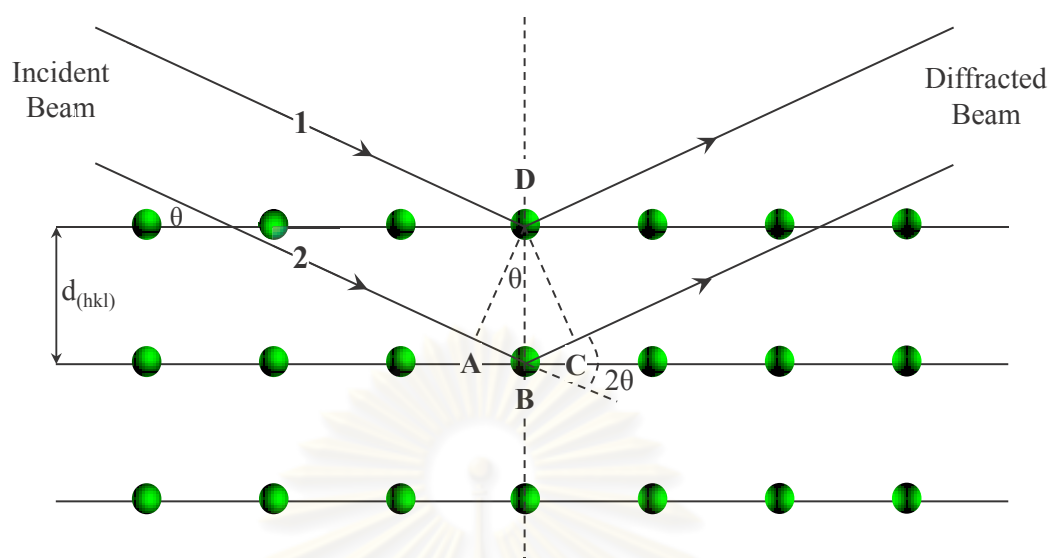


Figure 4.1: Bragg's Law

recording two-dimensional diffraction patterns. The surface of the detector could be spherical, cylindrical or flat depending on setup geometry between a sample and the detector. Both spherical and cylindrical area detectors are designed for a fixed sample-to-detector distance. The flat area detector has great flexibility to be used at different sample-to-detector distances. Image plate area detector was originally developed for the medical radiology. The detector has become very popular in high-pressure angle dispersive powder diffraction technique because it is highly sensitive for the short-wavelength x-rays ($\lambda < 0.7 \text{ \AA}$) passing through a pressure cell. In this research, the image plate used is made of the phosphor material BaFBr:Eu²⁺ bonded on the backing plate of 20×25 cm² flat aluminium and covered with a thin layer of transparent plastic. The family of BaFX:Eu²⁺ (X = Cl, Br) compounds has been known to have the high luminescence efficiency for x-ray excitation for over thirty years [58]. The excited electron state will occur when the x-ray photons are absorbed by phosphor screen. In order to irradiate the screen, He-Ne laser with $\lambda = 632 \text{ nm}$ has been used for generating photo-stimulated luminescences in visible light photons at $\lambda = 400 \text{ nm}$. The intensity of visible light photon is proportional to those of original x-ray photons absorbed by the phosphor screen. The x-ray powder diffraction apparatus for high-pressure

research is illustrated in Figure 4.2.

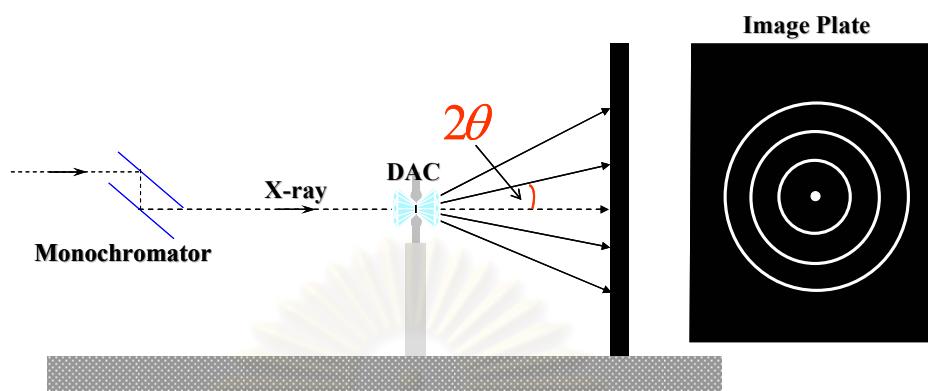


Figure 4.2: Schematic diagram of image plate method in high-pressure research. [59]

4.2 Crystal Structure Refinement

The reflection peak intensities versus Bragg angle from the integrated one-dimensional powder diffraction pattern were fitted using Pseudo-Voigt function for unit cell determination. Automatic indexing program such as DICVOL [60], UNIT CELL [61] and CRYTALCRACKER [62] were used in order to obtain lattice parameters by minimizing residuals in the experimentally determined Bragg position in the terms of $2\theta_{hkl}$, d-spacing (d_{hkl}) or energy (E_{hkl}) using a non-linear least squares method. The Rietveld method is used for refining the crystal structure.

The Rietveld method was first presented by H. M. Rietveld in 1969 [63]. Since diffraction peak intensity depends on the atomic type and atomic distribution within the unit cell, the lattice parameters of structure models, intensities of Bragg peaks and also instrument effects on the diffraction pattern, All these quantities are refined.

The shape of reflection profiles can be affected by many factors including temperature, polarization, absorption, particle size and also preferred orientation. Least-square refinement is used for adjusting parameters of the model and comparing the calculated diffraction profile with the observed step profile point by

point. This method calculates intensities of the reflection peaks in an experimental pattern and combining various controllable factors in the form of a diffraction diagram. Moreover, the model is adjusted to obtain the best fitting and accurate information of atomic positions in a unit cell. The usual refinable parameters are listed in Table 4.1 [64]. The calculated model can be used to describe several information from a sample such as lattice parameters, symmetry of a unit cell, atomic coordinates, thermal parameters, occupancy, optics, set-up of diffractometer and peak shape, etc. Each variable will be refined until a diffraction pattern from observing and from calculating diagram are matched.

The quantity minimized in least-squares refinement is the residual, χ^2 ,

$$\chi^2 = \sum_i w_i (y_{oi} - y_{ci})^2 \quad (4.2)$$

where w_i = the statistical weight at the i^{th} step, $\frac{1}{y_{oi}}$,

y_{oi} = the observed intensity at the i^{th} step,

y_{ci} = the calculated intensity at the i^{th} step,

with summation runs overall data points. The calculated intensity is a combination of many factors following the equation:

$$y_{ci} = s \sum_K L_K |F_K|^2 \varphi(2\theta_i - 2\theta_K) P_K A + y_{bi} \quad (4.3)$$

where s = the scale factor,

K = the Miller indices, $h k l$, for a given Bragg reflection,

L_K = the Lorentz factor,

φ = the reflection profile function,

P_K = the preferred orientation function,

A = an absorption factor,

F_K = the structure factor for the K^{th} Bragg reflection,

y_{bi} = the background intensity at i^{th} point, can be modelled or subtracted,

base on physical reality.

Table 4.1: Parameters refinable simultaneously

For <i>each</i> phase present
x_j y_j z_j B_j N_j (x_j , y_j , and z_j are position coordinates, B_j is an isothermal parameter, and N_j is the site-occupancy multiplier, all for the j^{th} atom in the unit cell.) Scale factor Lattice parameters Thermal parameter Preferred orientation Crystallite size and microstrain
Global
2θ -Zero Instrumental profile Profile asymmetry Background Wavelength Specimen displacement Specimen transparency Absorption

The reflection profile function estimates the effects of instrument and specimen features, i.e., aberrations due to transparency, specimen displacement and specimen-caused broadening [64]. The structural parameters and unit cell parameters ($a, b, c; \alpha, \beta, \gamma$) are ignored in equation (4.3). The structure factor, $|F_K|$, depends on the positions of every atoms within each Miller plane and can be written as,

$$F_{hkl} = \sum_j N_j f_j \exp [2\pi i(hx_j + ky_j + lz_j)] \exp (-B \sin^2 \frac{\theta}{\lambda^2}) \quad (4.4)$$

where N_j = the site occupancy,
 f_j = the structural factor for j^{th} atom,
 x_j, y_j, z_j = the position parameters of j^{th} atom in the unit cell,
 B = the thermal vibration.

The peak shape in the powder diffraction can be described using the Pseudo - Voigt function with the refinable degree of mixing following the equation:

$$pV = \eta L + (1 - \eta)G \quad (4.5)$$

where pV = the pseudo - Voigt function,

L = the Lorentzian function:

$$f(x) = y_0 + \frac{2A}{\pi} \frac{w}{4(x - x_c)^2 + w^2},$$

G = the Gaussian function:

$$f(x) = y_0 + \frac{A}{w\sqrt{\frac{\pi}{2}}} e^{-\frac{2(x-x_c)^2}{w^2}},$$

η = the mixing parameter.

The peak shape of the Pseudo - Voigt function are compared with those of the Lorentzian and Gaussian functions in Figure 4.3. The mixing parameter can be refined as a linear function of 2θ . The refinable variables — NA and NB — can be written as,

$$\eta = NA + NB * (2\theta). \quad (4.6)$$

and

$$NB * (2\theta)_i = \sum_{j=-n}^n NB_{i-j}(2\theta)_j \quad (4.7)$$

where $*$ is the convolution operator. Moreover, the peak shape also depends on the half-width of Bragg peaks or full width at half maximum (FWHM). The FWHM shows an angular dependence that can be expressed by the Caglioti function,

$$H^2 = U \tan^2 \theta + V \tan^2 \theta + W \quad (4.8)$$

where H = the half-width of Bragg peaks (FWHM),

U, V, W = the refinable parameters.

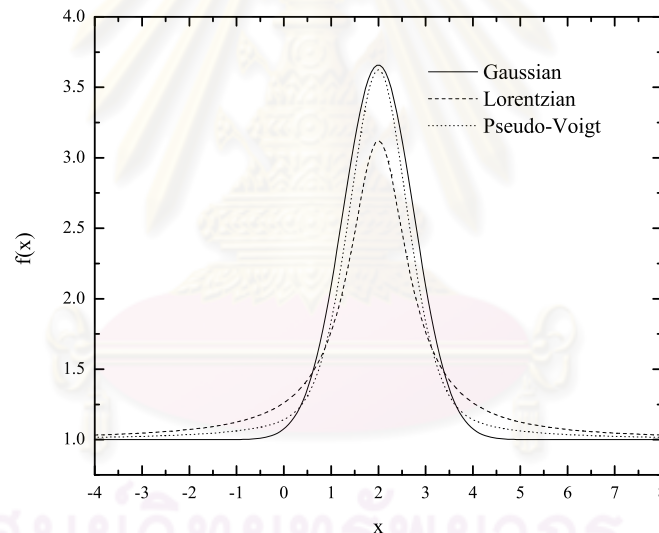


Figure 4.3: Gaussian function (solid line), the Lorentzian function (long dash line) and the pseudo - Voigt function (short dash line) for $y_0 = 1$, $x_c = 2$, $A = 5$ and $w = 1.5$.

After compressing small amount of powder sample in a pressure cell, crystal-lites in the sample may be oriented in one direction more than all others which is called preferred orientation effect. For powder diffraction experiments, preferred orientation, a frequent problem, can produce systematic distortions of the reflection intensities. These distortions can be modelled mathematically in the form of

the preferred orientation function (P_K),

$$P_K = \exp(-G_1\alpha_K^2) \quad (4.9)$$

or

$$P_K = G_2 + (1 - G_2) \exp(-G_1\alpha_K^2) \quad (4.10)$$

where G_1 , G_2 are refinable parameters. In addition, P_K is used for small preferred orientation.

In 1989, Ahtee *et al.* [65] presented a spherical harmonic formulation for defining an orientation distribution function as a function of the sample and the Laue phase symmetry. In this research, we use the aid of Generalized Structure Analysis System (GSAS) program [66, 67], which is based on the described method and least-square refinement, for crystal structure refinement. The GSAS has been developed by Allen C. Larson and Robert B. Von Dreele at Los Alamos National Laboratory, USA. This program is widely used for fitting crystallographic and magnetic structural models to x-ray and neutron single-crystal and powder diffraction data for both time of flight and monochromatic neutron powder diffraction.

ศูนย์วิทยทรัพยากร
จุฬาลงกรณ์มหาวิทยาลัย

CHAPTER V

EXPERIMENTAL METHODS

5.1 X-Ray Fluorescent Analysis

Figure 5.1 shows the experimental setup for XRF analysis temporarily installed on the beamline BL2 at the Siam Photon Laboratory using synchrotron radiation in the x-ray region from the bending magnet. Sample holder is set to 45 degrees with respect to the incident beam and the detector. The distances between sample to slits and to detector are 10 and 16.4 cm, respectively. For XRF analysis on millimeter-sized samples, we set the unfocused beam size using horizontal slit to match the sample size in order to increase detection sensitivity. All measurements were carried out in air; moreover, aluminium sheets with thickness of 0.1 mm are used as the filter for improving the signal-to-background ratio and protecting the detector from radiation saturation damage caused by high intensity of the scattered white beam. Because electron-beam current in the storage ring decreased with time and so does the intensity of synchrotron radiation, this affects XRF signal as it is directly proportional to the incident x-ray intensity. In order to correct this problem, one can normalize the XRF spectra using 1) peak area of internal standard added to each sample, 2) beam current during the measurement or 3) intensity of x-ray incident beam, I_0 , that can be measured from an ionization chamber.

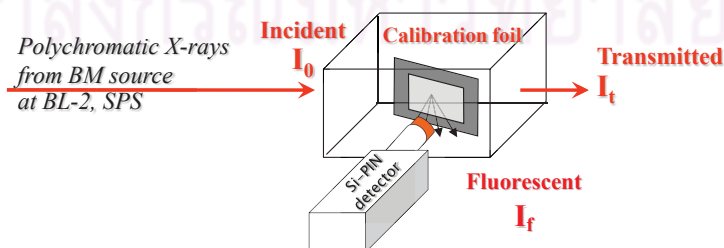


Figure 5.1: Schematic diagram of the experimental setup for XRF analysis.

Sample Preparation

Using XRF quantitative analysis, we have selected to study contamination in food as an example. The objects include sticky rice for polluted and corn leaf which were grown in soil containing high amount of cadmium (Cd). For corn leaf, we prepared dry sample in a kapton frame. For the sticky rice, we prepared powdered sample in the kapton frame. The sample size in the kapton frame for both rice powder and corn leaf was $2 \times 0.5 \text{ cm}^2$.

For determining the lower limit of detection (LLD) for this system, many interesting samples from laboratories and common goods including herb, catalyst, food, cosmetics and also fuels were analysed. The LLD are listed in Table 3.4 for these samples. The unfocused beam size was controlled to match the smallest sample size because we need the same beam size for all experiments.

Standard Preparation

For determining amount of Cd in sticky rice powder, we prepared a calibration set by mixing a controlled sticky rice powder (without Cd) with CdO (purity 99.99%) at 1, 2, 3, 4 and 5% w/w of Cd. For corn leaf, standard solutions were prepared by dissolving appropriate amount of CdO 99.99% in 5% (v/v) of HNO₃ at 1, 2, 3, 4 and 5% of Cd.

XRF Qualitative Analysis and Software

XRF analysis on a NIST SRM 610 trace-elements standard reference material in a glass matrix (S610) was conducted for testing the experimental setup and XRF analysis software written in Mathematica. The nominal composition of the glass matrix is 72% SiO₂, 12% CaO, 14% Na₂O and 2% Al₂O₃. There are 61 trace elements in S610 [68]. The recorded XRF spectrum from S610 with a counting time of 2000 s is shown in Figure 5.2. Our system could detect up to 10 elements in S610 (Ca, Mn, Fe, Cr, V, Co, Ti, Ni, Cu and Zn). Since the highest excitation photon energy is around 12 keV, the other heavier elements in S610 cannot be excited. Besides, some of them have very low concentrations beyond the lower

limit of detection (LLD) for our system. Currently, XRF analysis software is implemented for automatically assigning the observable peaks to the characteristic x-ray emission of elements from $z = 1$ to 95 in the periodic table [33]. The peak fitting is based on a Gaussian function. The peak fitting from the XRF analysis software will be presented in the next chapter.

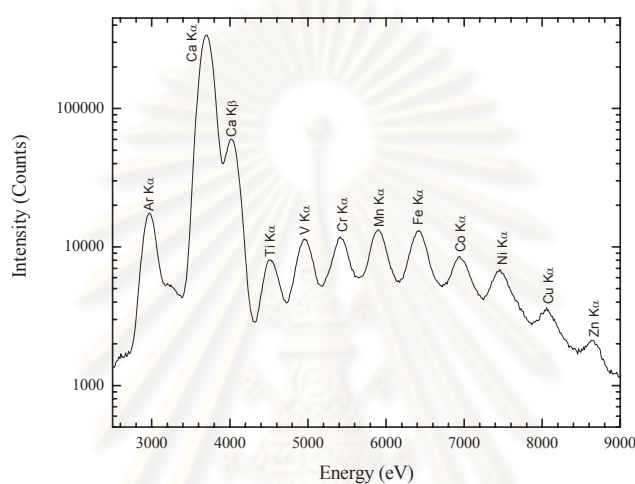


Figure 5.2: Experimental XRF spectrum from a NIST SRM 610 standard with a white beam and measurement time 2000 s.

ศูนย์วิทยทรัพยากร
จุฬาลงกรณ์มหาวิทยาลัย

5.2 X-Ray Fluorescent Imaging

Figure 5.3 shows two different apparatus for XRF imaging installed at the beamline BL2. The scanning x-axis for both models follow the motor axis, which are rotated by 45 degrees with respect to the sample surface for the setup No.1 but are set parallel to the sample surface for the setup No.2. So the dimension of the recorded XRF image will be smaller than that of the sample for the setup No.1. A two-dimensional motorized translation stage is used for moving a particular position on the sample to intercept the beam. The white x-ray beam of $7 \times 1 \text{ mm}^2$ defined by a horizontal slit was focused using a polycapillary x-ray half-lens as described in chapter 3. In order to measure the focused white x-ray beam size, we scanned titanium (Ti) and copper (Cu) wire across the beam and counted emitted photons at Ti K_α (4510.8 eV) and Cu K_α (8047.7 eV) with the silicon PIN detector. We measure the focused x-ray beam size for both white beam and monochromatic beam. The wire is placed at the sample position where the beam is focused. To obtain the focused beam size, the apparent widths were deconvoluted with the width of the wire. In order to recorded the fluorescent data for each scanning point, the author have partly developed the program for controlling the scanned motor by defining the scanned boundary, step size, step time and also ROI for the XRF spectra. For each sample scanned, we need to scan the wire for testing the spatial distribution of focused beam. For good focused beam, the beam profile will be Gaussian.

At first, the apparatus for the technique was the setup No.1 as illustrated in Figure 5.3(a). However, problems regarding the dimension miss match between the fluorescent image and the visual image were identified and the apparatus has been changed to the setup No.2 as shown in Figure 5.3(b). For both apparatus, the gap between the horizontal slit and the capillary lens is 7 cm. In addition, the gap between the capillary lens and sample is 2.5 cm. Moreover, the gap between sample and the detector is 5 cm. The different results for both apparatus models will be compared in chapter 6.

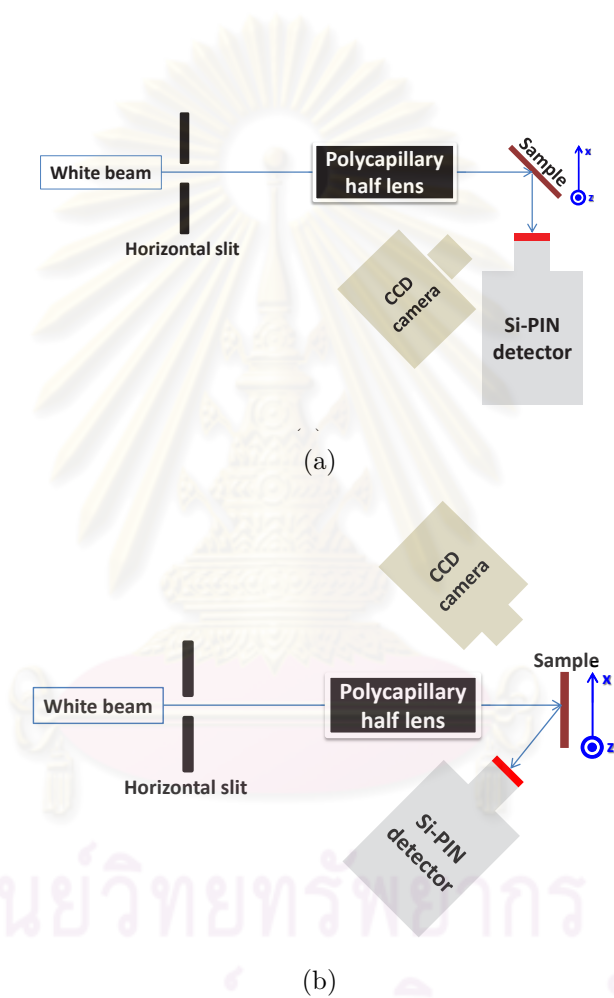


Figure 5.3: Schematic diagram of the experimental setup for XRF imaging at the Siam Photon Laboratory;(a) the setup No.1 and (b) the setup No.2.

One Dimensional XRF Imaging System

We used nickel grids of different sizes coated on supporting glass as shown in Figure 5.4 for testing the accuracy of the XRF imaging experiment firstly in one direction (horizontal). The relevant dimensions of the nickel grid structure denoted by the capital letters in Figure 5.4(b) is given in Table 5.1. Characteristic x-rays of Ni K_{α} from patterns 1, 2, 3 and 4 were recorded using the Si-PIN detector where the horizontal scanning step (Δx) was 20 μm and the counting time was 30 second for each step. The tested results will be described in the next chapter.

Table 5.1: Widths (A, B) and spacing (C) of the nickel grid structure denoted in Figure 5.4(b).

Nickel grid No. Pattern	Width (mm)		
	A	B	C
1	0.085	0.110	0.395
2	0.155	0.190	0.410
3	0.010	0.050	0.350
4	0.150	0.195	1.000

Two Dimensional XRF Imaging System

For testing the two dimensional XRF imaging system, we used a hand-made pattern of cobalt foil (7.5 μm -thick) overlaid on copper foil (4 μm -thick) as shown in Figure 5.5. The step size for scanning was 150 μm , the counting time was 10 s/step and the scanned area was 6000 $\mu\text{m} \times 6000 \mu\text{m}$.

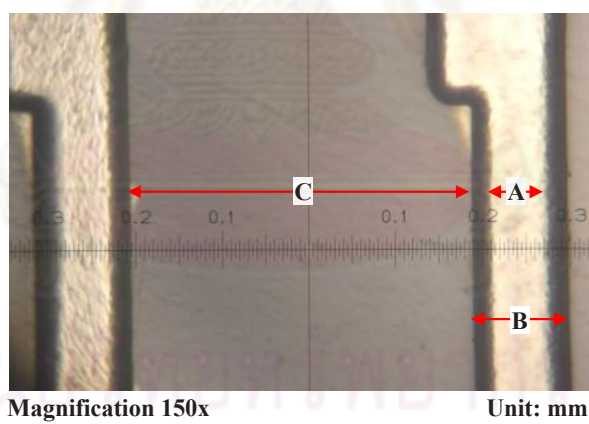
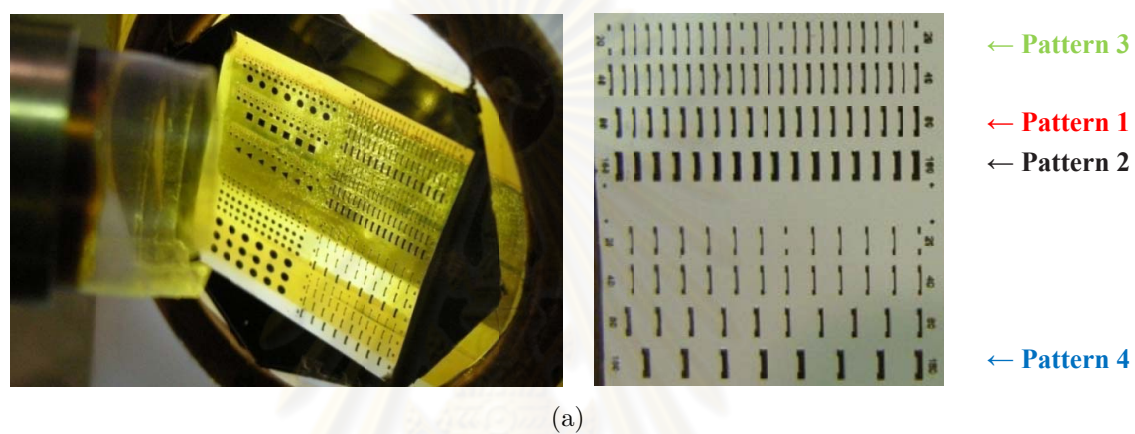


Figure 5.4: Patterns 1-4 and magnified structures of nickel grids on supporting glass.

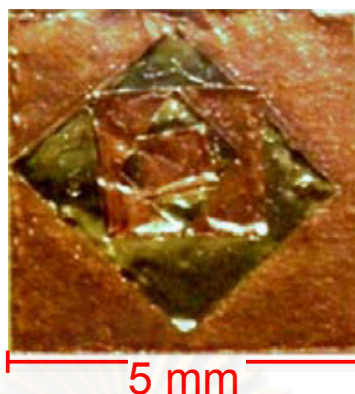


Figure 5.5: Photograph of the test object made of copper (seen in orange) and cobalt (gray) foils.

Scanning Position Calibration

It can be seen that a careful calibration of the scanning position is very important for accurate mapping the fluorescent image with the visual image of the sample. This is one of the remaining tasks to be carried out to complete our XRF imaging technique.

Figure 5.6 shows the steps for experimental setup of XRF imaging. Firstly, we define a scanned area and starting point for scanning using a sample holder with a fluorescent screen and a grid pattern ($1 \text{ pixel} = 1 \text{ mm}^2$), the picture is captured using a CCD camera. The grid pattern is made from black ink printed on a transparent plastic for printer. The sample holder also has the grid pattern as the sample holder. We put a sample on the defined scanning area and capture the picture. After complete the procedure, the scan starts.

According to previous procedure, we found that we cannot specify the exact position on the scanned fluorescent, because the grid pattern is not uniform. For adjusting the calibration method, nickel mesh with $\phi 43 \mu\text{m}$ and spacing $803 \mu\text{m}$ is used as grid reference. The nickel mesh is put over a fluorescent screen as presented in Figure 5.7 for calibrating picture frame and motor frame.

The procedures for calibrating picture frame and motor frame using the nickel mesh are:

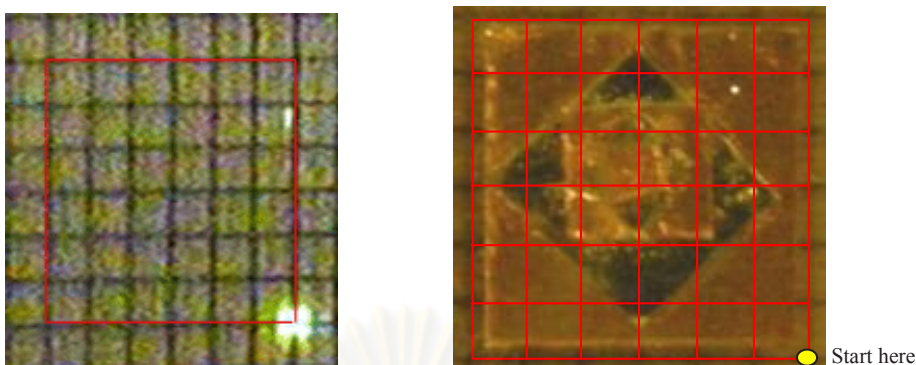


Figure 5.6: Defining scanned area (left). Sample was placed in the scanned area (right).

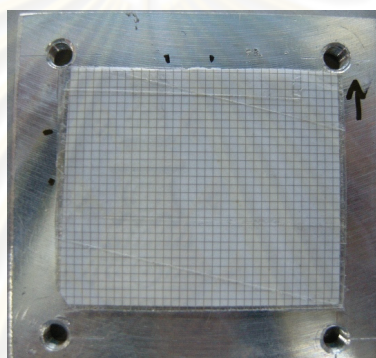


Figure 5.7: Sample holder with Ni mesh over a fluorescent screen.

1. First, moving white beam to the starting position.
2. Finding center of the beam (X_{c1} and Y_{c1}) by scanning Ni mesh along x and y directions.
3. Moving the starting point by X_{c1} and Y_{c1} to coincide with the center of the beam.
4. Moving sample holder from X_{c1} to $X_{c1}+5$ mm (X_{c2}) and scanning Ni mesh again for finding Y_{c2} as shown in Figure 5.10. For this setup, $Y_{c2} - Y_{c1} = 0.05$ mm and $\theta = 0.543$ degrees (0.01 radian).
5. If $Y_{c1} = Y_{c2}$, the motor frame is equivalent to the picture frame. If $Y_{c1} \neq Y_{c2}$, we have to rotate the picture by using (X_{c1}, Y_{c1}) as a pivot for mapping both frames.

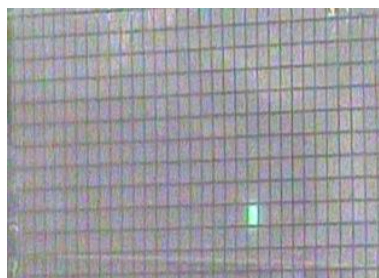


Figure 5.8: Capture photo for Ni mesh by CCD camera. A green spot represents the position of x-ray beam on the screen.

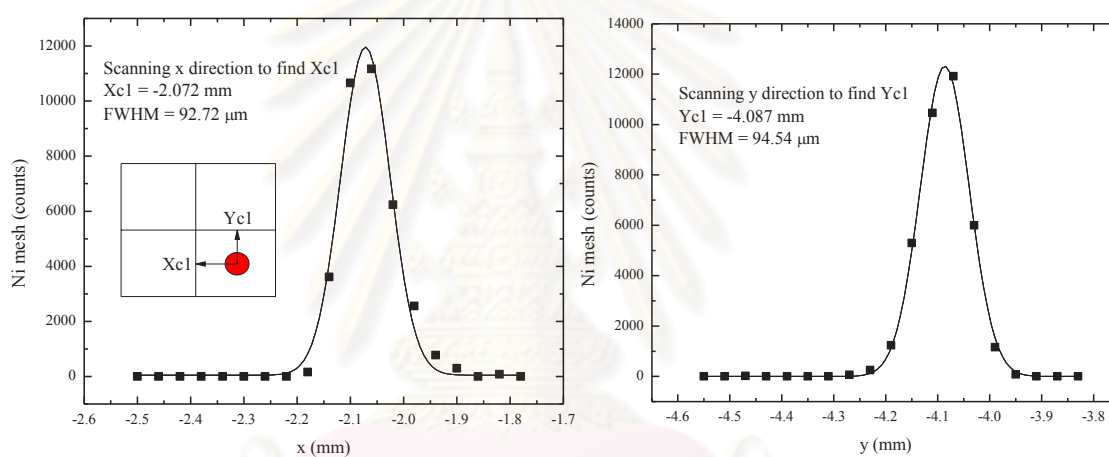


Figure 5.9: Fluorescent signal from Ni K_{α} for both x (left) and y (right) scans.

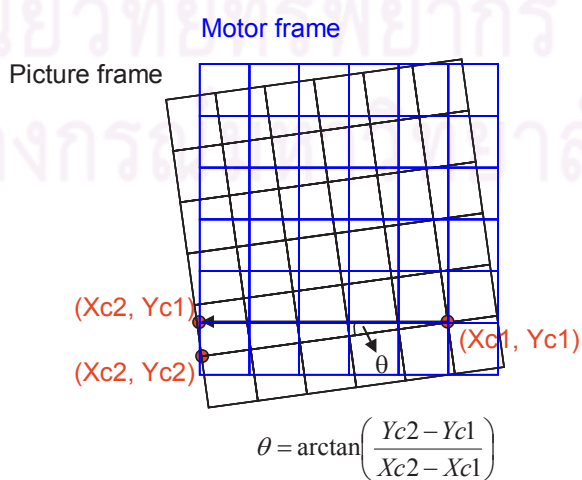


Figure 5.10: Picture frame versus motor frame.

5.3 X-Ray Powder Diffraction

For this thesis, we propose to develop the experimental station for x-ray powder diffraction technique under extreme conditions using a conventional image plate area detector at the Siam Photon Laboratory [6]. The experimental station will be installed and commissioned following the synchrotron beamline on station 9.1, Daresbury laboratory as presented in Figure 5.11 [13].

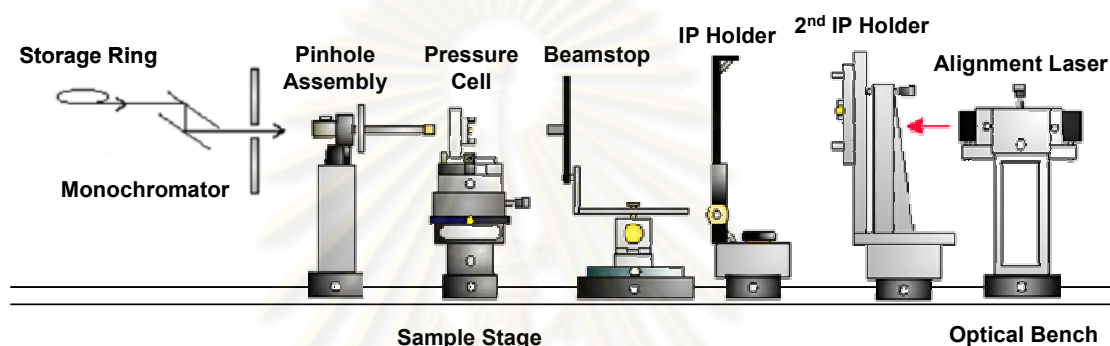


Figure 5.11: Setup for x-ray powder diffraction technique under extreme conditions on the beamline BL-8 at the Siam Photon Laboratory.

X-ray Powder Diffraction using a Polycapillary X-ray Half Lens

For this research, we propose to improve the x-ray synchrotron flux for incident on the sample in the diamond anvil cell; therefore, the idea of focusing lens has been utilized. The polycapillary half lens No.UNS1G-2T-170209 manufactured by UNISANTIS EUROPE GmbH has been used in order to obtain a micro monochromatic x-ray beam for diffraction technique. The specifications of the capillary are listed in Table 5.2. The setup using the capillary lens is presented in Figure 5.12.

The monochromatic x-ray beam with a photon energy of 8823.86 eV from bending magnet is utilized instead of which a photon energy of 9000 eV because the motor of DCM at beamline BL2 cannot move to the required angle. A double Si (111) monochromator is used for selecting the required wavelength for angle dispersive x-ray diffraction. A platinum pinhole with diameter of 200 μm is used for adjusting the beam shape to circular beam. The x-ray beam is perpendicular to the faces of the DAC and incident to powder sample inside the DAC. After the

Table 5.2: Specifications of the Polycapillary half lens No.UNS1G-2T-170209

Polycapillary half lens No.UNS1G-2T-170209	Specifications
Unit length (mm)	38.0
Unit diameter (mm)	14.5
Outlet focal distance (mm)	223
Optical inlet diameter (mm)	11.0
Focal spot size for Cu line (μm)	850

beam passing through the DAC, the beamstop is used for protecting the image plate detector from direct beam. The distance between IP and sample is 70 mm. In order to align the setup, an optical method using a laser employed at Photon Factory [69] is used. The telescope is used for positioning on the sample through the DAC and is removed during exposures.

We utilize the ruby fluorescence technique for pressure determination inside the DAC. The pressure measurement were carried out before and after collecting x-ray powder diffraction data. The Diode Pumped Solid State (DPSS) laser with wavelength of 532 nm is used for stimulating electron inside the ruby crystal to emit the fluorescence. We focus the laser beam on a tiny ruby crystal inside the DAC. After that the collected spectra are compiled by a computer. The pressure inside the DAC can be calculated using the shifting of R_2 line fluorescence as presented in Figure 5.13,

$$P = \frac{19040}{B} \left[\left(\frac{\Delta\lambda}{\lambda_0} + 1 \right)^B - 1 \right], \quad (5.1)$$

where P is in kbar, $\Delta\lambda$ is the ruby R_2 line wavelength shift in angstroms and parameter B is equal to 5 and 7.665 for non-hydrostatic and quasi-hydrostatic conditions, respectively. λ_0 is the wavelength measured at 1 bar in angstroms equal to 6942 for R_1 line and 6928 for R_2 line.

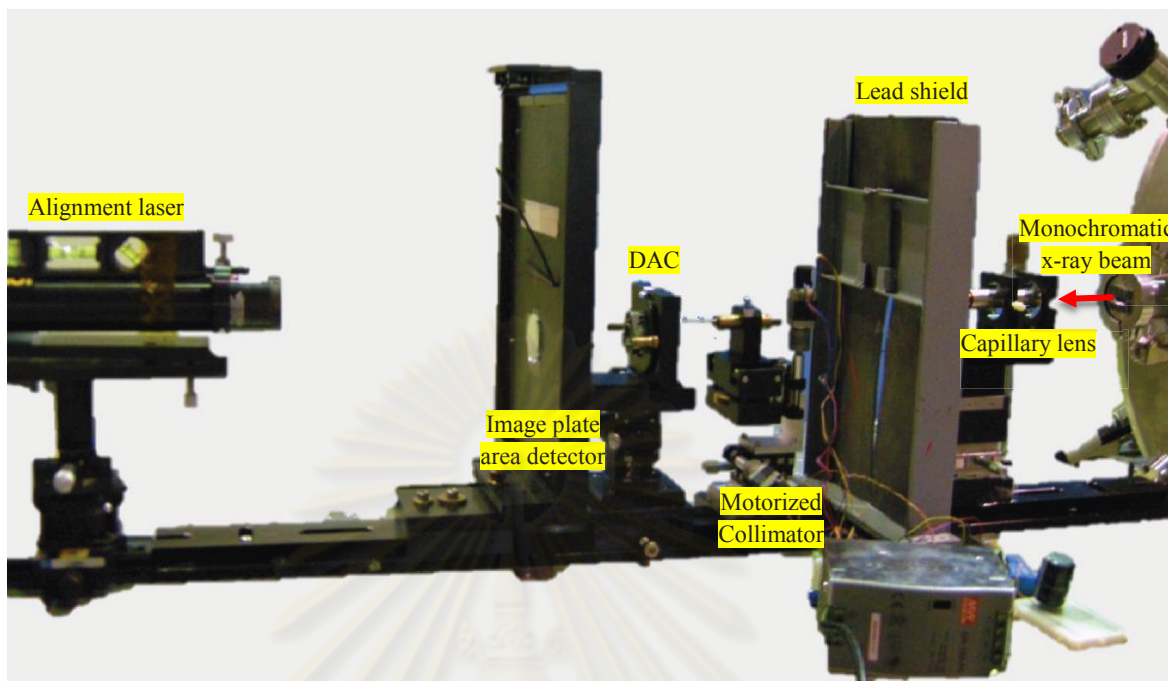


Figure 5.12: Setup for x-ray powder diffraction technique under extreme conditions using the polycapillary lens on the beamline BL-2 at the Siam Photon Laboratory.

The recorded diffraction patterns from many particle size of CeO_2 (10-20, 20-30 and 32-40 nm) and also calibrant Al_2O_3 will be presented in chapter 6.

Micro-Electrical Discharged Machine

Micro-Electrical Discharge Machine (Micro-EDM) is a high precision drilling machine for conductive material especially for micro-fabrication. The EDM process was created by the Russian scientists named B.R. Lazarenko and N.I. Lazarenko [71] in 1943 and has been used in the tool making industry for more than 40 years. Due to its high precision capability and fine cutting surface quality produced, micro-EDM is widely used in the production of DAC gasket for high pressure applications. The idea for the process is to apply an electrical power to a small gap between a highly charged electrode and a work piece in a dielectric medium. When EDM spark discharges into a gap, a small part of the work piece will be gradually eroded away. The micro-EDM have many advantages; for example, producing complex shapes which is difficult to machine with conventional

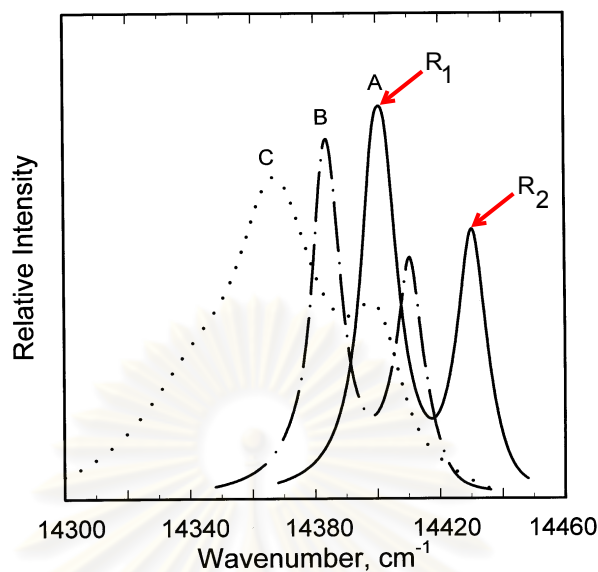


Figure 5.13: R-line fluorescences of a ruby crystal in the DAC at room temperature are shown; ruby crystal: at ambient pressure (A); at about 22.3 kbar (B); at about 40 kbar (C). The pressure shift is to lower energy with increasing pressure. [70]

drilling machines, applying to either soft or extremely hard materials and being safe for very tiny work piece. On the other hand, this process cannot machine non-conductive material and is significantly slower than either laser or mechanical drilling.

For the Extreme Condition Physics Research Laboratory, Chulalongkorn University, the micro-EDM is used for tungsten gaskets preparation. The micro-EDM can drill tungsten sheet with a thickness of 100 micron in less than 20 minutes. The holes can be as small as 50-100 microns in diameter for containing the powder sample and ruby chip. Figure 5.14 shows the old micro-EDM adapted from Lorenzana *et al.* [72] used at the Extreme Condition Physics Research Laboratory. The disadvantages for this machine are inability to control gap and time for spark as well as missing position if we change from drilling head to microscope and then moves back. In order to minimize error for the process, the drilling machine is upgraded to the motorized machine, using the precise translation stage with resolution only 1 μm and the idea of rotation around pivot as expressed in

Figure 5.15. The crucial improvement for the new micro-EDM is to optimize the parameters for high precision drilling as well as the upgraded electronic devices for erosion circuit. We have to consider the energy for melting work piece carefully because the high energy will make the work piece's surface rough. The designed drilling circuit which have been optimized for drilling small gasket holes is shown in Figure 5.16. Firstly, the capacitor is the charge reservoir for supplying the high power during the discharge process. Secondly, the resistor R_1 with resistance 5Ω is used as the discharge rate controller for the capacitor. Finally, the resistor R_2 with resistance 160Ω is used as a high-wattage current limiter for the short circuit between the drilling tool and workpiece. New micro-EDM machine is presented in Figure 5.17.



Figure 5.14: Old micro-EDM used at the Extreme Condition Physics Research Laboratory, Chulalongkorn University.

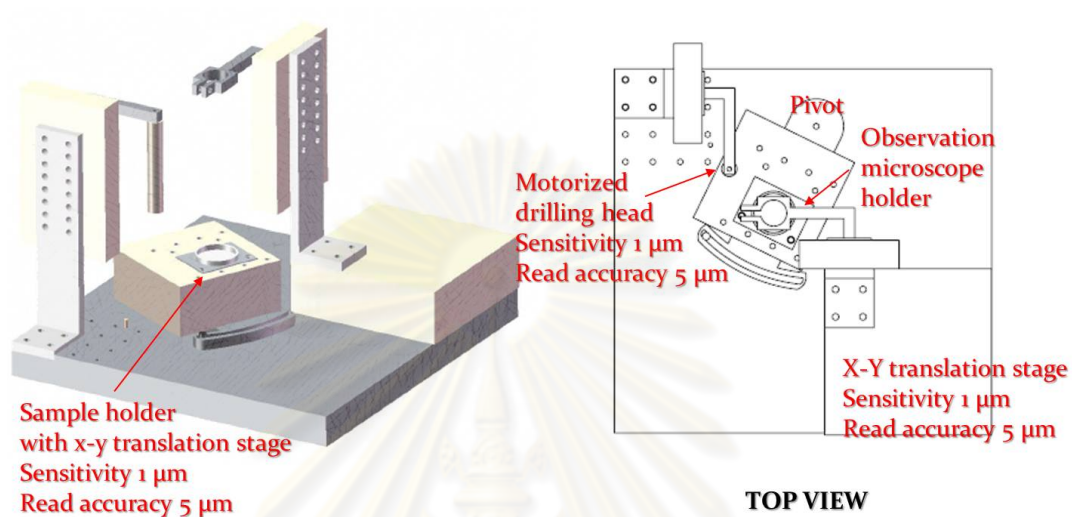


Figure 5.15: Schematic layout for drilling machine.

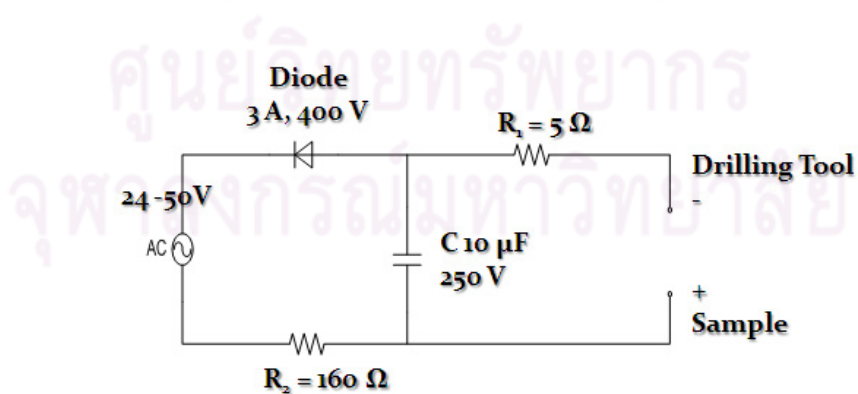


Figure 5.16: Schematic diagram of the drilling circuit.

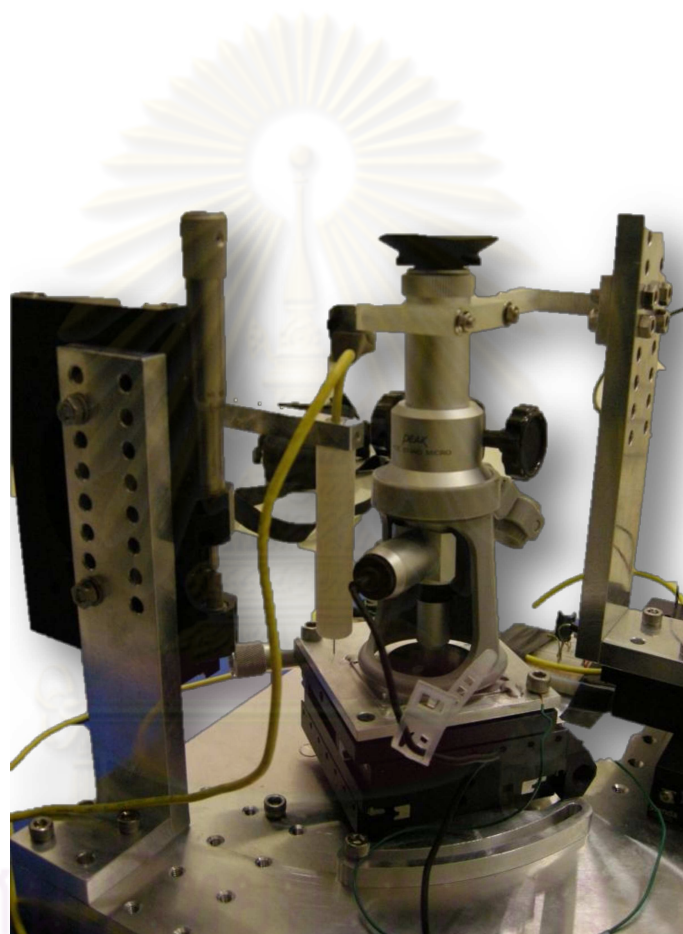


Figure 5.17: New micro-EDM.

จุฬาลงกรณ์มหาวิทยาลัย

CHAPTER VI

RESULTS AND DISCUSSIONS

6.1 Ray Tracing Simulation

Synchrotron Beamline Optics for X-ray Powder Diffraction under High Pressure Condition at the Siam Photon Laboratory

According to the complete diffraction pattern of the hexagonal phase of ZnO under ambient condition at beamline BL8 using an image plate area detector as shown in Figure 6.1 [6], we found that the technique requires x-ray beam with higher flux. Here we propose an XRPD beamline to deliver a focused x-ray beam with high photon flux as presented in Figure 6.2.

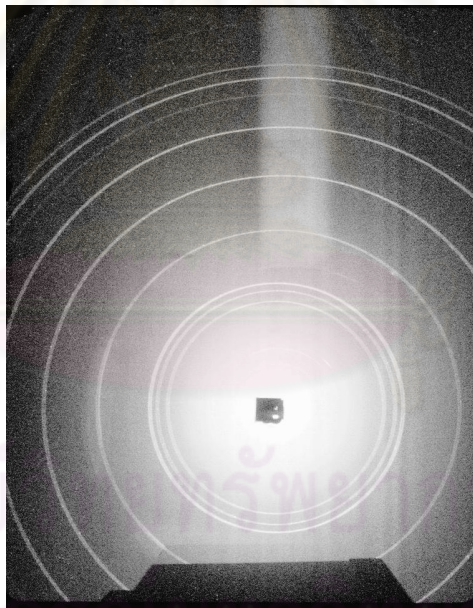


Figure 6.1: Complete diffraction pattern of the hexagonal phase of ZnO under ambient condition at beamline BL8.

Beamline Optics

Double Multilayer Monochromator

A W/B_4C multilayer (ML) with a small double layer period (d-spacing) of 10 \AA , 600 layer pairs and a ratio of metal to double layer thickness (Γ) of 0.5 is selected for this XRPD beamline. The fabrication and characterization of this

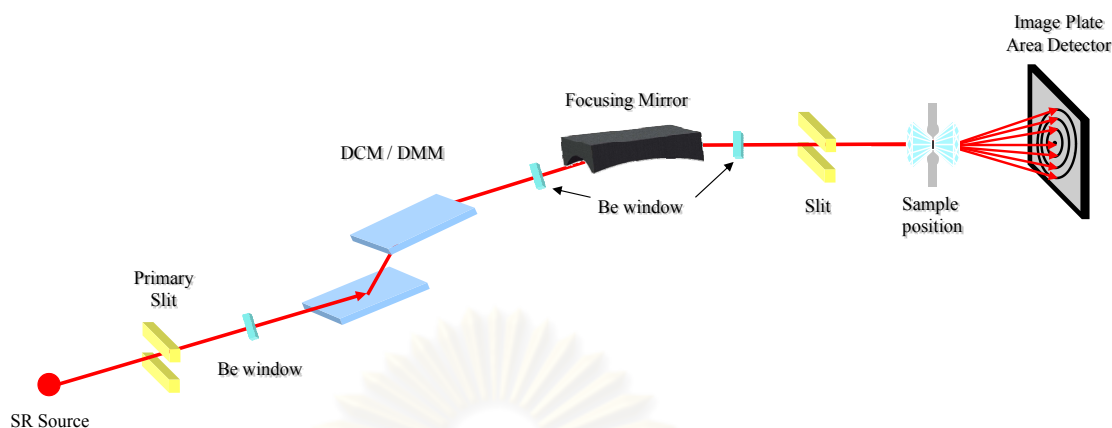
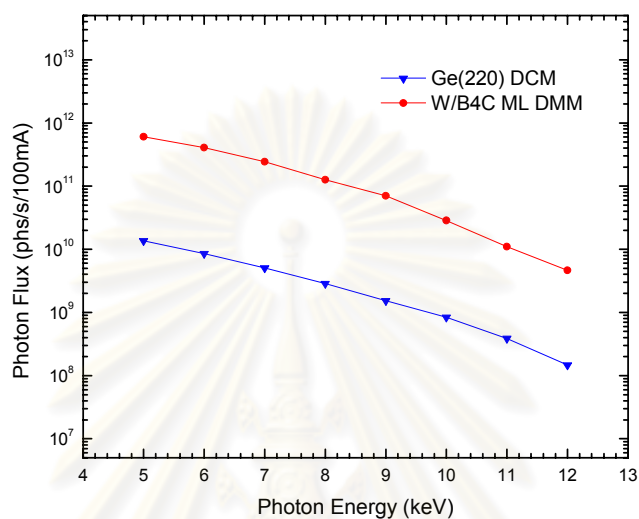
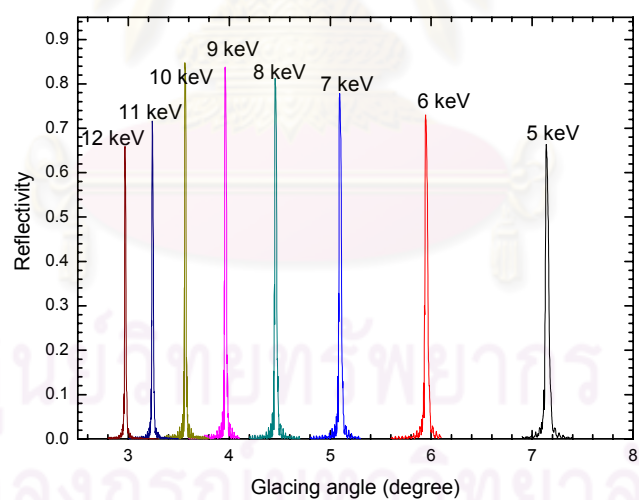


Figure 6.2: Schematic layout of the proposed XRPD beamline for the Siam Photon Laboratory.

mirror was reported by S. Braun *et al.* [73]. Figure 6.3(a) shows a comparison of the simulated photon flux from the Ge(220) DCM and from the W/B_4C DMM. In overall, the W/B_4C DMM provides photon flux about 46 times higher than that of the Ge(220) DCM. This is mainly attributed to the larger natural bandwidth of the W/B_4C DMM. At 9 keV, the bandwidth of the W/B_4C DMM is 86.0 arcsec while that of the Ge(220) crystal is only 11.8 arcsec. The opening angle of $3.0(\text{h}) \times 0.417(\text{v}) \text{ mrad}^2$, which was defined by the primary slit (see Figure 6.2), was selected for calculating the photon flux given by the W/B_4C DMM. The vertical angle was set equal to the W/B_4C bandwidth and the horizontal angle was selected to match the width of the focusing mirror as described in section .Focusing Mirror. In case of the Ge(220) DCM the opening angle of $1.75(\text{h}) \times 0.125(\text{v}) \text{ mrad}^2$ is normally used at the BL8. The reflectivity of the W/B_4C ML for different photon energies as a function of glancing angle is presented in Figure 6.3(b). The rocking curve in figure 3 shows the bandwidth of 86.0 arcsec for W/B_4C ML tuned at 9 keV. This corresponds to an energy resolution ($\Delta E/E$) of 6.0×10^{-3} . It should be noted that the W/B_4C DMM yields higher flux than Ge(220) DCM at the cost of energy resolution.



(a)



(b)

Figure 6.3: Comparison of simulated photon flux between DCM: Ge(220) and DMM: W/B_4C ML for a photon energy range of 5-12 keV and opening angle of $1.75(h) \times 0.125(v)$ mrad² is shown in (a). Reflectivity of W/B_4C ML with $d = 10 \text{ \AA}$, $N = 600$ and $\Gamma = 0.5$ is shown in (b).

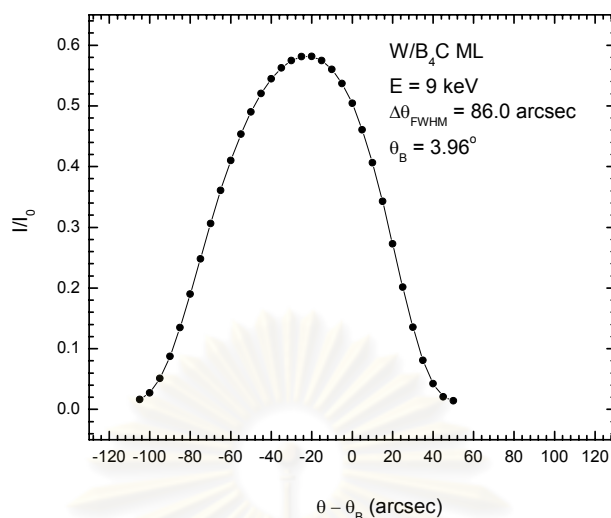


Figure 6.4: Simulated rocking curve for the DMM with W/B_4C ML at 9 keV.

Focusing Mirror

We choose Rh 5 nm/ Pt 25 nm for optical coating on the mirror. The mirror body may be silicon single crystal or ultra low expansion (ULE) fused silica. The suitable glancing angle (θ_c) for the XRPD technique in a photon energy range of 5-12 keV is 5 mrad. This is shown in figure 6.5. For the same length of the mirror, i.e. 1 meter, the mirror set at 3 mrad glancing angle accepts 30% less of the beam than in the case of 5 mrad with slightly higher reflectivity, thus the overall beam intensity throughput of 3 mrad is lower than that of 5 mrad.

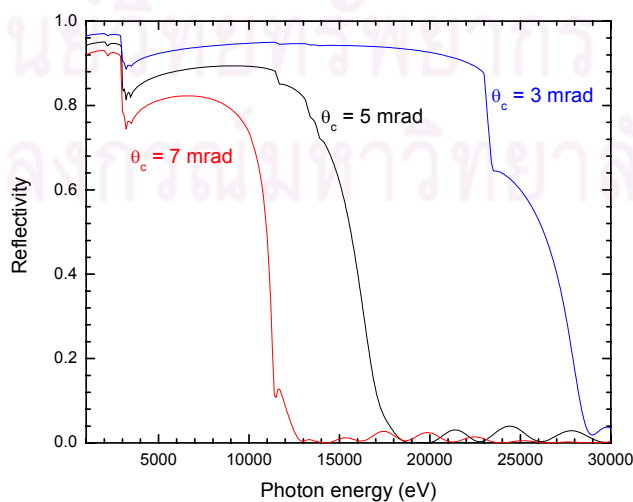


Figure 6.5: Calculated reflectivity of Rh 5 nm/ Pt 25 nm coated on silicon mirror with $\theta_c = 3, 5$ and 7 mrad.

In order to determine the best magnification of the toroidal focusing mirror, ray-tracing simulation was carried out with the aid of SHADOW [14]. A primary x-ray beam from a bending magnet synchrotron source was generated at 2% bandwidth with energy centered at 9 keV. Different mirror magnifications allowed by the available length of the beamline - M0.3, M0.4, M0.5, M0.6 and M0.7 - were tested with the opening angle of $3.0(\text{h}) \times 0.42(\text{v}) \text{ mrad}^2$. The x-ray beam at the image plane could be characterized by the beam size, beam convergence and beam intensity. The results are presented in Figure 6.6 and 6.7. For M0.7, photon flux at sample is highest. Moreover, the focused beam size is smallest and spatially symmetric. The expected flux at sample through a $0.3 \times 0.3 \text{ mm}^2$ aperture is 2.7×10^{10} photons/sec/100mA. Thus, it is about 7500 times higher than that of BL8.



ศูนย์วิทยทรัพยากร
จุฬาลงกรณ์มหาวิทยาลัย

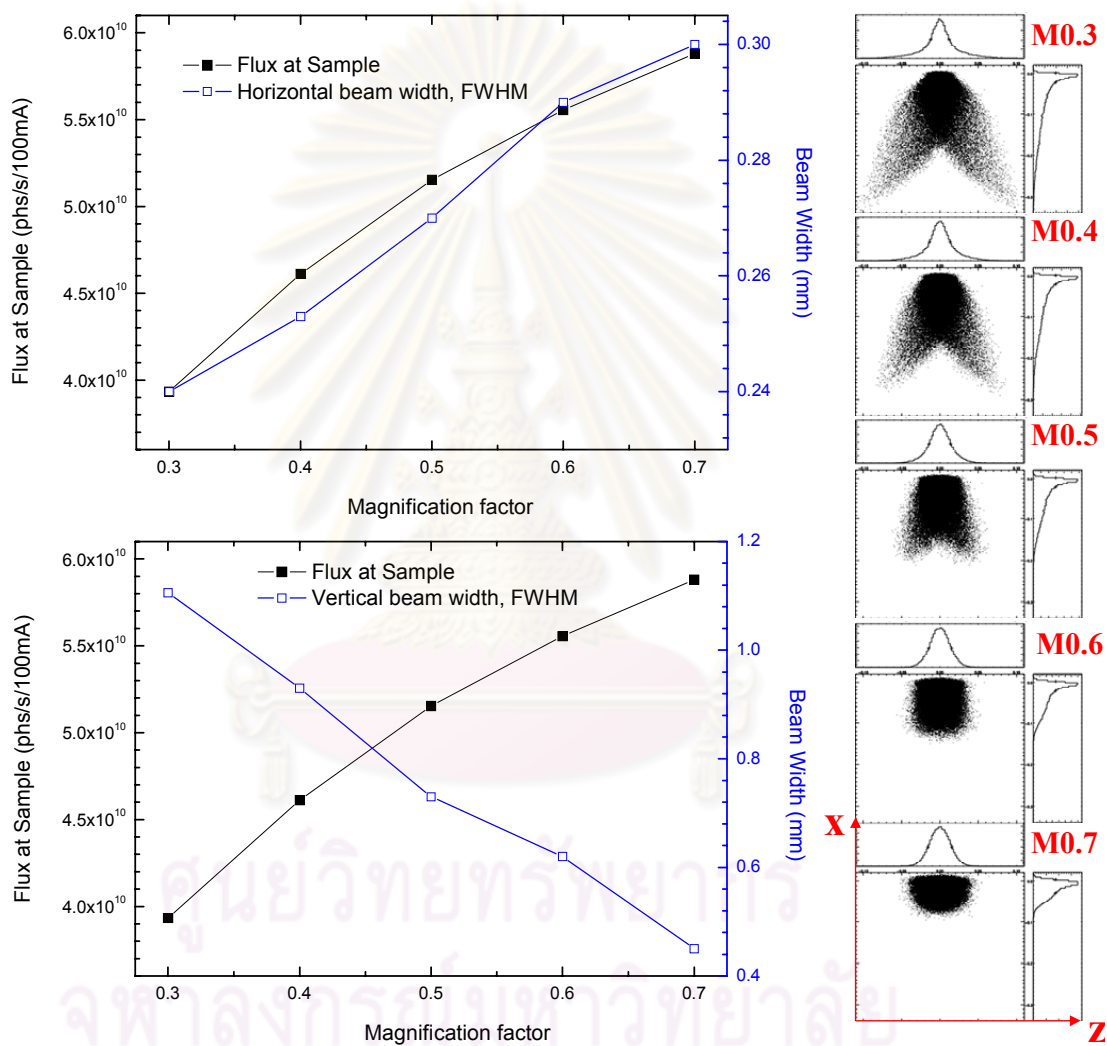


Figure 6.6: Image size at focal plane for the mirror magnifications M0.3, M0.4, M0.5, M0.6 and M0.7.

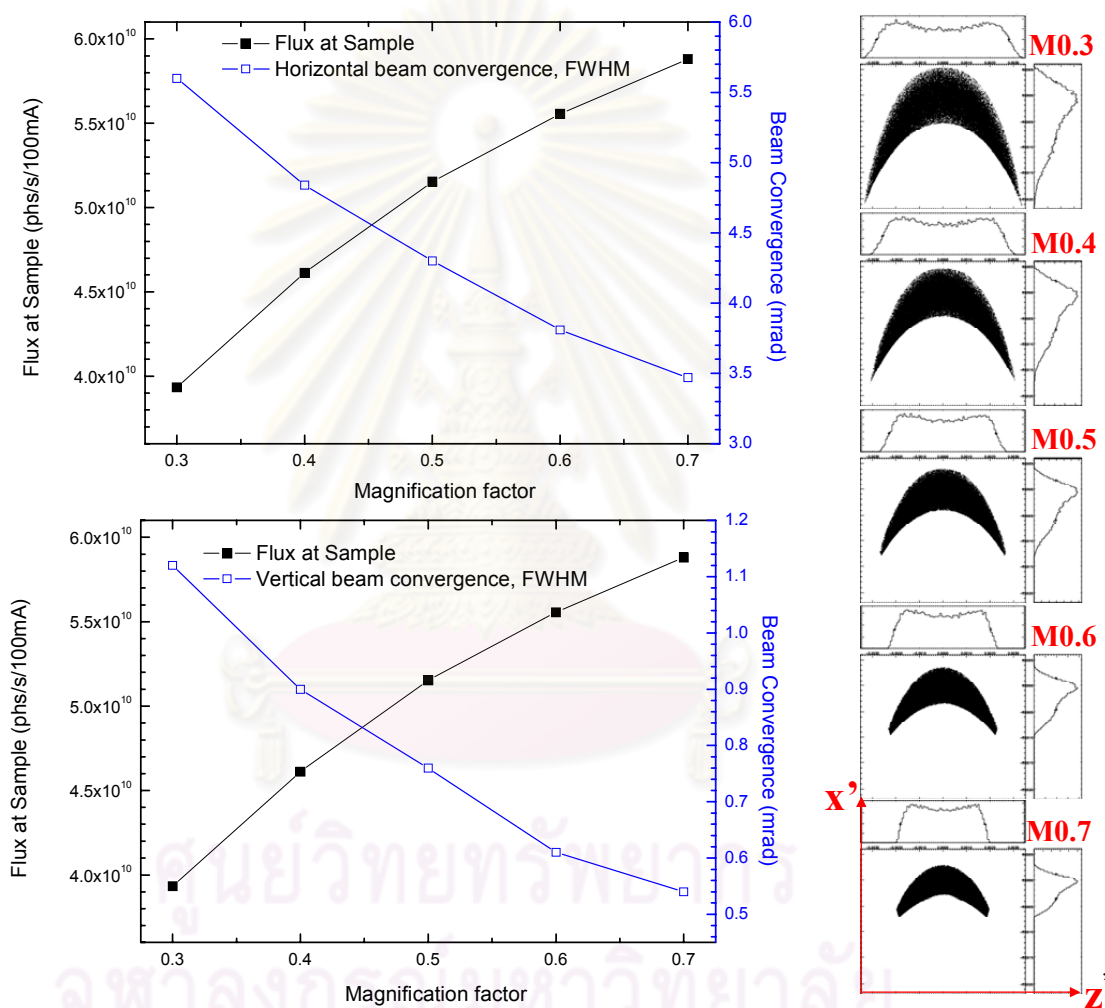


Figure 6.7: Beam convergence at focal plane for the mirror magnifications M0.3, M0.4, M0.5, M0.6 and M0.7.

Focused monochromatic beam for x-ray absorption spectroscopy and x-ray fluorescent techniques

In order to provide the focused monochromatic beam for x-ray absorption spectroscopy and x-ray fluorescent techniques, a toroidal mirror (TM) or a cylindrical mirror (CM) will be used in the designs for delivering the most suitable monochromatic x-rays following the beamline designs in Figure 6.8.

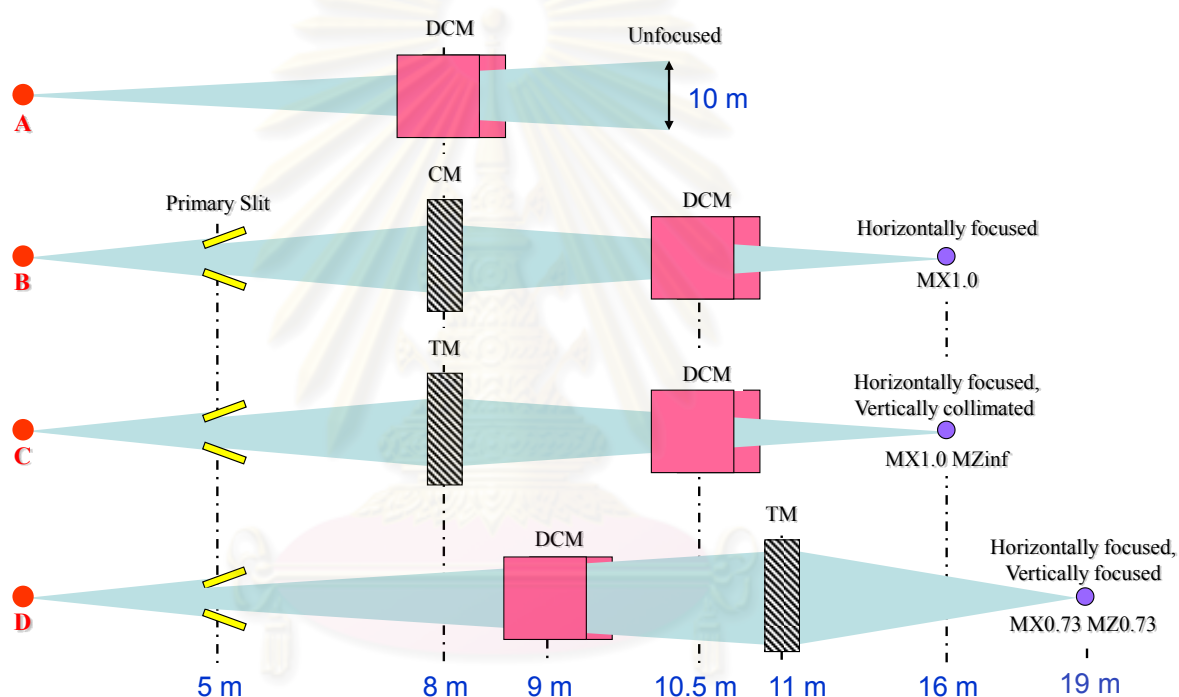


Figure 6.8: Layout for beamline design of the unfocused and focused monochromatic beam for x-ray absorption spectroscopy and x-ray fluorescent techniques.

Magnifications of TM and CM are varied in many conditions for optimization the x-ray beam as indicated in Figure 6.8. Case A presents an unfocused x-ray beam. Case B represents a horizontally focused beam using the CM with horizontal magnification, MX1.0. In order to provide the horizontally focused and vertically collimated beam, the TM with magnification MX1.0 MZinf is inserted between SR source and the DCM in case C. The mirrors in both cases B and C are inserted in front of the DCM in order to reduce their length. For the last case (case

D), we provide the horizontally and vertically focused beam by inserting the TM with magnification MX0.73 MZ0.73. In cases B and D, SR source distributions are varying according to the limited size of the DCM and the mirror. Parameters of synchrotron radiation source for all cases of beamline designs are presented in Table 6.1. In addition, the optical elements and some simulated results are expressed in Table 6.2.

Table 6.1: Parameters of synchrotron radiation source for designing x-ray beamline.

Case	SR source distribution ($mrad^2$)	Primary slit size at 5 m (mm^2)	Crystal size for Si(111) (mm^2)
A: unfocused	1 (h) \times 0.125 (v)	-	20 (w) \times 40 (l)
B1: MX1.0	3 (h) \times 0.125 (v)	15 (h) \times 0.625 (v)	20 (w) \times 40 (l)
B2: MX1.0	3.5 (h) \times 0.125 (v)	17.5 (h) \times 0.625 (v)	20 (w) \times 40 (l)
B3: MX1.0	4.0 (h) \times 0.125 (v)	20 (h) \times 0.625 (v)	20 (w) \times 40 (l)
C: MX1.0MZinf	3.0 (h) \times 0.4 (v)	15 (h) \times 2.0 (v)	20 (w) \times 40 (l)
D1: MX0.73MZ0.73	2.0 (h) \times 0.125 (v)	10 (h) \times 0.625 (v)	20 (w) \times 40 (l)
D2: MX0.73MZ0.73	3.0 (h) \times 0.125 (v)	15 (h) \times 0.625 (v)	30 (w) \times 40 (l)
D3: MX0.73MZ0.73	4.0 (h) \times 0.125 (v)	20 (h) \times 0.625 (v)	40 (w) \times 40 (l)

Concerning mirror absorption

Absorption of the mirror depends on coated material. Moreover, we need to choose the most proper coated material for optimizing the results. Rhodium (Rh), silicon (Si) and double layer of Rh and platinum (Pt), Rh 5 nm/Pt 25 nm, are chosen for coating on the toroidal and the cylindrical mirror in order to simulated ray tracing for all cases of beamline designs. The reflectivity for Rh, Si and also Rh 5/Pt 25 nm for a photon energy range of 1-15 keV is shown in Figure 6.9.

According to the reflectivity of Si for a photon energy range of 1-3 keV, it affects on K-edge of Si and L-edges of Sr, Y as described in Figure 6.10. Figure 6.11 illustrates the reflectivity of Rh 5/Pt 25 nm for a photon energy range of 1.4-3 keV. The simulated reflectivity indicates that it affects on K-edge of P, L-edge of

Table 6.2: Parameters of optical elements

Parameter	Beamline Design											
	A	B1	B2	B3	C1	C2	C3	D1.1	D2	D1.2	D3	
DCM, Si(111) - 1 st crystal position (m)	8	10.5			10.5			9				
Mirror type	-	CM			TM							
Mirror position (m)		8			8			11				
Mirror size (cm)	-	100 (l) x 5.4 (w)										
Coated material	-	Si	Rh	Rh 5/ Pt 25 nm	Si	Rh	Rh 5/ Pt 25 nm	Si	Rh	Rh 5/ Pt 25 nm		
Major radius (R, km)	-	-			5.33	3.2	2.67	3.088	1.85	1.54		
Minor/Spherical radius (ρ , cm)	-	2.4	4	4.8	2.4	4	4.8	2.78	4.63	5.558		
Glancing angle (mrad)	-	3	5	6	3	5	6	3	5	6		
Sample position (m)	10	16	16	16	16	16	16	19	19	19	19	
• beam size at 5 keV (FWHM)												
h (mm)	10.1	1.22	1.49	1.58	0.574	0.55	0.54	0.29	0.275	0.3	0.274	
v (mm)	1.21	2.73	3.5	3.82	2.22	2.2	2.4	0.45	0.44	0.45	0.538	
• beam divergence at 5 keV (FWHM)												
ϕ_h (mrad)	0.991	2.17	3.41	3.9	1.95	2.8	2.81	2.05	3.35	2.56	4.12	
ϕ_v (mrad)	0.124	0.111	0.11	0.122	0.145	0.131	0.15	0.375	0.802	0.3	0.592	
ΔE (FWHM) at 5 keV	1.385	1.265	1.28	1.28	1.954	1.775	1.59	1.275	1.275	1.275	1.275	
$\Delta E/E$ at 5 keV	2.77×10^{-4}	2.53×10^{-4}	2.56×10^{-4}	2.56×10^{-4}	3.91×10^{-4}	3.55×10^{-4}	3.18×10^{-4}	2.55×10^{-4}	2.55×10^{-4}	2.55×10^{-4}	2.55×10^{-4}	
Flux at sample 5 keV	6.86×10^8	1.47×10^{10}	2.0×10^{10}	2.23×10^{10}	1.19×10^{10}	1.35×10^{10}	4.03×10^{10}	1.11×10^{10}	1.71×10^{10}	1.13×10^{10}	1.98×10^{10}	

^a FWHM values correspond to 80% population.

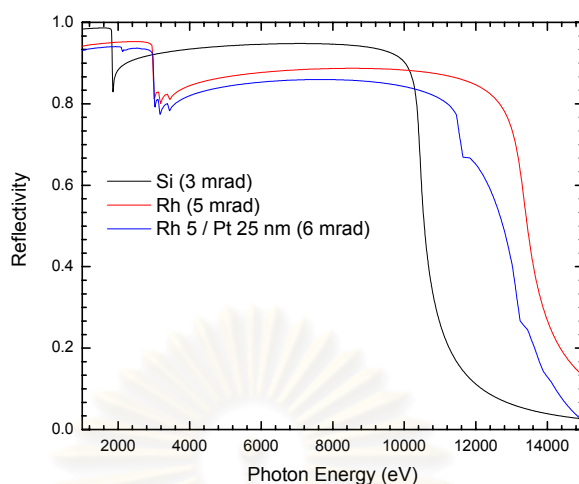


Figure 6.9: Reflectivity for Si with glancing angle of 3 mrad, Rh with glancing angle of 5 mrad and Rh 5/Pt 25 nm with glancing angle of 6 mrad for a photon energy range of 1-15 keV.

Tc and M-edges of Pt, Hf, Ta, Ho and also Er. In addition, if neither Rh 5/Pt 25 nm nor Rh is used for coating the mirror, its reflectivity for a photon energy range of 2800-3600 eV has an effect on the absorption edge of many materials as illustrated in Figure 6.12.

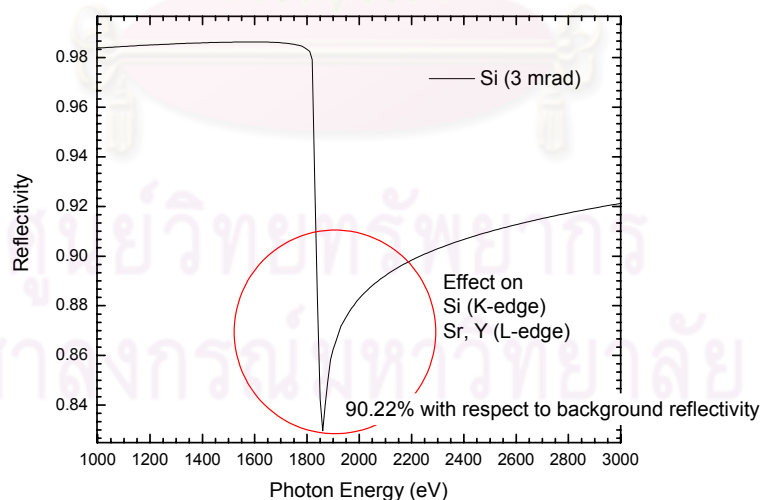


Figure 6.10: Reflectivity for Si with a glancing angle of 3 mrad for a photon energy range of 1000-3000 eV.

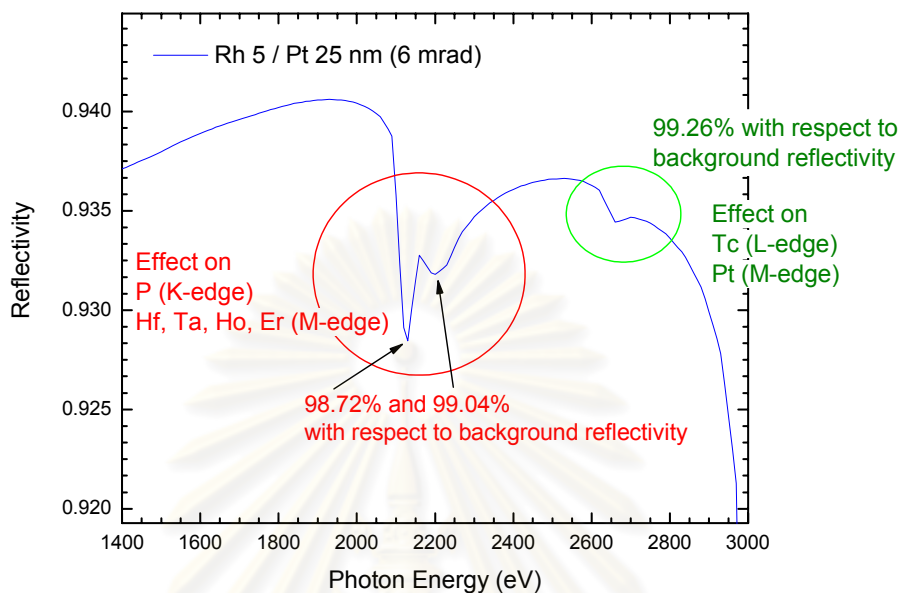


Figure 6.11: Reflectivity for Rh 5/Pt 25 nm with a glancing angle of 6 mrad for a photon energy range of 1400-3000 eV.

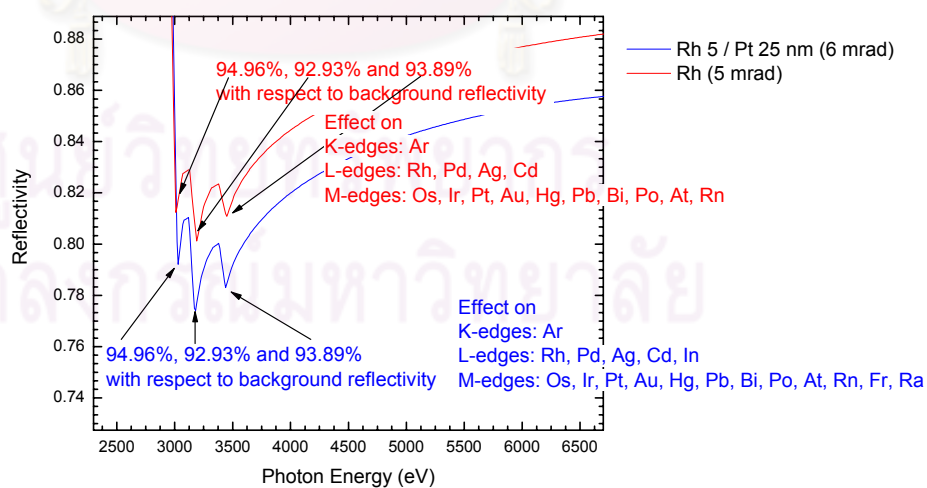


Figure 6.12: Reflectivity for Rh with a glancing angle of 5 mrad and Rh 5/Pt 25 nm with a glancing angle of 6 mrad for a photon energy range of 2300-6700 eV.

Ray tracing simulations of the beam width and beam divergence at focal plane for various cases for a photon energy of 5 keV are illustrated in Figure 6.13 and 6.14 respectively. The flux at sample and energy resolution for photon energies of 2.5, 5, 7.5 and also 10 keV are presented in Figure 6.15(a) and 6.15(b) respectively.

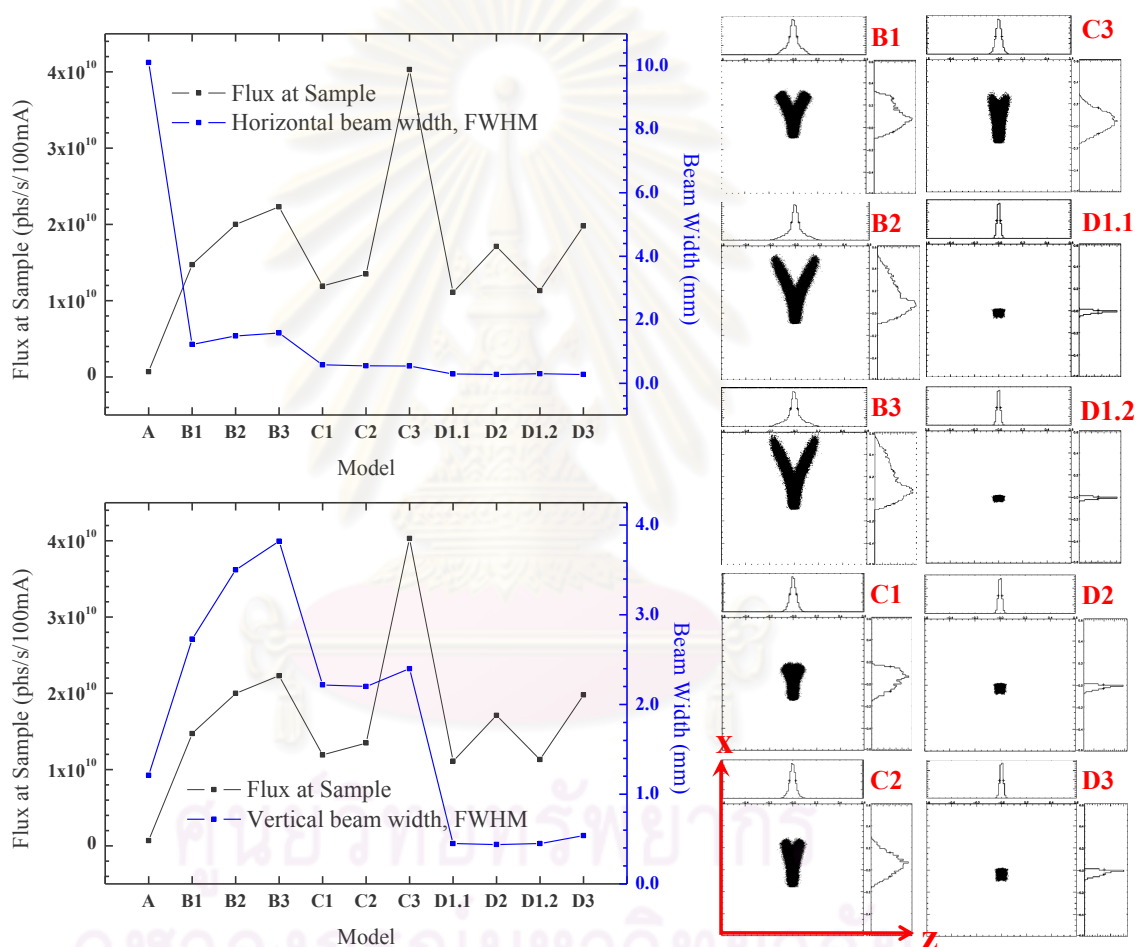


Figure 6.13: Image size at focal plane.

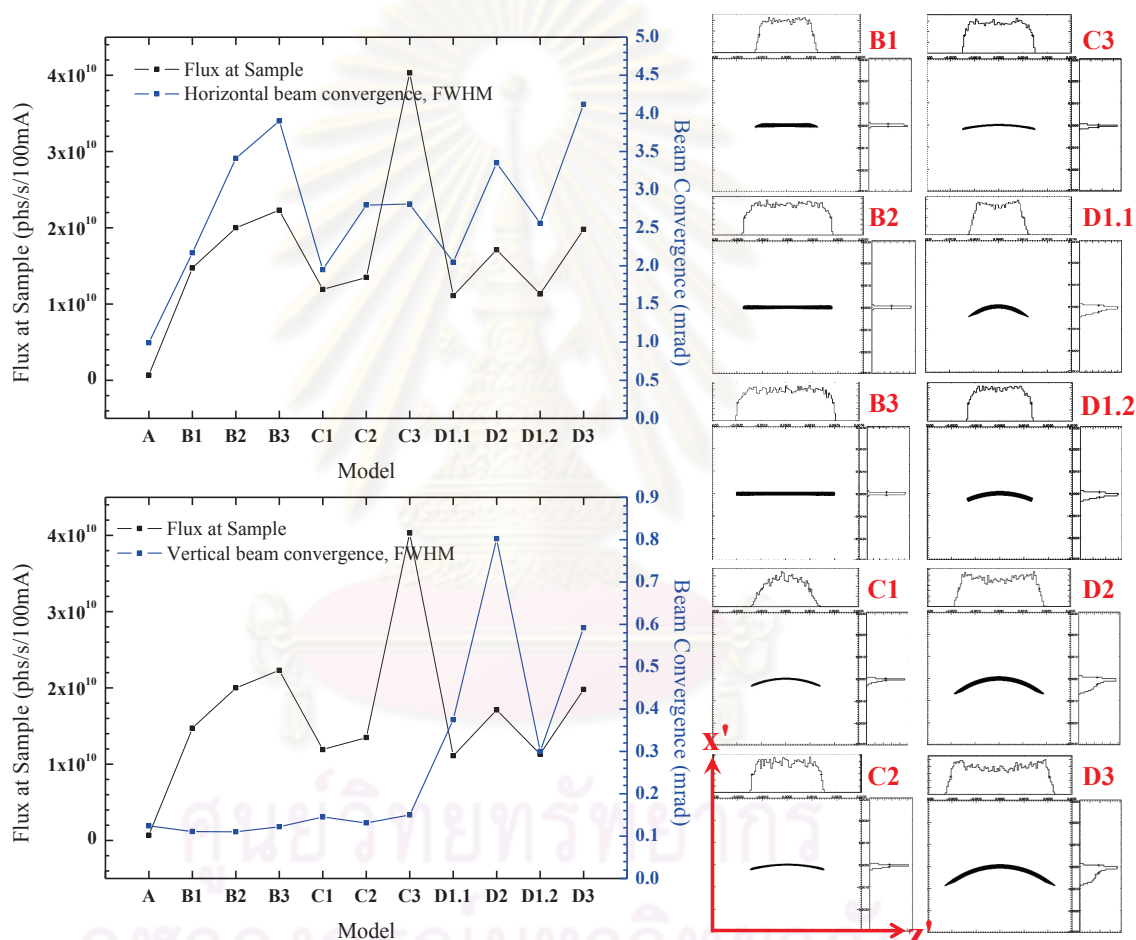
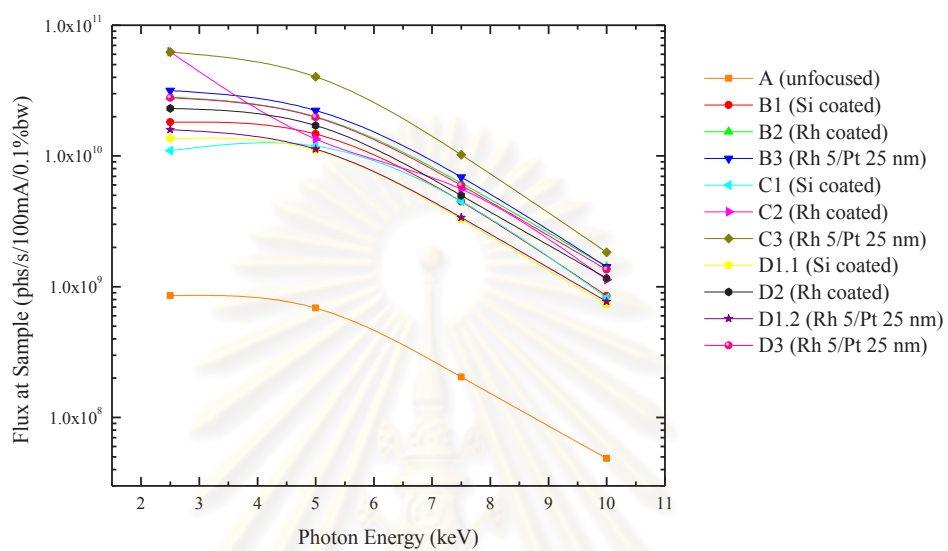
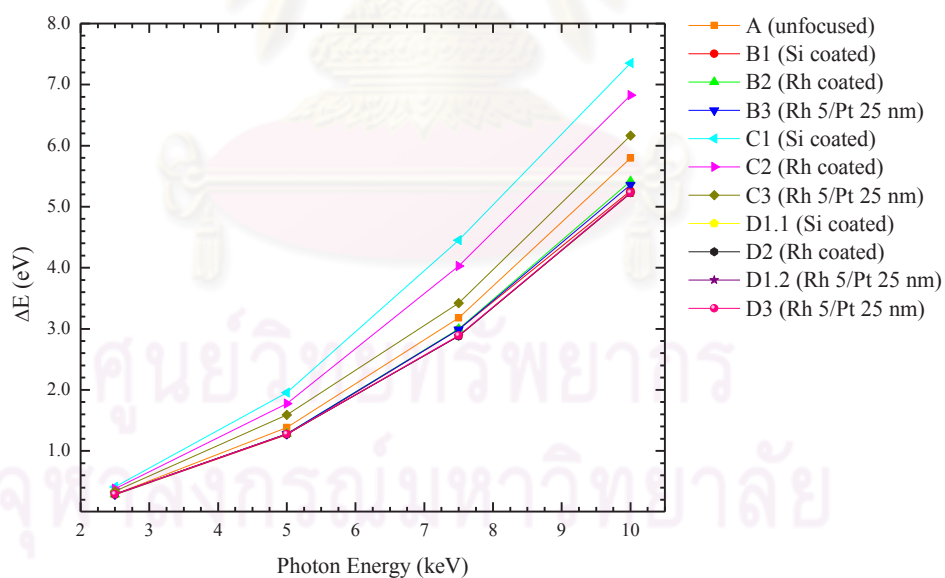


Figure 6.14: Beam convergence at focal plane.



(a)



(b)

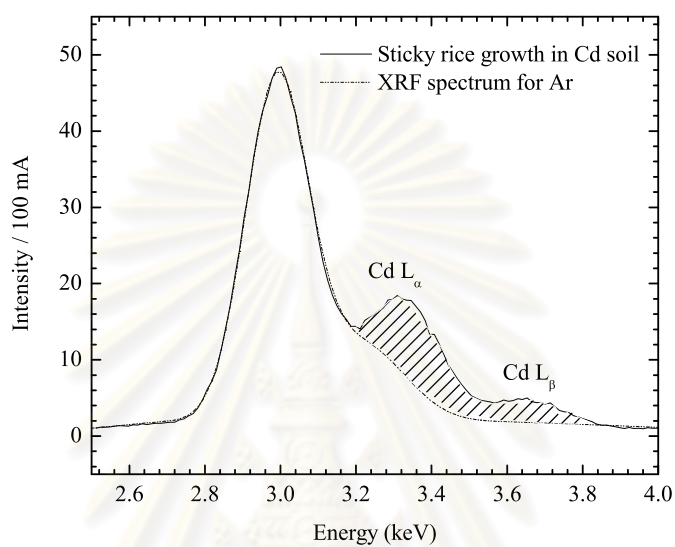
Figure 6.15: (a) Flux at sample and (b) energy resolution for all cases of beamline designs.

6.2 X-Ray Fluorescent Analysis

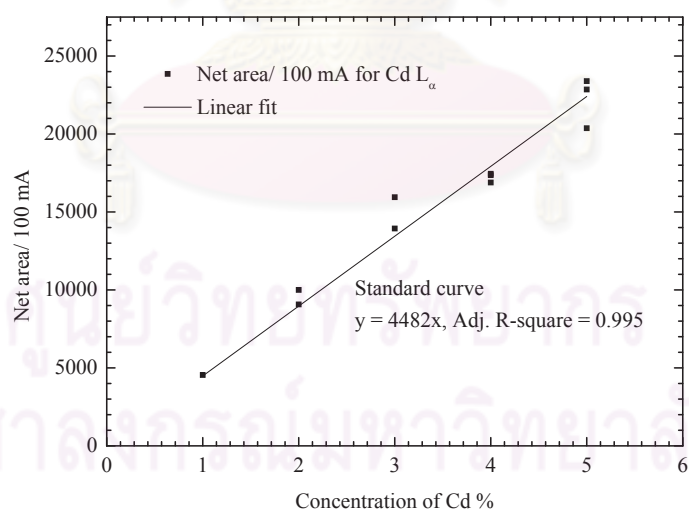
Cadmium in sticky rice powder

Cadmium (Cd) in sticky rice powder obtained from sticky rice which grew in soil containing high amount of Cd was used as a sample for testing the XRF quantitative analysis apparatus. Figure 6.16(a) displays the fluorescence spectrum from this sample in the vicinity of Cd L_{α} . To obtain calibration curve of Cd in sticky rice, five standards were prepared by mixing a controlled sticky rice powder with CdO (purity 99.99 %) at 1, 2, 3, 4 and 5% w/w of Cd. Figure 6.16(b) shows the calibration curve derived from the concentrations of Cd in the standards and measured net areas of the fluorescence Cd L_{α} peaks. The LLD for Cd is 60 ppm. Using a linear fit with zero intercept, the equation $y = 4482x$ was obtained for the best fit (Adjusted coefficient of determination, Adj. R-square = 0.995), where y is the net area (counts) and x is concentration (% w/w) of Cd. The recorded net area of Cd in the sticky rice powder is 1181 (with a standard deviation of 350); therefore, the amount of Cd in the sample is 0.26% w/w. This sample was also measured with an ED-2000 energy dispersive XRF system (at the Scientific and Technology Research Equipment Center, Chulalongkorn University, Thailand) operated in vacuum with a conventional x-ray source. Cd in the sample could hardly be detected.

In order to repeat the experiment, the sample was measured again at the beamline BL6. The best fit for the standard is a linear fit with zero intercept — the equation $y = 3791x$ (Adj. R-square = 0.992) — where y is the net area (counts) and x is concentration (% w/w) of Cd. The recorded net area of Cd in the sticky rice powder is 1181. According to the standard curve in Figure 6.17, the recorded net area of Cd in the sticky rice powder is 1081 corresponding with the amount of Cd 0.28% w/w in the sample.



(a)



(b)

Figure 6.16: (a) XRF spectrum of Cd in sticky rice powder and (b) Calibration curve derived from the sticky rice standards with varying Cd concentrations.

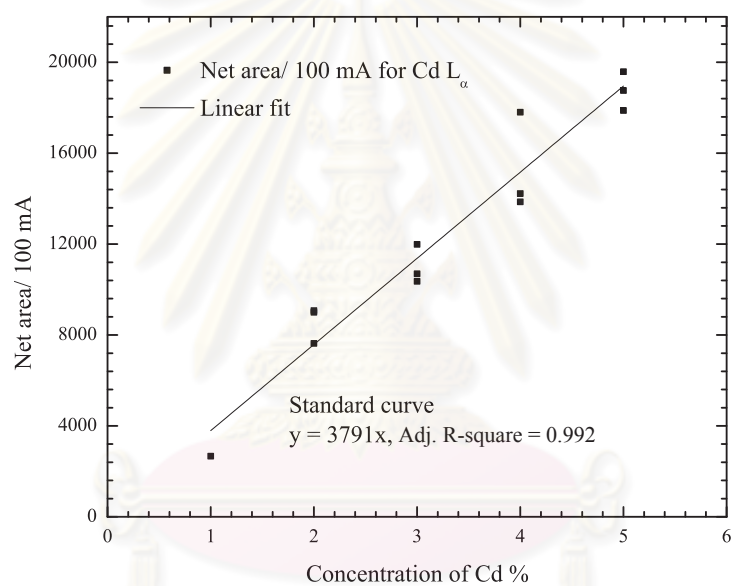


Figure 6.17: Calibration curve derived from the sticky rice standards with varying Cd concentrations. The experiment was repeated using white beam at the beamline BL6.

จุฬาลงกรณ์มหาวิทยาลัย

XRF qualitative analysis and software

Table 6.3 describes the peak fitting from the XRF analysis software. The software can identify those 10 elements in S610 correctly. The photon energies of the characteristic x-rays determined by the software differ from the reference values by less than 22 eV (0.34%).

Table 6.3: Peak fitting for a NIST SRM 610 multi-element glass calibration standard using the XRF analysis software.

Element	Energy (keV)		
	E fit	E theory	ΔE
Calcium $K\alpha_{1,2}$	3.704	3.69	0.014
Calcium $K\beta_1$	4.026	4.013	0.013
Argon $K\alpha_{1,2}$	2.975	2.96	0.015
Manganese $K\alpha_{1,2}$	5.899	5.895	0.004
Iron $K\alpha_{1,2}$	6.422	6.40	0.022
Chromium $K\alpha_{1,2}$	5.415	5.412	0.003
Vanadium $K\alpha_{1,2}$	4.955	4.95	0.005
Cobalt $K\alpha_{1,2}$	6.945	6.925	0.020
Titanium $K\alpha_{1,2}$	4.521	4.509	0.013
Nickel Ni $K\alpha_{1,2}$	7.456	7.472	-0.017
Copper $K\alpha_{1,2}$	8.055	8.041	0.014
Zinc $K\alpha_{1,2}$	8.630	8.631	-0.001

6.3 X-Ray Fluorescent Imaging

Determining the focused beam size

According to the previous chapter (Chapter 5: Experimental Methods), we measure the focused x-ray beam size for both white beam and monochromatic beam by placing the wire at the sample position where the beam is focused.

At first, the polycapillary half lens No.208 has been tested using monochromatic x-rays with a photon energy of 9.5 keV at beamline BL2 for measuring the focused monochromatic x-ray beam size. The experimental set-up is presented in

Figure 6.18.

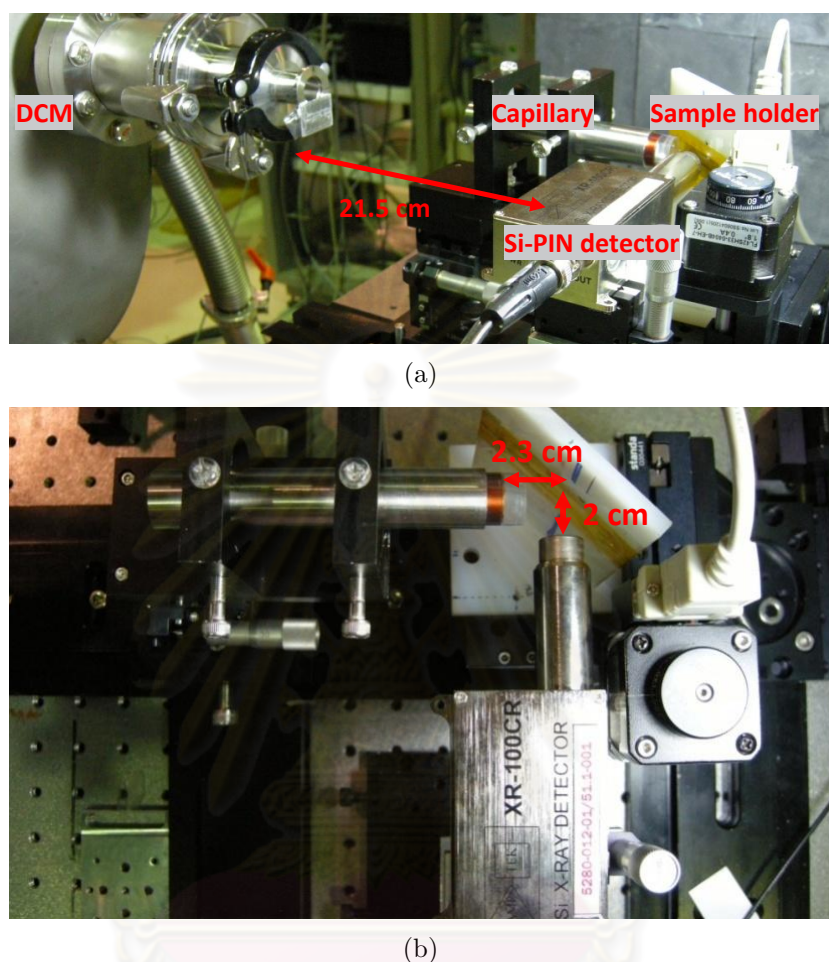
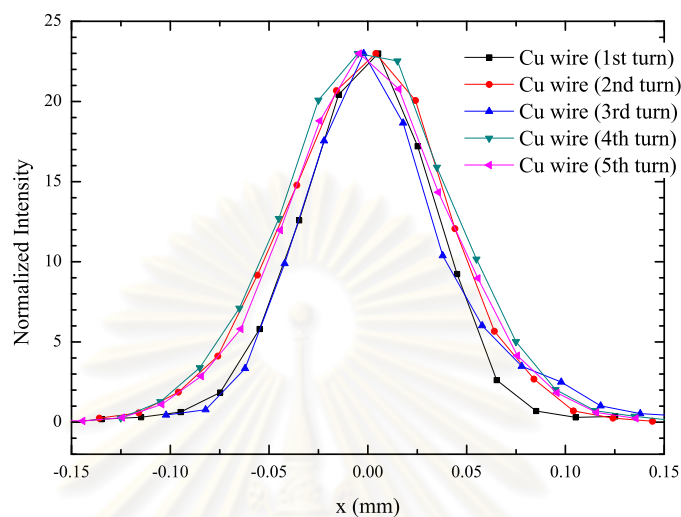


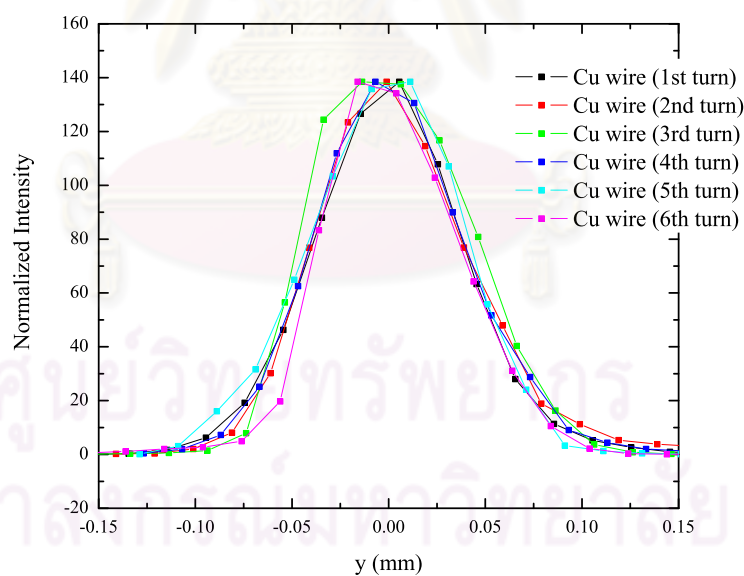
Figure 6.18: Experimental setup for testing the polycapillary half lens No.208 using monochromatic x-rays with a photon energy of 9.5 keV at beamline BL2

Cu wire with ϕ 100 μm was placed at the sample position where the monochromatic x-ray beam was focused. The fluorescent signal at Cu K_{α} (8047.7 eV) from the wire scanning in both horizontal and vertical direction are shown in Figure 6.19. The apparent widths (FWHM) for the fluorescent signal of Cu K_{α} in both horizontal and vertical directions are presented in Table 6.4. To obtain the focused beam size, the apparent widths shown in Figure 6.19(a) and 6.19(b) were deconvoluted with the width of the Cu wire. For this case, the focused beam size is $73 \times 74 \mu\text{m}^2$.

The capillary lens has been tested using white x-rays at beamline BL2 for



(a)



(b)

Figure 6.19: Fluorescent signal from Cu K_{α} for the Cu wire with ϕ 100 μm normalized by the electron beam current scanned in (a) the horizontal direction (x) and (b) the vertical direction (z) for monochromatic x-ray beam. The step size is 50 μm and the counting time is 30 s/step.

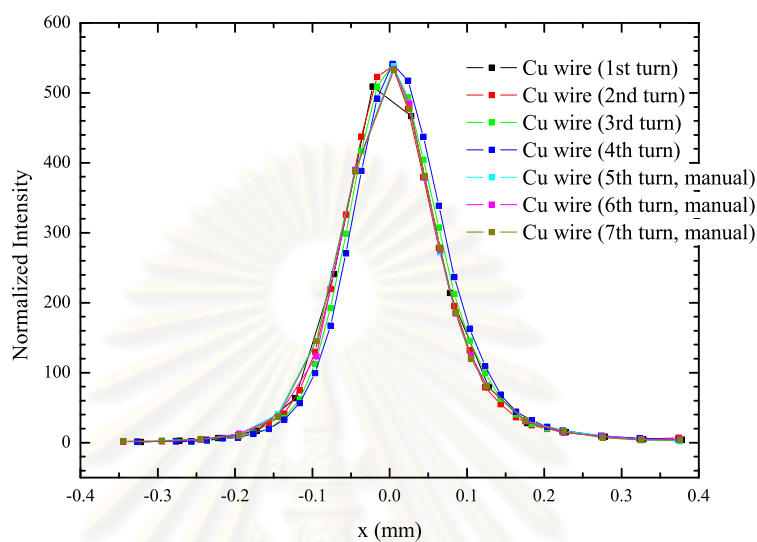
Table 6.4: Apparent widths (FWHM) for the fluorescent signal from Cu K_{α} for the Cu wire with ϕ 100 μm in horizontal (see Figure 6.19(a)) and vertical (see Figure 6.19(b)) directions for monochromatic beam.

No.scanned turn	x FWHM (μm)	y FWHM (μm)
1	73.27	85.19
2	88.20	86.39
3	71.27	97.59
4	95.10	88.55
5	90.42	90.96
6	-	78.48
average	83.65	87.86

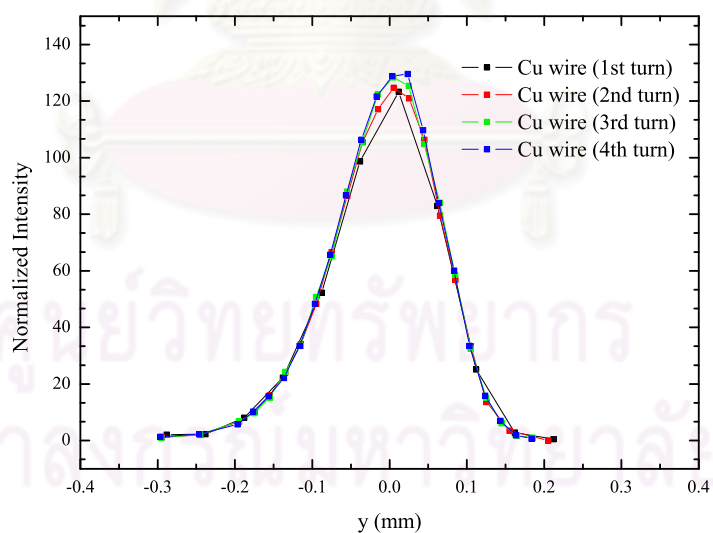
measuring the focused white x-ray beam size too. The Cu wire with ϕ 25 and 100 μm have been used. The fluorescent signal at Cu K_{α} , which is normalized by the electron beam current, in both horizontal and vertical direction for the Cu wire with ϕ 25 and 100 μm are presented in Figure 6.20 and 6.21 respectively. The apparent widths (FWHM) for the fluorescent signal of Cu K_{α} in both horizontal and vertical directions are expressed in Table 6.5 for the Cu wire with ϕ 100 μm and Table 6.21 for the Cu wire with ϕ 25 μm .

Table 6.5: Apparent widths (FWHM) for the fluorescent signal of Cu K_{α} (the Cu wire with ϕ 100 μm) in horizontal (see Figure 6.20(a)) and vertical (see Figure 6.20(b)) directions for white beam.

No.scanned turn	x FWHM (μm)	y FWHM (μm)
1	136.79	155.91
2	136.04	157.47
3	136.74	155.80
4	136.67	154.22
5	137.97	-
6	135.61	-
7	138.75	-
average	136.94	155.85

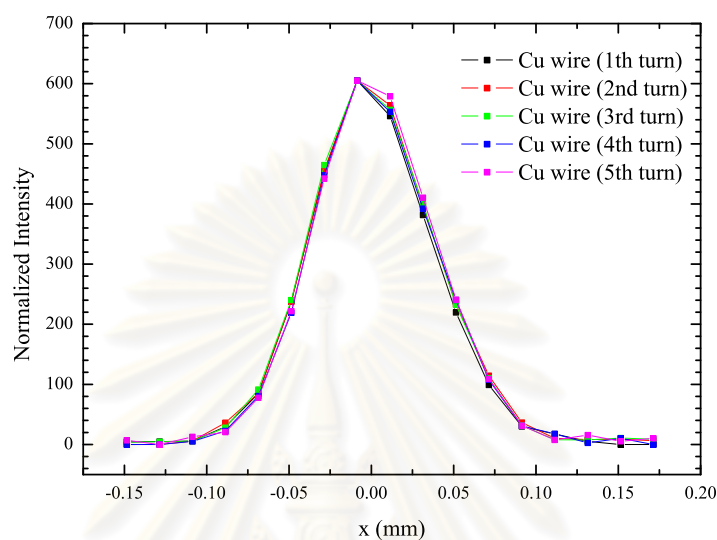


(a)

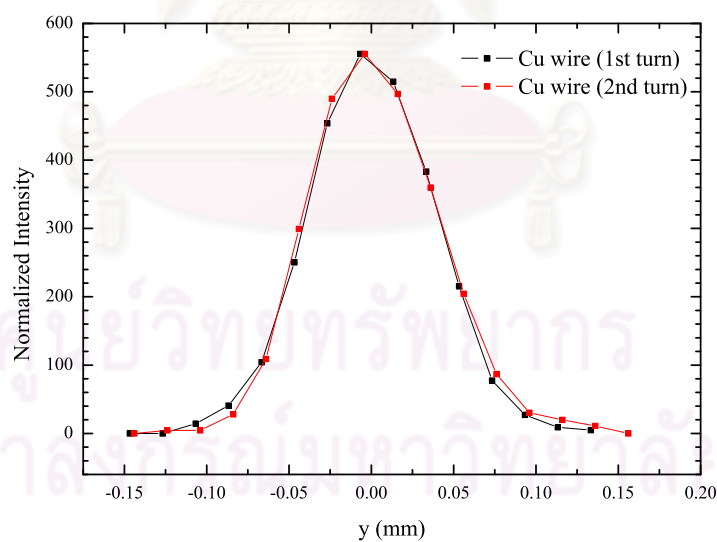


(b)

Figure 6.20: Fluorescent signal from Cu K_{α} for the Cu wire with ϕ $100 \mu\text{m}$ normalized by the electron beam current scanned in (a) the horizontal direction (x) and (b) the vertical direction (z) for white beam. The step size is $50 \mu\text{m}$ and the counting time is 30 s/step.



(a)



(b)

Figure 6.21: Fluorescent signal from Cu K_{α} for the Cu wire with ϕ 25 μm normalized by the electron beam current scanned in (a) the horizontal direction (x) and (b) the vertical direction (z) for white beam. The step size is 20 μm and the counting time is 30 s/step.

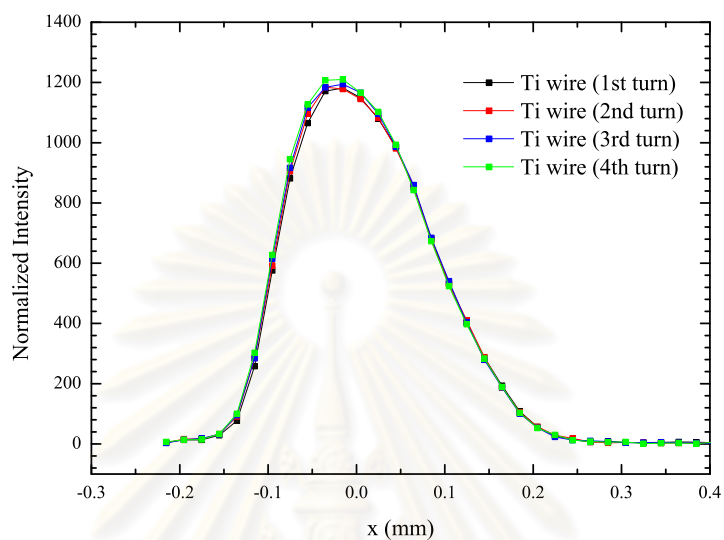
Table 6.6: Apparent widths (FWHM) for the fluorescent signal of Cu K_{α} (the Cu wire with ϕ 25 μm) in horizontal (see Figure 6.21(a)) and vertical (see Figure 6.21(b)) directions for white beam.

No.scanned turn	x FWHM (μm)	y FWHM (μm)
1	84.868	88.000
2	85.056	89.365
3	84.114	-
4	83.031	-
5	83.596	-
average	84.133	88.683

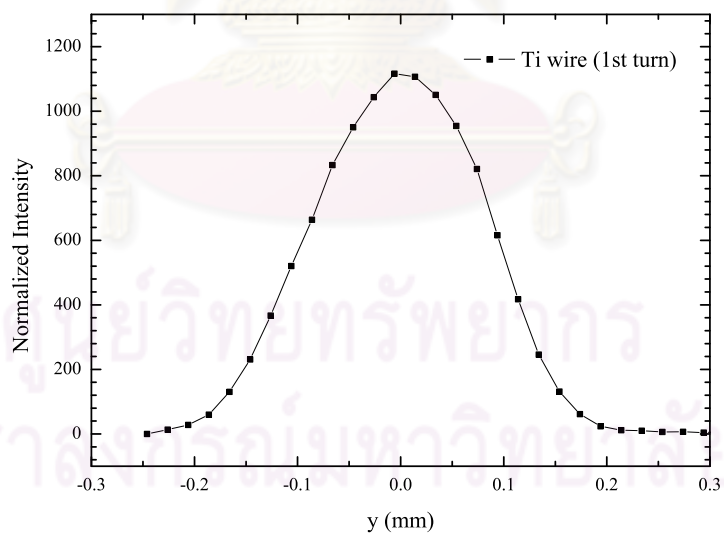
After that, due to the unavoidable development of the beamline, we have to move the apparatus to a new position (6 m away from current position at the beamline BL2); therefore, the beam size at new position is bigger than that of the old one because of the beam convergence. At this position, we used the Ti wire with ϕ 50 μm for measuring the focused white x-ray beam size. The fluorescent signal at Ti K_{α} in both horizontal and vertical direction are expressed in Figure 6.22. The apparent widths (FWHM) for the fluorescent signal of Ti K_{α} in both horizontal and vertical directions are expressed in Table 6.7. For this case, the focused beam size is $163 \times 170 \mu m^2$.

Table 6.7: Apparent widths (FWHM) for the fluorescent signal of Cu K_{α} (the Cu wire with ϕ 25 μm) in horizontal (see Figure 6.22(a)) and vertical (see Figure 6.22(b)) directions for white beam.

No.scanned turn	x FWHM (μm)	y FWHM (μm)
1	181.585	193.220
2	182.971	-
3	182.525	-
4	181.490	-
average	182.143	193.220



(a)



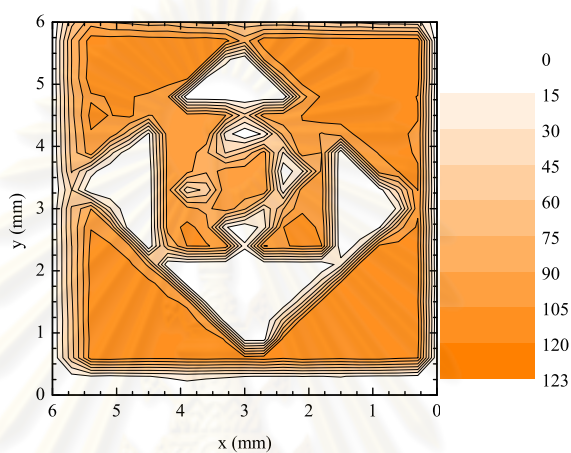
(b)

Figure 6.22: Fluorescent signal from Ti K_{α} normalized by the electron beam current scanned in (a) the horizontal direction (x) and (b) the vertical direction (z) for white beam. The step size is $20 \mu\text{m}$ and the counting time is 30 s/step.

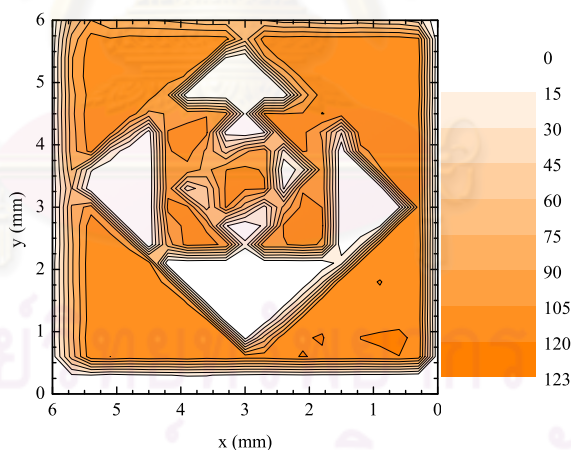
Scanning Position Calibration

Defining the scanned position using the grid pattern

Figure 6.23 presents the XRF images of copper for 1st and 2nd scans using grid pattern for calibrating the scanned position. As results, it indicates that the scanning is repeatable. For this calibration method, we also recorded the



(a)



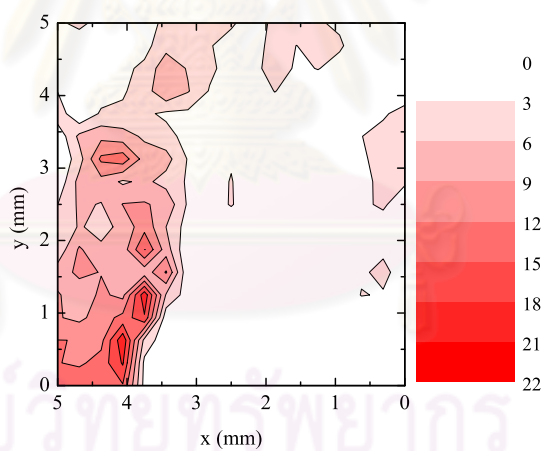
(b)

Figure 6.23: XRF images of copper for 1st and 2nd scans. The step size is $150 \mu\text{m}$, the counting time is 10 s/step and the scanned area is $6000 \times 6000 \mu\text{m}^2$.

XRF images from shark's fang fossil and a sticky rice grain with high amount of cadmium. Figure 6.24 specifies that at the edge of the fang fossil consist of iron. The XRF imaging of the sticky rice in Figure 6.25(b) indicates that the amount of cadmium is around the rice-germ.

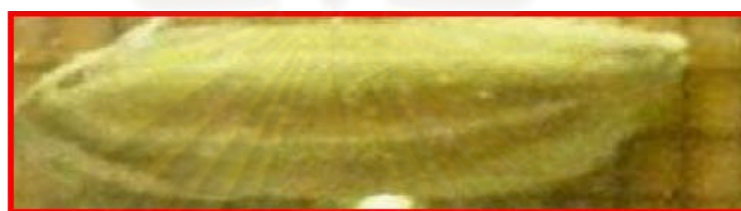


(a)

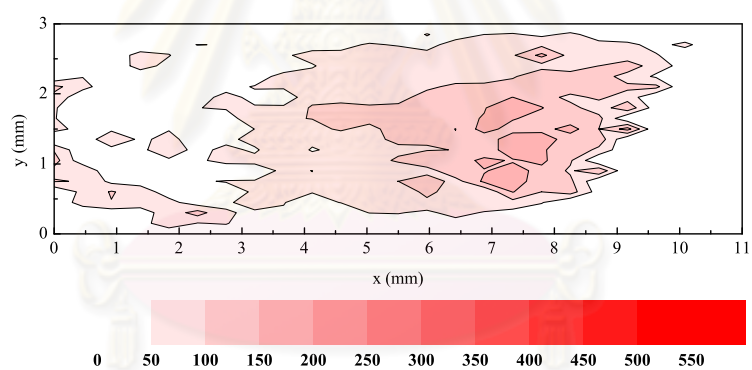


(b)

Figure 6.24: Imaging scans of a sharks fang fossil being preserved in rock. (a) Captured photo by the CCD camera (b) the information of Fe K_{α} in the sample. The step size is $150 \mu\text{m}$, the counting time is 10 s/step and the scanned area (red boundary) is $5000 \times 5000 \mu\text{m}^2$.



(a)

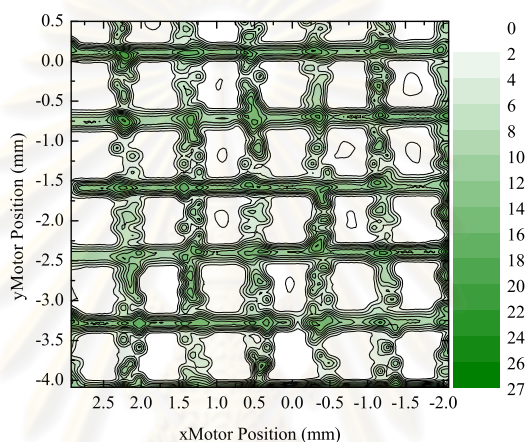


(b)

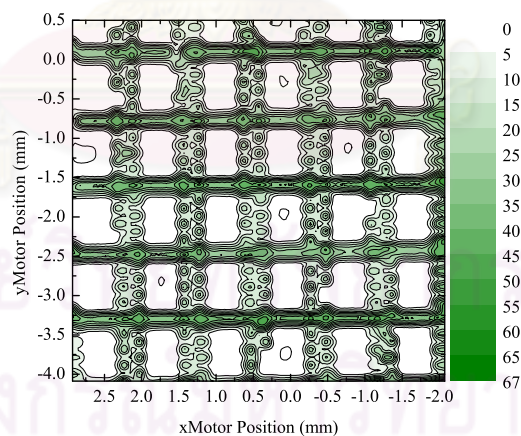
Figure 6.25: (a) Photo of the rice grain, (b) the information of Cd L_{α} for the sample. The step size is $150 \mu\text{m}$, the counting time is 10 s/step and the scanned area (red boundary) is $300 \times 11000 \mu\text{m}^2$.

Calibrating picture frame and motor frame using the nickel mesh

For picture frame and motor frame calibration using the nickel mesh, we scanned the mesh according to the described procedures in chapter 5. Figure 6.26 presents the XRF images of the nickel mesh. Δy for the XRF image in Figure 6.26(a) is 0.05 mm so we need to rotate the picture frame by 0.573 degree (clockwise) with respect to the pivot.



(a)



(b)

Figure 6.26: XRF images of the nickel mesh for 1st and 2nd scans. The step size is 100 μm , the counting time is 5 s/step and the scanned area is 5.04(x) \times 4.6(y) mm². The image (b) was rotated by 0.573 degree (clockwise).

Sample: Nickel grids on supporting glass

We used nickel grids of different sizes coated on supporting glass (see Figure 5.4) for testing the accuracy of the XRF imaging experiment firstly in one direction (horizontal).

For the setup No.1 (see Figure 5.3(a)), the relevant dimensions the spatial profiles of the fluorescent signal of the nickel grid structure denoted by the capital letters in Figure 5.4 and Figure 6.27 are given in Table 6.8. The width of the profile (D) and spacing distance (E) evidently correspond to the dimension B and C of the grid patterns, respectively. The results for the setup No.1 in Table 6.8 indicate that dimensions of the grid in the beam frame do not match with the real dimension of the grid. Therefore, the apparatus adapted to the setup No.2 as shown in Figure 6.28 for fixing this problem. As result, the setup No.2 can reduce the error of setup No.1 by 27%.

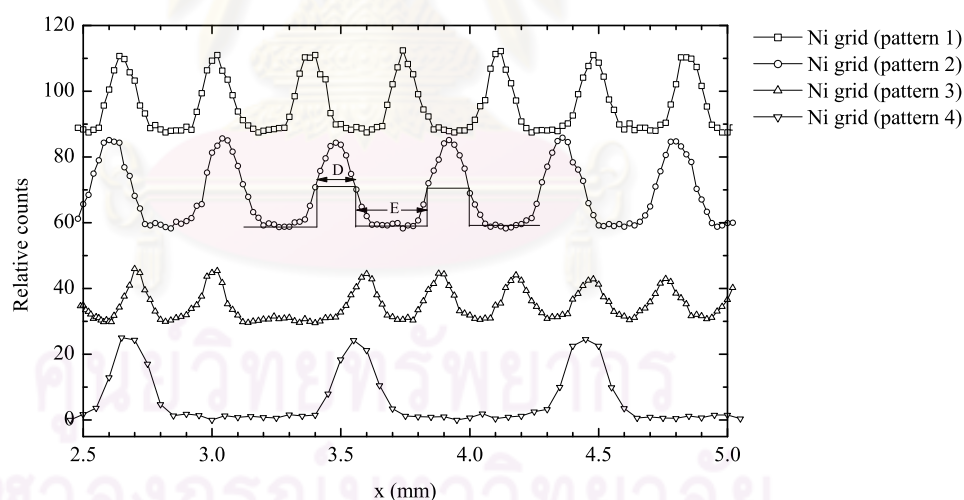


Figure 6.27: Spatial profiles of Ni K_{α} recorded from the grid patterns.

Table 6.8: Setup No.1: widths (A, B) and spacing (C) of the nickel grid structure denoted in Figure 5.4(b). Widths (D) and spacing (E) of the fluorescent patterns in Figure 6.27.

Nickel grid No. Pattern	Width (mm)				
	A	B	C	D	E
1	0.085	0.110	0.395	0.097	0.269
2	0.155	0.190	0.410	0.126	0.313
3	0.010	0.050	0.350	0.118	0.174
4	0.150	0.195	1.000	0.147	0.734

ศูนย์วิทยทรัพยากร
จุฬาลงกรณ์มหาวิทยาลัย

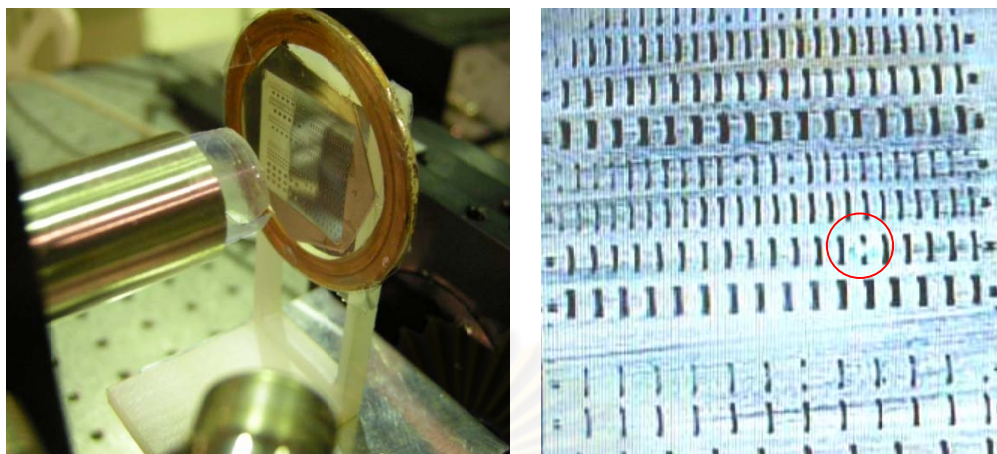


Figure 6.28: New apparatus (No.2) for one dimensional testing (left). Focused white beam (red circle) on the Ni grid pattern 1 (right).

Table 6.9: Setup No.2: widths (A, B) and spacing (C) of the nickel grid structure. Widths (D) and spacing (E) of the fluorescent patterns.

Nickel grid No. Pattern	Width (mm)				
	A	B	C	D	E
1	0.085	0.110	0.395	0.112	0.393
2	0.155	0.190	0.410	0.179	0.456
3	0.01	0.050	0.350	0.093	0.310
4	0.15	0.195	1.000	0.205	0.998

ศูนย์วิทยทรัพยากร
จุฬาลงกรณ์มหาวิทยาลัย

Sample: A hand-made pattern of cobalt foil overlaid on copper foil

For testing the two dimensional XRF imaging system, we used a hand-made pattern of cobalt foil ($7.5\ \mu\text{m}$ -thick) overlaid on copper foil ($4\ \mu\text{m}$ -thick) as shown in Figure 6.29. At this point, the apparatus for XRF imaging can distinguish the regions of copper and cobalt in the pattern. The fluorescent data of Cu K_α and Co K_α in 2D scans were reconstructed with color levels corresponding to the photon counts shown in Figures 6.29(b) and 6.29(c), respectively. The overall fluorescent images resemble the morphology of the test object. It can be seen that a careful calibration of the scanning position is very important for accurate mapping the fluorescent image with the visual image of the sample. This is one of the remaining tasks to be carried out to complete our XRF imaging technique.

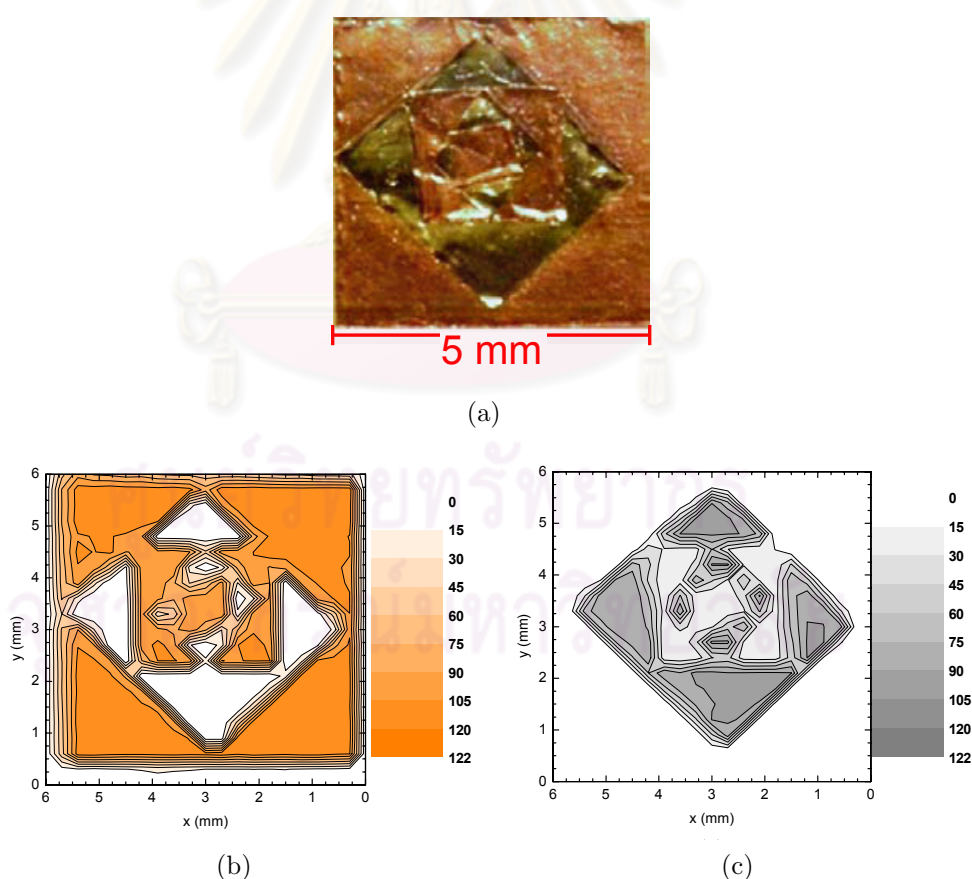
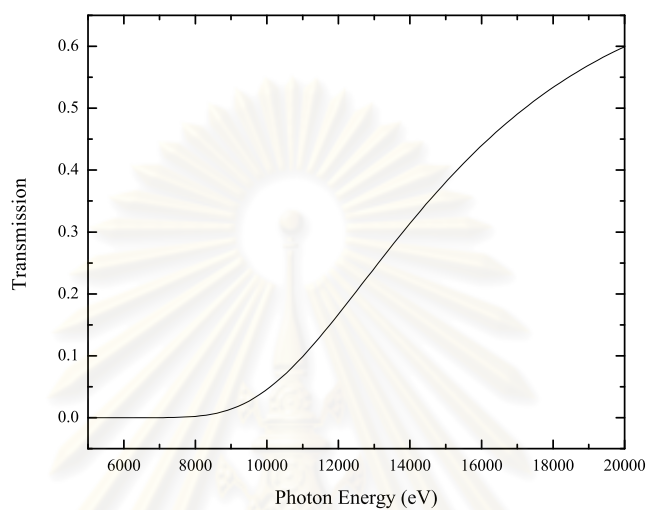


Figure 6.29: (a) Photograph of the test object made of copper (seen in orange) and cobalt (gray) foils. XRF Images (b) and (c) of copper and cobalt, respectively. The step size is $150\ \mu\text{m}$, the counting time is 10 s/step and the scanned area is $6000\ \mu\text{m} \times 6000\ \mu\text{m}$.

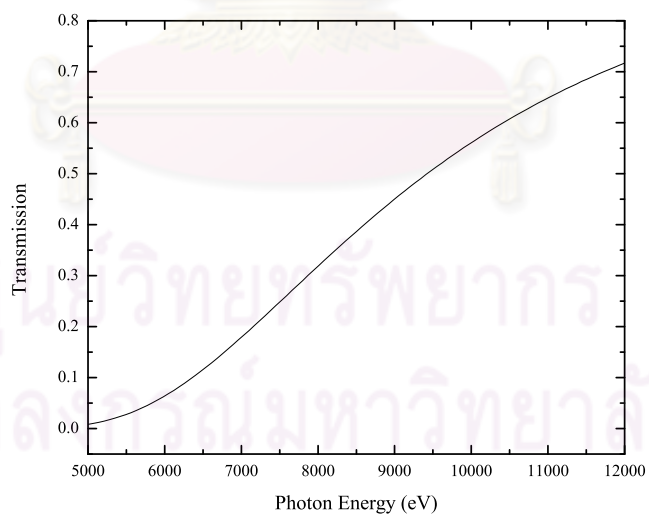
6.4 X-Ray Powder Diffraction

By using monochromatic x-ray beam with a photon energy of 8823.86 eV from bending magnet at the beamline BL2, the recorded diffraction patterns are presented in Figure 6.31 - 6.33. The setup for XRPD under high pressure consists of the capillary lens, the collimator, pinhole with ϕ 200 μm and powder of CeO_2 loaded in the DAC (see Figure 5.12). The recorded diffraction patterns under high pressure condition are shown in Figure 6.31. We cannot record any diffraction ring. According to the x-ray transmission for diamond culets in the DAC and air (see Figure 6.30), a lot of x-ray photon with a photon energy of 8823.86 eV are absorbed by diamond culets in the DAC and also by air. Hence, we tried to reduce the x-ray absorption by removing the pin hole in order to increase incident photon flux; although, we cannot recorded any diffraction ring recorded as expressed in Figure 6.31(c). At this point, it indicates that our experiment requires higher energy for incident x-ray.

Since we cannot record the diffraction pattern under high pressure using focusing lens, the diffraction patterns at ambient condition using the lens were recorded instead. The recorded diffraction patterns for Al_2O_3 and CeO_2 at ambient condition are shown in Figure 6.32 - 6.33. We used the pinhole for recording the pattern from Al_2O_3 in Figure 6.32(a); as result, intensity of the pattern is too weak. Hence, we fixed this problem by recorded the remained patterns without the pinhole, the recorded diffraction patterns seem to be clearly as shown in Figure 6.32(b) and 6.33.



(a)



(b)

Figure 6.30: X-ray transmission for (a) the diamond culets with thickness of $4000 \mu\text{m}$ and (b) air with path length 100 cm.

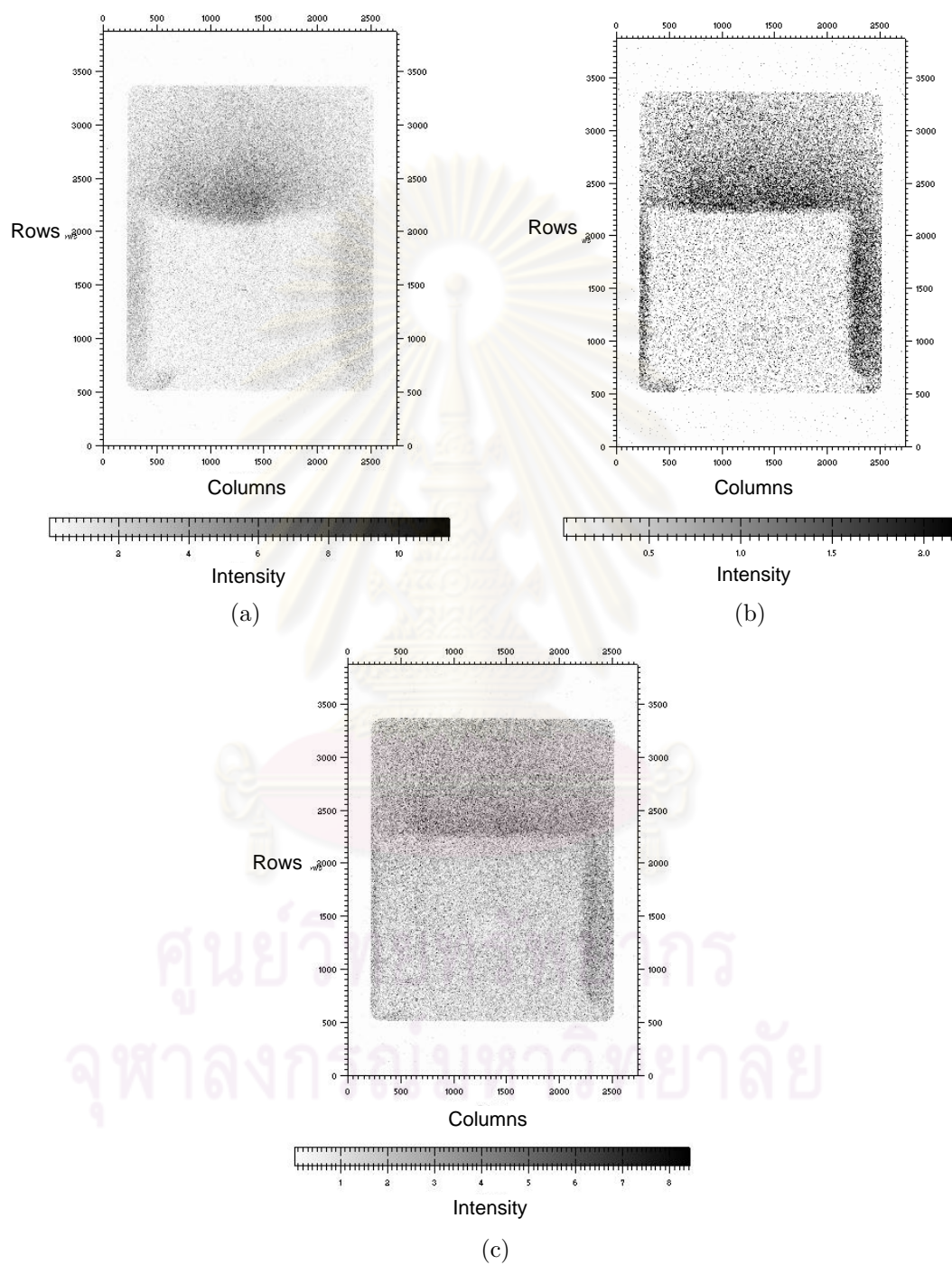


Figure 6.31: X-ray powder diffraction pattern for CeO_2 under high pressure. Recorded time are (a) 3 (b and c) 4 hrs.

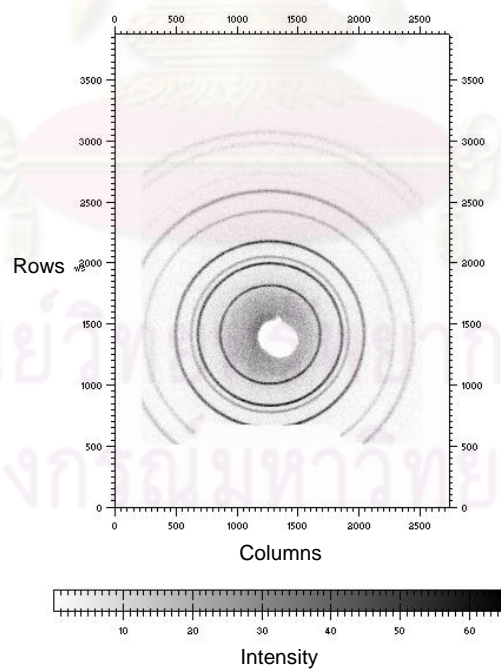
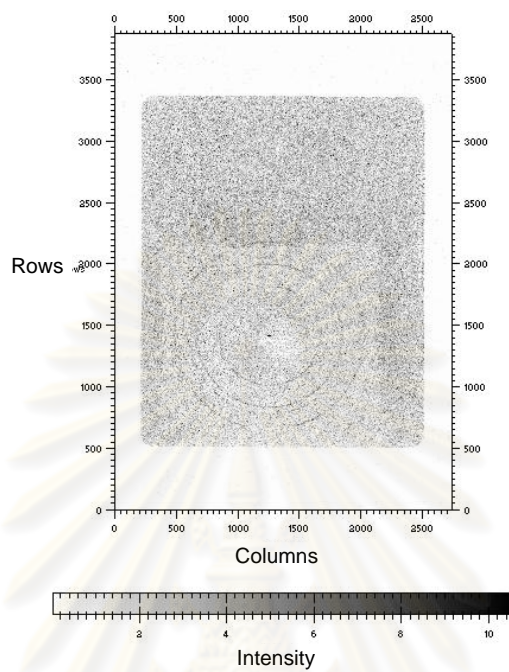


Figure 6.32: X-ray powder diffraction pattern for Al_2O_3 at ambient condition. Recorded time are (a) 4 and (b) 2.5 hrs.

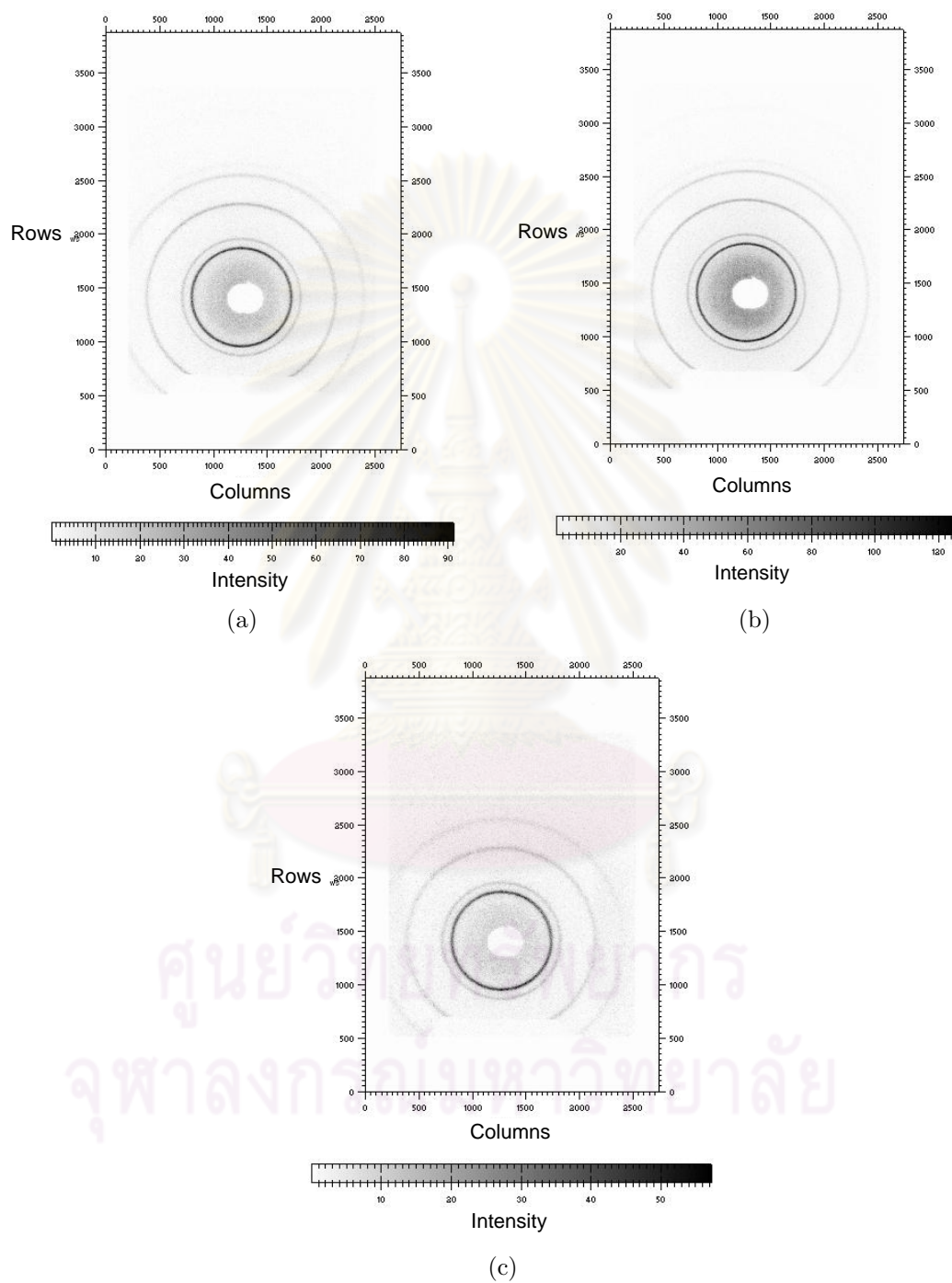


Figure 6.33: X-ray powder diffraction pattern for CeO_2 at ambient condition. Recorded time is (a) 2.5, (b) 3 and (c) 4 hrs.

CHAPTER VII

CONCLUSIONS

7.1 Ray Tracing Simulation

Synchrotron Beamline Optics for X-ray Powder Diffraction under High Pressure Condition at the Siam Photon Laboratory

At this point, we can conclude that the W/B_4C multilayer is appropriate for the DMM in order to increase the photon flux for the bending magnet beamline at the Siam Photon Laboratory. The optimal mirror magnification of the toroidal focusing mirror for the limited length of the beamline is M0.7. The expected flux at sample through a $0.3 \times 0.3 \text{ mm}^2$ aperture is 2.7×10^{10} photons/sec/100mA, which is about 7500 times higher than that of the beamline BL8. In addition, less aberration and small x-ray beam size is required for the XRPD technique. Therefore, the mirror magnification M0.7 is a good choice for upgrading the existing beamline or developing a new one.

Focused monochromatic beam for x-ray absorption spectroscopy and x-ray fluorescent techniques

The results of ray tracing simulations indicate that case C can provide the best photon flux; however, the flux will be reduced after inserting a circular pinhole. According to beam width and beam convergence for all cases of beamline designs, the flux for cases D2 and D3 do not substantially reduced too much after inserting a circular pinhole.

7.2 X-Ray Fluorescent Technique

According to the results, our XRF experimental setup using a white x-ray beam from the synchrotron bending magnet is capable of identifying major and trace elements present in the samples. XRF imaging system shows sufficient potential performance to become one of the major techniques available at the Siam Photon

Laboratory. Position calibration will be conducted to improve the precision of the XRF image mapping. We have shown that XRF experiments using white-beam x-rays have better sensitivity than conventional monochromatic x-rays.

7.3 X-Ray Powder Diffraction Technique

The results indicate that powder diffraction under ambient condition can be performed using the developed apparatus. However, the hard x-ray from wavelength shifter is required in order to perform high pressure experiment with diamond anvil cell.

The text indicate that this thesis covers the important details for developing the synchrotron radiation beamline including the beamline design and the techniques — XRF imaging and analysis and also XRPD under high-pressure conditions — for supporting and expanding the knowledge of science in Thailand.



ศูนย์วิทยทรัพยากร
จุฬาลงกรณ์มหาวิทยาลัย

References

- [1] G. R. Burbidge. On Synchrotron Radiation from Messier 87. *Burbidge, G. R.* 124 (1956): 416.
- [2] F. R. Elder, A. M. Gurewitsch, R. V. Langmuir, and H. C. Pollock. Radiation from electrons in a synchrotron. *Phys. Rev.* 71 (1947): 829–830.
- [3] P. J. Duke. *Synchrotron Radiation Production and Properties*. Oxford University Press. illustrated edition. 2000.
- [4] Kwang J. Kim. Optical and power characteristics of synchrotron radiation sources. *Optical Engineering* 34 (1995): 342–352.
- [5] David Attwood. *Soft X-Rays and Extreme Ultraviolet Radiation: Principles and Applications*. Cambridge University Press. illustrated edition. 2007.
- [6] NSRC. *National Synchrotron Research Center Annual Report*. Gnomes House Co., Ltd. 2006.
- [7] Akihisa Takeuchi, Yasuko Terada, Yoshio Suzuki, Kentaro Uesugi, and Sadao Aoki. Confocal full-field X-ray microscope for novel three-dimensional X-ray imaging. *Journal of Synchrotron Radiation* 16 (2009): 616–621.
- [8] Tianxi Sun, Meiling Zhang, Zhiguo Liu, Zhiguang Zhang, Gang Li, Yongzhong Ma, Xiaoguang Du, Quanjie Jia, Yu Chen, Qingxi Yuan, Wanxia Huang, Peiping Zhu, and Xunliang Ding. Focusing synchrotron radiation using a polycapillary half-focusing X-ray lens for imaging. *Journal of Synchrotron Radiation* 16 (2009): 116–118.
- [9] BRIAN P. FLANNERY, HARRY W. DECKMAN, WAYNE G. ROBERGE, and KEVIN L. D'AMICO. Three-Dimensional X-ray Microtomography. *Science* 237 (1987): 1439–1444.
- [10] O. F. Vyvenko, T. Buonassisi, A. A. Istratov, E. R. Weber, M. Kittler, and W. Seifert. Application of synchrotron-radiation-based x-ray microprobe techniques for the analysis of recombination activity of metals precipitated at si/sige misfit dislocations. *Journal of Physics: Condensed Matter* 14 (2002): 13079.
- [11] R. Kautenburger. Multi element analysis by x-ray fluorescence: A powerful tool of ivory identification from various origins. *Journal of Radioanalytical and Nuclear Chemistry* 260 (May 2004): 399–404(6).

- [12] O. Gonzalez-Fernandez, I. Queralt, M.L. Carvalho, and G. Garcia. Elemental analysis of mining wastes by energy dispersive x-ray fluorescence (edxf). *Nuclear Instruments and Methods in Physics Research Section B: Beam Interactions with Materials and Atoms* 262 (2007): 81 – 86.
- [13] Thiti Bovornratanaraks. PhD thesis. The University of Edinburgh. 2001.
- [14] C. Welnak, G.J. Chen, and F. Cerrina. Shadow: A synchrotron radiation and x-ray optics simulation tool. *Nuclear Instruments and Methods in Physics Research Section A: Accelerators, Spectrometers, Detectors and Associated Equipment* 347 (1994): 344 – 347.
- [15] Wantana Klysubun, Panidta Sombunchoo, Narupon Wongprachanukul, P. Tarawarakarn, S. Klinkhieo, Jitrin Chaiprapa, and Prayoon Songsiriritthigul. Commissioning and performance of X-ray absorption spectroscopy beamline at the Siam Photon Laboratory. *Nuclear Instruments and Methods in Physics Research Section A: Accelerators, Spectrometers, Detectors and Associated Equipment* 582 (2007): 87–89.
- [16] H. Riesemeier, K. Ecker, W. Görner, B. Müller, R., M. Radtke, and M. Krumrey. Layout and first XRF applications of the BAMline at BESSY II. *X-Ray Spectrometry* 34 (2005): 160–163.
- [17] Y. Shvyd'ko. *X-Ray Optics: High-Energy-Resolution Applications (Springer Series in Optical Sciences)*. Berlin, Heidelberg: Springer-Verlag. 2004.
- [18] Alexander Kazimirov, Detlef-M. Smilgies, Qun Shen, Xianghui Xiao, Quan Hao, Ernest Fontes, Donald H. Bilderback, Sol M. Gruner, Yuriy Platonov, and Vladimir V. Martynov. Multilayer X-ray optics at CHESS. *Journal of Synchrotron Radiation* 13 (2006): 204–210.
- [19] Christian Morawe, Jean-Christophe Peffen, Eric Ziegler, and Andreas K. Freund. High-resolution multilayer x-ray optics. *Advances in X-Ray Optics* 4145 (2001): 61–71.
- [20] N. N. Salashchenko, Yu. Ya. Platonov, and S. Yu. Zuev. Multilayer x-ray optics for synchrotron radiation. *Nuclear Instruments and Methods in Physics Research Section A: Accelerators, Spectrometers, Detectors and Associated Equipment* 359 (1995): 114 – 120.
- [21] Martin Kunz, Alastair A. MacDowell, Wendel A. Caldwell, Daniella Cambie, Richard S. Celestre, Edward E. Domning, Robert M. Duarte, Arianna E. Gleason, James M. Glossinger, Nicholas Kelez, David W. Plate, Tony Yu, Joeseoph M. Zaug, Howard A. Padmore, Raymond Jeanloz, A. Paul Alivisatos, and Simon M. Clark. A beamline for high-pressure studies at the Advanced

- Light Source with a superconducting bending magnet as the source. *Journal of Synchrotron Radiation* 12 (2005): 650–658.
- [22] G. Falkenberg, O. Clauss, A. Swiderski, and Th. Tschentscher. Upgrade of the x-ray fluorescence beamline at hasylab/desy. *X-Ray Spectrometry* 30 (2001): 170–173.
- [23] C. A. MacDonald, S. M. Owens, and W. M. Gibson. Polycapillary X-ray optics for microdiffraction. *Journal of Applied Crystallography* 32 (1999): 160–167.
- [24] M. A. Kumakhov. Channeling of photons and new x-ray optics. *Nuclear Instruments and Methods in Physics Research Section B: Beam Interactions with Materials and Atoms* 48 (1990): 283 – 286.
- [25] Ari Ide-Ektessabi, Yukihide Ota, Ryoko Ishihara, Yutaka Mizuno, and Tohru Takeuchi. Distribution of lead in the brain tissues from dntc patients using synchrotron radiation microbeams. *Nuclear Instruments and Methods in Physics Research Section B: Beam Interactions with Materials and Atoms* 241 (2005): 681 – 684.
- [26] Kouichi Tsuji, Jasna Injuk, and Rene' Van Grieken. *X-Ray Spectrometry: Recent Technological Advances*. John Wiley & Sons, Ltd. 2004.
- [27] Akihisa Takeuchi, Sadao Aoki, Kimitake Yamamoto, Hidekazu Takano, Norio Watanabe, and Masami Ando. Full-field x-ray fluorescence imaging microscope with a Wolter mirror. *Review of Scientific Instruments* 71 (2000): 1279–1285.
- [28] J. R. Helliwell. *Rep. Prog. Phys.* 47 (1984): 1403.
- [29] V. Saengsuwan, W. Klysubun, T. Bovornratanaraks, and S. Rugmai. Synchrotron beamline optics for X-ray powder diffraction under high-pressure conditions at the Siam Photon Laboratory. *Zeitschrift für Kristallographie Supplements* 30 (2009): 189–194.
- [30] Ari Ide-Ektessabi. *Applications of Synchrotron Radiation: Micro Beams in Cell Micro Biology and Medicine*. Biological and Medical Physics, Biomedical Engineering. Springer Berlin Heidelberg. 2007.
- [31] Günter Gauglitz and Tuan Vo-Dinh. *Handbook of Spectroscopy*. Wiley-VCH, Weinheim. 1 edition. 2003.
- [32] E. P. Bertin. *Principles and Practice of X-Ray Spectrometric Analysis*. Plenum Press, New York. 1975.

- [33] J. A. Bearden. X-Ray Wavelengths. *Reviews of Modern Physics* 39 (1967): 78–124.
- [34] Onder Simsek, Oguz Dogan, Umit Turgut, and Mehmet Ertugrul. Measurement of k shell fluorescence yields of some elements in the atomic range $22 \leq z \leq 30$ using photoionisation. *Radiation Physics and Chemistry* 58 (2000): 207 – 211.
- [35] Sabriye Seven. A method for the determination of K shell fluorescence yields using photoionization. *Journal of Quantitative Spectroscopy and Radiative Transfer* 74 (2004): 69–74.
- [36] Mehmet Ertugrul. Determination of L_3 subshell fluorescence yield of Nd with a Si(Li) detector. *Nuclear Instruments and Methods in Physics Research Section B: Beam Interactions with Materials and Atoms* 124 (1997): 475–477.
- [37] O. Simsek, M. Ertugrul, D. Karagoz, G. Budak, A. Karabulut, S. Yilmaz, O. Dogan, U. Turgut, O. Sogut, R. Polat, and A. Gurol. K shell fluorescence yields for elements with $33 \leq Z \leq 53$ using 59.5 keV photons. *Radiation Physics and Chemistry* 65 (2002): 27–31.
- [38] I. Han, M. Sahin, L. Demir, and Y. Sahin. Measurement of K X-ray fluorescence cross-sections, fluorescence yields and intensity ratios for some elements in the atomic range $22 \leq Z \leq 68$. *Applied Radiation and Isotopes* 65 (2007): 669–675.
- [39] Ozdemir Yuksel, Durak Ridvan, and Oz Elif. K-shell X-ray production cross-sections and fluorescence yields in some medium-Z elements. *Radiation Physics and Chemistry* 65 (2002): 199–204.
- [40] Xue-Liang Ren, Qing-Long Liu, Hao-Wei Fu, Dian xing Wu, and Qing-Yao Shu. Density alteration of nutrient elements in rice grains of a low phytate mutant. *Food Chemistry* 102 (2007): 1400 – 1406.
- [41] D.K. Teherani. Trace elements analysis in rice. *Journal of Radioanalytical and Nuclear Chemistry* 107 (1987): 133–143.
- [42] M.Z. Mollah, N.M. Talukder, M.N. Islam, M.A. Rahman, and Z. Ferdous. Effect of nutrients content in rice as influenced by zinc fertilization. *World Applied Sciences Journal* 6 (2009): 1082–1088.
- [43] Varalak Saengsuwan, Wantana Klysubun, Saroj Rujirawat, and Thiti Bovornratanarak, editors. *A feasibility study of x-ray fluorescent analysis by utilizing synchrotron radiation*. Walailak University, Nakhon Si Thammarat, Thailand. Proceeding of the 33rd congress on science and technology of Thailand (STT 33). 2007.

- [44] M. Al-Turany, J. D. Meyer, and K. Bethge. PIXE analysis with the XR-100CR Si-PIN detector. *Nuclear Instruments and Methods in Physics Research Section B: Beam Interactions with Materials and Atoms* 155 (1999): 137–142.
- [45] I. Ahmad, R. R. Betts, T. Happ, D. J. Henderson, F. L. H. Wolfs, and A. H. Wuosmaa. Nuclear spectroscopy with Si PIN diode detectors at room temperature. *Nuclear Instruments and Methods in Physics Research Section A: Accelerators, Spectrometers, Detectors and Associated Equipment* 299 (1990): 201–204.
- [46] P. Leutenegger, A. Longoni, C. Fiorini, L. Strder, J. Kemmer, P. Lechner, S. Sciuti, and R. Cesareo. Works of art investigation with silicon drift detectors. *Nuclear Instruments and Methods in Physics Research Section A: Accelerators, Spectrometers, Detectors and Associated Equipment* 439 (2000): 458–470.
- [47] Arunee Promsawad, Arunee Kongsakphaisal, and Sirinart Laoharojanaphand. Determination of cadmium in rice by radiochemical neutron activation analysis. *KMITL Science Journal (Section B)* 8 (2008): 12–17.
- [48] R. Govil and S. K. Kataria. A semi-empirical method for quantitative XRF analysis of thick samples. *X-Ray Spectrometry* 11 (1982): 144–148.
- [49] J. L. Galvez, J. Dufour, C. Negro, and F. Lopez-Mateos. Routine to estimate composition of concentrated metal-nitric-hydrofluoric acid pickle liquors. *Hydrometallurgy* 96 (2009): 88 – 94.
- [50] Miloslav Pouzar, Tomas Cernohorsk, and Anna Krejcova. Determination of metals in lubricating oils by x-ray fluorescence spectrometry. *Talanta* 54 (2001): 829 – 835.
- [51] Marit Andersson and Ake Olin. A modified standard addition method in x-ray fluorescence spectrometry. *Talanta* 40 (1993): 669 – 674.
- [52] S. B. Torok, J. Labar, J. Injuk, and R. E. V. Grieken. X-ray spectrometry. *Analytical Chemistry* 68 (1996): 467R–485R.
- [53] S. B. Torok, J. Labar, M. Schmeling, and R. E. V. Grieken. X-ray spectrometry. *Analytical Chemistry* 70 (1998): 495R–517R.
- [54] A. E. S. Vives, S. Moreira, S. M. B. Brienza, O. L. A. Zucchi, and V. F. N. Filho. Synchrotron radiation total reflection X-ray fluorescence (SR-TXRF) for evaluation of food contamination. *Journal of Radioanalytical and Nuclear Chemistry* 270 (2006): 147–153.

- [55] A. Erko, M. Idir, T. Krist, and A. G. Michette. *Modern Developments in X-Ray and Neutron Optics*. volume 137/2008 of *Springer Series in Optical Sciences*. Springer-Verlag Berlin Heidelberg. 2008.
- [56] D. V. Rao, M. Swapna, R. Cesareo, A. Brunetti, T. Akatsuka, T. Yuasa, T. Takeda, G. Tromba, and G.E. Gigante. Investigation of the distribution of elements in snail shell with the use of synchrotron-based, micro-beam X-ray fluorescence spectrometry. *Journal of Trace Elements in Medicine and Biology* 23 (2009): 251–257.
- [57] G. R. Pereira, H. S. Rocha, M. J. Anjos, P. C. M. A. Farias, C. A. Perez, and R. T. Lopes. Elemental distribution mapping on breast tissue samples. *European Journal of Radiology* 68S (2008): S104–S108.
- [58] Munekawa Shigeru and Joseph D. Ferrara. *Imaging Plates as Detectors for X-ray Diffraction*. [online]. Available from: <http://www.rigakumsc.com>. [15/02/2004].
- [59] Varalak Saengsuwan. *Crystal Structure of CuInSe₂*. Master's thesis. Department of Physics, Faculty of Science, Chulalongkorn University. 2004.
- [60] A. Boultif and D. Louër. Indexing of powder diffraction patterns for low-symmetry lattices by the successive dichotomy method. *Journal of Applied Crystallography* 24 (1991): 987–993.
- [61] T. J. B. Holland and S. A. T. Redfern. *UNITCELL*: a nonlinear least-squares program for cell-parameter refinement and implementing regression and deletion diagnostics. *Journal of Applied Crystallography* 30 (1997): 84.
- [62] K. Leinenweber. *Crystal-Cracker (build 186) X-ray program*. [online]. Available from: <http://multianvil.asu.edu>. [24/06/2004].
- [63] H. M. Rietveld. A profile refinement method for nuclear and magnetic structures. *Journal of Applied Crystallography* 2 (1969): 65–71.
- [64] R. A. Young. *The Rietveld Method*. Oxford University Press. 1993.
- [65] M. Ahtee, M. Nurmela, P. Suortti, and M. Järvinen. Correction for preferred orientation in Rietveld refinement. *Journal of Applied Crystallography* 22 (1989): 261–268.
- [66] A. C. Larson and R. B. Von Dreele. General Structure Analysis System (GSAS). *Los Alamos National Laboratory Report LAUR* (2000): 86–748.
- [67] Brian H. Toby. *EXPGUI*, a graphical user interface for *GSAS*. *Journal of Applied Crystallography* 34 (2001): 210–213.

- [68] National Institute of Standards and Technology, Gaithersburg, MD 20899. *Certificate of Analysis, SRM 610 Trace Elements in a Glass Matrix*. [online]. Available from: <https://www-s.nist.gov/srmors/certificates/610.pdf>. [11/03/2009].
- [69] O. Shimomura, K. Takemura, H. Fujihisa, Y. Fujii, Y. Ohishi, T. Kikegawa, Y. Amemiya, and T. Matsushita. Application of an imaging plate to high-pressure x-ray study with a diamond anvil cell (invited). *Proceedings of the 4th International Conference on Synchrotron Radiation Instrumentation* 63 (1992): 967–973.
- [70] Gasper J. Piermarini. High Pressure X-Ray Crystallography With the Diamond Cell at NIST/NBS. *Journal of Research of the National Institute of Standards and Technology* 106 (2001): 889–920.
- [71] R. B. Lazarenko and L. N. Lazarenko. *American Machinist* 91 (1947): 120.
- [72] H. E. Lorenzana, M. Bennahmias, H. Radousky, and M. B. Kruger. Producing diamond anvil cell gaskets for ultrahigh-pressure applications using an inexpensive electric discharge machine. *Review of Scientific Instruments* 65 (1994): 3540–3543.
- [73] Stefan Braun, Peter Gawlitza, Maik Menzel, Andreas Leson, Marcel Mertin, and Franz Schäfers. Reflectance and Resolution of Multilayer Monochromators for Photon Energies from 400 – 6000 eV. *AIP Conference Proceedings* 879 (2007): 493–496.

Biography

Varalak Saengsuwan was born in Bangkok, Thailand in 1981. In 2001, she graduated from Mahidol University with the degree of B.Sc.(physics). Afterwards, she worked in the Extreme Condition Physics Research Laboratory and was awarded a M.Sc. degree in physics from Chulalongkorn University in 2004. She continued her Ph.D. research about XRF and XRD under high-pressure at the Siam Photon Laboratory and was awarded a Ph.D. degree in physics from Chulalongkorn University in 2009.

International Journals:

1. V. Saengsuwan, W. Klysubun, T. Bovornratanaraks and S. Rugmai, "Synchrotron Beamline Optics for X-ray Powder Diffraction under High-Pressure Conditions at the Siam Photon Laboratory." *Zeitschrift für Kristallographie Supplement*, **30** (2009) 189-194.
2. V. Saengsuwan, W. Klysubun, T. Bovornratanaraks, N. Wongprachanukul and T. Srisatit, "Progress on the Development of XRF Imaging and Analysis at the Siam Photon Laboratory." *AIP Conference Proceedings (accepted)*, (2010).

International Conferences:

1. V. Saengsuwan, W. Klysubun, T. Bovornratanaraks, N. Wongprachanukul and T. Srisatit. "Progress on the Development of XRF Imaging and Analysis at the Siam Photon Laboratory." *The 10th International Conference on Synchrotron Radiation Instrumentation*. Melbourne, Australia (27 Sep - 2 Oct 2009)
2. V. Saengsuwan, W. Klysubun and T. Bovornratanaraks. "Synchrotron Beamline Optics for X-Ray Powder Diffraction under High Pressure Condition at the Siam Photon Laboratory." *The 11th European Powder Diffraction Conference*. Warsaw University of Technology, Poland (18-22 Sep 2008)